Wiley Interdisciplinary Reviews: Computational Molecular Science

WILEY

WIREs COMPUTATIONAL MOLECULAR SCIENCE

ADVANCED REVIEW OPEN ACCESS

Computation of Time-Resolved Nonlinear Electronic Spectra From Classical Trajectories

Maxim F. Gelin[1] | Zhenggang Lan[2] | Nađa Došlić[3] | Wolfgang Domcke[4]

[1]School of Science, Hangzhou Dianzi University, Hangzhou, China | [2]Key Laboratory of Theoretical Chemistry of Environment, Ministry of Education and Guangdong Provincial Key Laboratory of Chemical Pollution and Environmental Safety; School of Environment, South China Normal University, Guangzhou, China | [3]Department of Physical Chemistry, Ruder Bošković Institute, Zagreb, Croatia | [4]Department of Chemistry, Technical University of Munich, Garching, Germany

Correspondence: Wolfgang Domcke (domcke@ch.tum.de)

Received: 3 October 2024 | **Revised:** 24 January 2025 | **Accepted:** 9 February 2025

Associate Editor: Sandra Luber | **Editor-in-Chief:** Peter R. Schreiner

Funding: M.F.G. acknowledges support from the National Natural Science Foundation of China (No. 22373028). Z.L. acknowledges support from the National Natural Science Foundation of China (No. 22333003, 22361132528, 21933011). N.D. acknowledges support from the Croatian Science Foundation (HRZZ grant no. HRZZ-IP-2022-10-4658).

ABSTRACT

A variety of time-resolved spectroscopic techniques employing femtosecond pump and probe pulses are nowadays widely used to unravel the fundamental mechanisms of photophysical and photochemical processes in molecules and materials. Theoretical support based on first-principles electronic-structure calculations is essential for the interpretation of the observed time and frequency resolved signals. Accurate calculations of nonlinear spectroscopic signals based on a quantum wave-packet description of the nonadiabatic excited-state dynamics have been demonstrated for diatomic and triatomic molecules. For polyatomic molecules with many nuclear degrees of freedom, quasi-classical trajectory descriptions of the excited-state dynamics are more practical. While the computation of time-dependent electronic population probabilities with quasi-classical trajectory methods has become routine, the simulation of time and frequency resolved pump-probe signals is more challenging. This article presents a theoretical framework for first-principles simulations of various femtosecond signals that is based on the third-order polarization and the quasi-classical implementation of the doorway-window approximation. The latter approximation is applicable for non-overlapping pump and probe pulses that are reasonably short on the characteristic time scale of the system dynamics. Apart from a systematic derivation of the theory, explicit computational protocols for the calculation of pump-probe signals are provided. Transient absorption pump-probe spectroscopy with UV pump and UV or X-ray probe pulses, two-dimensional electronic spectroscopy, and femtosecond time-resolved photoelectron spectroscopy are considered as specific examples. Recent applications of these computational methods to prototypical chromophores are briefly reviewed.

1 | Introduction

1.1 | Time-Resolved Nonlinear Spectroscopy

The exploration of the elementary steps of photochemical reactions with femtosecond time resolution has become a booming research field in recent decades thanks to the continuous improvement of pulsed radiation sources in the visible, ultraviolet (UV), vacuum ultraviolet (VUV) and soft X-ray spectral ranges [1–7]. The simplest concept of monitoring the time-resolved nonequilibrium dynamics of photoexcited molecular systems is transient absorption (TA) pump-probe (PP) spectroscopy [8]. In electronic TA PP spectroscopy, a pump pulse impulsively initiates the dynamics in one or several excited electronic states, and the dynamics are monitored by the transmission of a short probe pulse as a function of the time delay of the pulses [9]. In recent years, interest has shifted towards more sophisticated spectroscopies employing multiple phase-locked laser pulses for excitation. Partial Fourier transformations spread the spectroscopic information on two or three frequency axes, providing detailed time and frequency resolved imaging of the dynamics [10–13]. Probing with femtosecond X-ray pulses adds element specificity and thus atomic resolution to time-resolved spectroscopy [14].

In addition to time-resolved spectroscopies based on optical (photon) detection, time-resolved photoelectron spectroscopy (TRPES) has been developed as a versatile technique over the past three decades [15–22]. In TRPES, a short visible or UV pump pulse excites the molecular system, and the excited-state dynamics are probed via ionization of the excited states with a time-delayed UV, VUV, EUV, or X-ray pulse. Due to the high detection efficiency of electrons, TRPES is particularly versatile for molecules in the gas phase or clusters in supersonic jets.

On the theoretical side, the conventional framework for the description of nonlinear optical signals is based on perturbation theory in the radiation-matter interaction [8]. In the lowest-order description of a given nonlinear signal, one radiation-matter interaction per pulse is taken into account. In this scheme, two-pulse or three-pulse four-wave mixing (FWM) signals are determined by the third-order polarization [8, 23]. As is well established, the third-order polarization can be expressed in terms of third-order dipole response functions, which contain matrix elements of transition operators and field-free quantum propagators [8]. Alternatively, nonperturbative (in the radiation-matter interaction) descriptions of time-resolved nonlinear signals have been developed [24–29]. In this approach, the interactions with the laser pulses are included in the quantum mechanical equations of motion; that is, the time-dependent Schrödinger equation for isolated molecules or quantum master equations for chromophores in condensed-phase environments [30]. To extract the experimental signals detected with phase matching [23], phase cycling [31], or phase modulation [32], an appropriate a posteriori decomposition of the nonperturbatively computed nonlinear polarization is necessary [30]. For TRPES, perturbative and nonperturbative theories were developed and applied in parallel [33–37].

It is nowadays well established that the existence of conical intersections of potential-energy (PE) surfaces is the rule rather than the exception in photochemical dynamics [38–45]. The adiabatic PE surfaces near conical intersections exhibit exceptionally strong local anharmonicities and therefore strong vibrational mode–mode couplings. In addition, the electronic degeneracy at the conical intersection results in a complete breakdown of the Born-Oppenheimer (BO) approximation [46]. Therefore, conical intersections often dominate the short-time (10–100 fs) excited-state dynamics in polyatomic molecules [44–49].

The strong non-BO effects and the strong coupling of vibrational degrees of freedom render the theoretical modeling of the dynamics near conical intersections challenging. A possible strategy is the construction of reduced-dimensional models that incorporate just the most relevant vibrational modes of the conical intersection (minimally, the two vectors spanning the branching space of the conical intersection) which are selected with exploratory ab initio electronic-structure calculations [46]. However, the construction of such few-state few-mode models (usually in a diabatic electronic representation) can be time-consuming, and the numerical solution of the time-dependent quantum equation of motion can be challenging when more than a few strongly coupled vibrational degrees of freedom are involved, albeit the multiconfiguration time-dependent Hartree (MCTDH) method [50–52] and, more recently developed, matrix-product-state (MPS) [53–55] and tensor-train network (TTN) methods [56–59] have become powerful tools for the computation of the quantum mechanical time evolution of systems with many nonseparable nuclear degrees of freedom.

An attractive alternative to fully quantum mechanical descriptions are mixed quantum-classical models in which the nuclear motion is described by classical mechanics, while a quantum mechanical description is retained for the electrons. In view of typically large-amplitude nuclear motions in excited electronic states and large vibrational excess energies generated by radiationless transitions, a classical description of the nuclear motion seems justified according to the correspondence principle. From the computational point of view, classical mechanics scales only linearly with the number of nuclear degrees of freedom, in contrast to the exponential scaling of numerical quantum dynamics. Moreover, classical trajectories can be propagated by calculating the electronic energies, gradients, and nonadiabatic couplings (NACs) "on the fly" with ab initio electronic-structure methods [60–65]. On the other hand, photon absorption and emission processes as well as radiationless transitions between electronic states are inherently quantum mechanical phenomena and their modeling via classical mechanics is nontrivial.

The approximation of nonadiabatic (i.e., non-BO) quantum dynamics by mixed quantum-classical schemes is not unique, and there exists a wide variety of approximate mixed quantum-classical computational methods. Broadly speaking, the mixed quantum-classical schemes can be classified into quasi-classical methods and semi-classical methods.

1.2 | Quasi-Classical Trajectory Methods

In the quasi-classical descriptions, quantum wave packets are approximated by swarms of independent classical trajectories, which excludes the simulation of quantum interference effects. The basis of all quasi-classical descriptions is the classical path

approximation [66]. The dynamics of the fast electrons are assumed to follow adiabatically the comparatively slow motion of the much heavier nuclei. In the context of molecular spectroscopy and photochemistry, the initial condition for the nuclear motion is typically given by one or a few quantized eigenstates in the electronic ground state of a molecular chromophore. The initial positions and momenta of the quasi-classical trajectories are typically stochastically sampled from a quasi-classical probability distribution, for example from the Wigner distribution [67] of the vibrational modes in the electronic ground state.

The quasi-classical methods differ in the manner in which the back-reaction of the electronic motion on the nuclear motion is taken into account. In the time-honored Ehrenfest approximation, the nuclear motion is driven by the gradient of the mean value of the electronic potentials [68, 69]. The Ehrenfest dynamics is very easy to implement as an ab initio direct dynamics method [61]. The performance of the Ehrenfest method depends strongly on the physics of the problem. In the context of nonadiabatic electron/nuclear dynamics, the Ehrenfest method generally performs well for "vertical" radiationless transitions, where the dynamics are confined to a limited range of nuclear geometries. A well-studied example is the radiationless decay of the excited states of the benzene cation [70]. The Ehrenfest method fails, on the other hand, if bifurcations of wave packets in nuclear coordinate space occur, for example in photochemical reactions. A multi-configuration extension of the Ehrenfest approximation was recently proposed by Shalashilin and coworkers and developed into a versatile direct-dynamics method [71].

The most widely employed quasi-classical approximation method for nonadiabatic dynamics is the trajectory surface-hopping (SH) method. The trajectory SH concept was first formulated by Tully and Preston [72], invoking the quasi-classical Landau-Zener (LZ) model [73] for the estimation of hopping probabilities. In 1990, Tully introduced the fewest-switches surface hopping (FSSH) algorithm [74] which soon was widely implemented as an ab initio on-the-fly simulation protocol [65]. In FSSH, each nuclear trajectory of the ensemble is propagated in time on a single adiabatic BO potential-energy surface by solving Newton's equation of motion. Transitions between electronic potential-energy surfaces are induced by nonadiabatic (NAC) elements and are taken into account by a probabilistic algorithm. The NAC elements are evaluated from the electronic wave function, which is propagated with the time-dependent Schrödinger equation along each trajectory [74].

Since the trajectories of the ensemble are propagated independently, the conservation of the total energy has to be enforced for each trajectory, usually by a rescaling of momenta along the NAC vector. By treating the electronic dynamics by the time-dependent Schrödinger equation and the nuclear dynamics by Newton's equation, the FSSH algorithm is not internally consistent. This inconsistency leads to the so-called lack-of-decoherence problem which can be mitigated by an empirical suppression of the overcoherence of the electronic wave function [65]. The most widely employed decoherence correction is that of Grannucci and Persico [75].

In FSSH, the hopping probabilities are calculated continuously in time along each trajectory, which can be a significant computational burden for large systems. Alternative variants of trajectory SH have been proposed in which SH is taken into account only when the energy gap between adjacent electronic states attains a local minimum. The LZ model in the adiabatic representation [76, 77] or SH with the Zhu-Nakamura formula [78, 79] are examples. The decoherence problem does not arise in these algorithms, since the coherent propagation of the electronic wave function is avoided. While the algorithms based on the Belyaev-Lebedev or Zhu-Nakamura formulas are generally less accurate than the FSSH algorithm, the gain in computational efficiency can be substantial for large systems [80].

Recently, algorithms of SH-type also have been derived from the so-called exact factorization (EF) ansatz proposed by Gross, Maitra, and coworkers [81–83]. Computational studies of the performance of EF-based trajectory SH methods were performed by Agostini and coworkers [84]. An insightful overview of various trajectory-based methods and their relationship to formally exact Bohmian dynamics can be found in an article by Tavernelli and coworkers [85].

A comprehensive discussion of the strengths and weaknesses of the various quasi-classical simulation algorithms is beyond the scope of this review, which is focused on nonlinear time-resolved spectroscopy. Benchmarking the accuracy of the various algorithms against each other or against more exact computational methods (as far as available) is currently a very active field of research. The reader is referred to a few representative recent studies [86–89].

1.3 | Semi-Classical Trajectory Methods

Turning to semi-classical approximations, the Gaussian wave-packet approach of Heller represents a seminal early development [90, 91]. In the so-called thawed-Gaussian approximation, the center of the semi-classical wave packet follows the equations of classical mechanics. Simple equations of motion for the width and the phase of the wave packet are obtained by a local harmonic expansion of the electronic potential around the center of the moving wave packet [90]. By accounting for the phase of the wave packet, Heller's Gaussian trajectory dynamics can qualitatively describe wave-packet interference effects, which are, for example, the origin of vibrational fine structure in electronic spectra [92]. Heller's thawed-Gaussian approximation was recently implemented as an ab initio direct dynamics method for the calculation of linear and nonlinear electronic spectra [93, 94]. In the so-called frozen-Gaussian approximation of Heller, multiple Gaussians of fixed width are employed as a trajectory-driven basis set to describe the dynamics of wave packets on general potentials [95]. Ben-Nun and Martinez extended this approach to nonadiabatic dynamics in the ab initio multiple-spawning (AIMS) formalism [96]. The multiple-cloning approach of Shalashilin and coworkers [97] and the variational multi-configuration Gaussian wave-packet (vMCG) method of Worth and Burghardt [98] are related methods.

An alternative approach to semi-classical dynamics is derived from the Feynman path-integral representation of the quantum propagator by applying the stationary-phase approximation. The van Vleck-Gutzwiller [99] and Herman-Kluk [100] propagators

are the most well-explored examples for semi-classical dynamics on single potential-energy surfaces. The semi-classical description of nonadiabatic multi-state dynamics is particularly challenging because transitions between discrete electronic states are inherently of quantum nature. The iconic Meyer-Miller classical electron model [101] set the stage for developments in semi-classical nonadiabatic dynamics, which continue until today. Stock and Thoss [102] generalized the classical electron model by the semi-classical mapping approach, which is formulated in the framework of Schwinger's representation of angular momentum [103]. The semi-classical mapping concept is not unique, and several versions and implementations of the semi-classical mapping approach exist [104]. A recent improvement is the spin-mapping formalism of Runeson and Richardson [105]. The development of further improvements of semi-classical mapping methods for multi-state quantum dynamics is currently a very active field of research [106–110].

Another semi-classical formulation suitable for the description of nonadiabatic multi-state quantum dynamics is the quantum-classical Liouville equation (QCLE) [111]. The QCLE is derived from the quantum Liouville equation by taking the partial Wigner transform of the electron-nuclear density matrix with respect to the nuclear degrees of freedom and treating the nuclear motion in the semi-classical limit. By retaining the quantum description of the electrons, the QCLE can rigorously account for electronic coherences. The QCLE can alternatively be derived by the linearization of the forward-backward action in the influence functional of the path-integral representation of the electron-nuclear density matrix [112].

1.4 | Doorway-Window Approximation

Given any of these trajectory-based methods for the simulation of coupled electronic-nuclear dynamics, the calculation of nonlinear time-resolved spectra is still a formidable task. Adopting the perturbative approach to nonlinear optics [113], the third-order polarization is given by the triple convolution of the third-order nonlinear dipole response function with the electric fields of the laser pulses [8]. The third-order nonlinear dipole response function carries the complete information on the system dynamics in the absence of external fields and can be decomposed into specific spectroscopic pathways which can be represented by Feynman diagrams [8]. With the advancement of computational facilities and theoretical algorithms, substantial progress has been achieved in the construction of on-the-fly protocols for the simulation of response functions for realistic molecular systems [30, 114–117]. Yet, the computation and storage of the nonlinear response functions depending on three time variables represent a considerable computational challenge in any ab initio on-the-fly approach. The simplifications of the doorway-window (DW) approximation are essential for developing computationally feasible ab initio protocols using either quasi-classical or semi-classical trajectory methods.

The DW approximation for TA PP spectra was introduced by Yan, Fried, and Mukamel [118–120]. In the initial derivations, the excited-state absorption (ESA) contribution to the TA PP signal was neglected. Later on, the DW approximation was extended to the calculation of time-resolved fluorescence spectra [121–126] as well as to femtosecond coherence spectra [127]. Novoderezhkin et al. as well as Balzer and Stock extended the DW description to include ESA and simulated TA PP signals for a number of systems [128–130]. The DW framework as an approximation scheme was also used to calculate nonlinear response functions themselves [131–135]. The DW approximation has been generalized to overlapping pulses (via time-dependent doorway operators [136–138]) and the DW approximation was extended to sequential three-pulse photon-echo signals [139, 140], to six-wave-mixing pump-dump-probe signals [141] as well as to TA PP signals [142–144] and to electronic 2D signals [145, 146] evaluated with strong (nonperturbative) laser pulses. Tanimura and Mukamel developed a formal scheme for the description of doorway and window wave packets for Brownian oscillator models beyond the weak-field limit, and they discussed the domain of validity of the DW approximation [147, 148]. Related developments were also discussed by Olsina and Mancal [149].

The basic requirement of the DW approximation is the assumption of non-overlapping laser pulses; that is, laser pulses which are well separated in time. Moreover, the pulses have to be reasonably short compared to the characteristic time scale of the system dynamics, such that the nonadiabatic dynamics during the action of the pulses can be neglected. The first-principles simulation of the system dynamics is thus restricted to the time intervals between the pulses, but is not taken into account during the action of the pulses.

In recent applications of the trajectory-based DW protocol in the research groups of the authors, which are briefly reviewed in Chapters 3–5, a quasi-classical description of the dynamics was adopted. This limits the simulations to signals that are determined by populations of electronic states, such as the TA PP signals or the dependence of electronic 2D signals on the electronic population time. Two variants of SH were employed for the description of the quasi-classical dynamics, either Tully's FSSH algorithm [74] or a LZSH algorithm based on the Belyaev-Lebedev formula [77]. Any other of the quasi-classical approximation methods discussed above could have been used.

The systematic implementation of the DW approximation with semi-classical protocols has not yet been worked out. While the sampling of initial conditions and the sum over trajectories may be considerably more difficult to converge with semi-classical algorithms, such implementations would allow the simulation of general N-wave-mixing signals and/or the simulation of signals that are sensitive to electronic coherences, for example, those that are generated when wave packets move through same-symmetry conical intersections.

2 | Optically-Detected Signals

2.1 | General Expressions for Four-Wave-Mixing Signals

FWM experiments detect the third-order laser-induced polarization $P_{\mathbf{k}}(t)$ radiating in a specific phase-matching direction $\mathbf{k}$ [8, 150]. Typically, $P_{\mathbf{k}}(t)$ is produced by the interaction of the material system under study with the first three laser pulses

$E_j(t-\bar{t}_j)$ ($j=1,2,3$, $\bar{t}_j$ are the arrival times of the pulses which for symmetric pulse envelopes $E_j(t)=E_j(-t)$ assumed herein coincide with the pulse centers) possessing the wave vectors $\mathbf{k}_j$ and is measured in the non-rephasing ($\alpha=\mathrm{NR}$, $\xi_\alpha=1$) or rephasing ($\alpha=\mathrm{R}$, $\xi_\alpha=-1$) phase-matching direction [8, 150].

$$\mathbf{k}_\alpha=\xi_\alpha(\mathbf{k}_1-\mathbf{k}_2)+\mathbf{k}_3. \tag{1}$$

The FWM signal I_α is detected by heterodyning $P_{\mathbf{k}_\alpha}(t)$ with the local-oscillator field $E_4(t-\bar{t}_4)$ [8, 150]:

$$I_\alpha=\mathrm{Im}\int dt P_{\mathbf{k}_\alpha}(t)E_4^*(t-\bar{t}_4). \tag{2}$$

This signal contains information on both absolute value and phase of the complex-valued polarization $P_{\mathbf{k}_\alpha}(t)$, and is therefore sensitive to electronic coherence effects [151].

FWM signals consist of ground-state bleach (GSB), stimulated emission (SE), and excited-state absorption (ESA) contributions and can be evaluated in terms of the total third-order response functions $R_{\alpha k}(t_3,t_2,t_1)$ ($k=0,\mathrm{I},\mathrm{II}$ correspond to the GSB, SE, and ESA contributions) as follows [8, 30, 151]:

$$I_\alpha(\tau,T,\tau_t)\sim\mathrm{Re}\sum_{k=0,\mathrm{I},\mathrm{II}}\int_{-\infty}^{\infty}dt\int_0^\infty dt_3\int_0^\infty dt_2\int_0^\infty dt_1E_1(t+\tau+T-t_3-t_2-t_1)\times \tag{3}$$

$$E_2(t+T-t_3-t_2)E_3(t-t_3)E_4(t-\tau_t)e^{i\xi_\alpha\omega_{pu}(t_1-\tau)}e^{i\omega_{pr}(t_3-\tau_t)}R_{\alpha k}(t_3,t_2,t_1).$$

Here the arrival times of the pulses are conventionally parameterized as

$$\bar{t}_1=-T-\tau,\ \bar{t}_2=-T,\ \bar{t}_3=0,\ \bar{t}_4=\tau_t \tag{4}$$

where τ, T, and τ_t are referred to as excitation, population, and detection times, respectively. This notation is used throughout this article. For simplicity and clarity, the carrier frequencies ω_j and durations τ_j of sequential pairs of pulses are taken the same,

$$\omega_1=\omega_2=\omega_{pu},\quad \omega_3=\omega_4=\omega_{pr} \tag{5}$$

$$\tau_1=\tau_2=\tau_{pu},\quad \tau_3=\tau_4=\tau_{pr} \tag{6}$$

(the subscripts "*pu*" and "*pr*" denote pump and probe pulses). The dynamical properties of the material system under study are determined by its Hamiltonian (see Appendix A) which, in turn, fully specifies the third-order response functions $R_{\alpha k}(t_3,t_2,t_1)$ (see Appendix B). All optical signals considered in this work can be evaluated as a special case of Equation (3).

2.2 | Quantum Doorway-Window Representation of Four-Wave-Mixing Signals

The third-order response functions can be formally represented in DW format as [131–133, 140].

$$R_{\alpha k}(t_3,t_2,t_1)=a_k\mathrm{Tr}\left[\mathcal{W}_k(t_3)\mathscr{L}(t_2)\mathcal{D}_\alpha(t_1)\right]. \tag{7}$$

Here the doorway and window operators, $\mathcal{D}_\alpha(t_1)$ and $\mathcal{W}_k(t_3)$, describe evolution of the system in electronic coherence during the times t_1 and t_3, while the propagator $\mathscr{L}(t_2)$ governs nonadiabatic evolution of the system in electronic population during the time t_2. Note that the doorway operator is the same for the GSB, SE and ESA signals. Note also that the window operators do not depend on the phase-matching condition (Equation (1)). The numerical factors

$$a_k=\begin{bmatrix}1, & k=0,\mathrm{I}\\ -1, & k=\mathrm{II}\end{bmatrix}$$

denote the sign of the corresponding term: According to the chosen convention, the GSB ($k=0$) and SE ($k=\mathrm{I}$) contributions are (predominantly) positive, while the ESA contribution ($k=\mathrm{II}$) is (predominantly) negative [30, 151].

The DW representation of the nonlinear response functions generates the DW representation of the FWM signal of Equation (3). The latter is constructed under two assumptions: (i) the pulses 2 and 3 are well temporally separated ($T>\tau_{pu},\tau_{pr}$), so that we can neglect the transient effects decaying on the timescale of τ_{pu} and τ_{pr}. (ii) the pulses are short on the system dynamics timescale, so that we can neglect electronic population evolution during τ_{pu} and τ_{pr}. Changing the integration variables

$$t=t'+t_3,\ t_2=t'+T-t_2'$$

and implementing the above assumptions, the FWM signal of Equation (3) can be recast in the DW form [30],

$$I_\alpha(\tau,T,\tau_t)\sim\mathrm{Re}\sum_{k=0,\mathrm{I},\mathrm{II}}a_k\mathrm{Tr}\left[W_k(\tau_t)\mathscr{L}(T)D_\alpha(\tau)\right], \tag{8}$$

where

$$D_\alpha(\tau)=\int_{-\infty}^{\infty}dt_2'\int_0^\infty dt_1E_2(t_2')E_1(t_2'+\tau-t_1)e^{i\xi_\alpha\omega_{pu}(t_1-\tau)}\mathcal{D}_\alpha(t_1) \tag{9}$$

$$W_k(\tau_t)=\int_{-\infty}^{\infty}dt'\int_0^\infty dt_3E_4(t'+t_3-\tau_t)E_3(t')e^{i\omega_{pr}(t_3-\tau_t)}\mathcal{W}_k(t_3). \tag{10}$$

2.3 | Classical Doorway – Window Representation of Four-Wave-Mixing Signals

It was proposed already in Refs [118–120] that the DW framework can be combined with classical or semi-classical trajectory methods. This idea has been further exploited and extended in Refs [70, 152–159], in which PP signals of several model systems were simulated. The general quantum FWM signal in the DW representation, Equations (8–10), can also be recast in a form suitable for on-the-fly classical trajectory methods by making the following approximations (see Refs [160, 161]):

i. The DW operators $\mathcal{D}_\alpha(t_1)$ and $\mathcal{W}_k(t_3)$ become functions in nuclear phase space, $\mathcal{D}_\alpha(t_1,\mathbf{R},\mathbf{P})$ and $\mathcal{W}_k(t_3,\mathbf{R},\mathbf{P})$, where $\mathbf{P}$ are the momenta conjugated to the nuclear coordinates $\mathbf{R}$.

ii. Radiative transitions are treated within the classical Condon approximation [153, 157, 162].

iii. The initial vibrational distribution in the electronic ground state is replaced by the Wigner distribution $\rho_g^{Wig}(\mathbf{R},\mathbf{P})$ [163].

iv. The trace Tr[…] in Equation (8) is evaluated by Monte Carlo (MC) importance sampling $\langle \ldots \rangle_{\mathrm{MC}}$. The initial conditions $\mathbf{R},\mathbf{P}$ of the trajectories are sampled from the ground-state Wigner distribution $\rho_g^{Wig}(\mathbf{R},\mathbf{P})$. The sum over the electronic states is replaced by importance sampling from the oscillator strength distribution of the electronic states. More details can be found in Appendix G.

v. The quantum evolution governed by the propagator $\mathscr{L}(T)$ is replaced by the evolution of nuclear coordinates along (quasi) classical trajectories, $\mathbf{R}(T),\mathbf{P}(T)$.

To turn these approximations into operational expressions and simulation protocols, it is useful to partition the molecular electronic states into three manifolds, {0}, {I}, {II} (see Appendix A). Manifold {0} consists of the electronic ground state $|\,g\,\rangle$; manifold {I} contains lower-lying excited electronic states $|\,e\,\rangle$ which are bright from the electronic ground state, as well as nearby dark electronic states which are nonadiabatically coupled to them; {II} comprises higher-lying electronic states $|\,f\,\rangle$ which can be probed by laser pulses from manifold {I}. We denote the potential energy functions of these states as $V_g(\mathbf{R})$, $V_e(\mathbf{R})$, $V_f(\mathbf{R})$ and specify the energy differences $U_{eg}(\mathbf{R}) = V_e(\mathbf{R}) - V_g(\mathbf{R})$ and $U_{fe}(\mathbf{R}) = V_f(\mathbf{R}) - V_e(\mathbf{R})$. We also introduce the transition dipole moment (TDM) operators $\boldsymbol{\mu}_{\mathrm{I},0}$, $\boldsymbol{\mu}_{\mathrm{II,I}}$ describing optical transitions between the manifolds and define their electronic matrix elements, $\mu_{ge}(\mathbf{R}) = \langle g|\,\boldsymbol{\mu}_{0,\mathrm{I}}\,|e\rangle$ and $\mu_{fe}(\mathbf{R}) = \langle f|\,\boldsymbol{\mu}_{\mathrm{II,I}}\,|e\rangle$. Then approximations (i) and (ii) yield the following explicit expressions [153, 157, 162].

$$\langle g|\, e^{iH_0 t_3}\boldsymbol{\mu}_{0,\mathrm{I}} e^{-iH_1 t_3}\,|e\rangle \approx e^{iU_{ge}(\mathbf{R})t_3}\boldsymbol{\mu}_{ge}(\mathbf{R}), \tag{11}$$

$$\langle f|\, e^{iH_{\mathrm{II}} t_3}\boldsymbol{\mu}_{\mathrm{II,I}} e^{-iH_1 t_3}\,|e\rangle \approx e^{iU_{fe}(\mathbf{R})t_3}\boldsymbol{\mu}_{fe}(\mathbf{R}), \tag{12}$$

where H_k is the molecular Hamiltonian in manifold k (see Appendix A). With the above approximations, Equations (8–10) are transformed into the classical DW formula for the FWM signal [160, 161]:

$$I_\alpha(\tau,T,\tau_t) \sim \mathrm{Re}\sum_{k=0,\mathrm{I,II}} a_k \left\langle W_k\big(\mathbf{R}(T),\mathbf{P}(T);\tau_t\big) D_\alpha(\mathbf{R},\mathbf{P};\tau)\right\rangle_{\mathrm{MC}}. \tag{13}$$

Here $D_\alpha(\mathbf{R},\mathbf{P};\tau)$, $\alpha = \mathrm{R}/\mathrm{NR}$, is the doorway function. It is defined by Equation (9) which, according to Equations (B5) and (B6) of Appendix B, assumes the form

$$\mathcal{D}_\alpha(t_1) = \big(\mathbf{s}_1\cdot\boldsymbol{\mu}_{ge}(\mathbf{R})\big)\big(\mathbf{s}_2\cdot\boldsymbol{\mu}_{ge}(\mathbf{R})\big) e^{-i\xi_\alpha U_{eg}(\mathbf{R})t_1}\rho_g^{Wig}(\mathbf{R},\mathbf{P}). \tag{14}$$

The window functions $W_k(t_3,\mathbf{R},\mathbf{P})$ are defined through Equation (10). Taking into account the explicit expressions (B7–B9) of Appendix B, we obtain

$$\mathcal{W}_0(t_3) = \sum_{e'} \big(\mathbf{s}_3\cdot\boldsymbol{\mu}_{ge'}(\mathbf{R})\big)\big(\mathbf{s}_4\cdot\boldsymbol{\mu}_{ge'}(\mathbf{R})\big) e^{-iU_{e'g}(\mathbf{R})t_3}, \tag{15}$$

$$\mathcal{W}_{\mathrm{I}}(t_3) = \big(\mathbf{s}_3\cdot\boldsymbol{\mu}_{ge}(\mathbf{R})\big)\big(\mathbf{s}_4\cdot\boldsymbol{\mu}_{ge}(\mathbf{R})\big) e^{-iU_{eg}(\mathbf{R})t_3}, \tag{16}$$

$$\mathcal{W}_{\mathrm{II}}(t_3) = \sum_f \big(\mathbf{s}_3\cdot\boldsymbol{\mu}_{ef}(\mathbf{R})\big)\big(\mathbf{s}_4\cdot\boldsymbol{\mu}_{ef}(\mathbf{R})\big) e^{-iU_{fe}(\mathbf{R})t_3}. \tag{17}$$

Here $\mathbf{s}_j$ is the unit vector specifying the linear polarization of pulse j (see Appendix A).

It is convenient to distinguish between the nuclear dynamics in manifolds {0} and {I} and denote the respective nuclear trajectories as $\mathbf{R}_g(t),\mathbf{P}_g(t)$ and $\mathbf{R}_e(t),\mathbf{P}_e(t)$. Hence in Equation (13)

$$D_\alpha(\mathbf{R},\mathbf{P};\tau) \equiv D_\alpha\big(\mathbf{R}_g,\mathbf{P}_g;\tau\big), \tag{18}$$

$$W_0\big(\mathbf{R}(T),\mathbf{P}(T);\tau_t\big) \equiv W_0\big(\mathbf{R}_g(T),\mathbf{P}_g(T);\tau_t\big), \tag{19}$$

$$W_k\big(\mathbf{R}(T),\mathbf{P}(T);\tau_t\big) \equiv W_k\big(\mathbf{R}_e(T),\mathbf{P}_e(T);\tau_t\big),\ k=\mathrm{I},\mathrm{II}. \tag{20}$$

The classical DW representation of the general FWM signal of Equation (13) is the key to the evaluation of these signals through classical trajectories, and the corresponding simulation protocols are summarized in Appendix G.

In deriving Equations (14–17), NACs within manifold {I} were neglected during the excitation time τ and the detection time τ_t. In this approximation, the dynamics of the optical electronic coherences during τ and τ_t is determined by the time-dependent energy gaps and the optical dephasing constant. In future improvements of the theory, the optical coherences during the excitation and detection times should be propagated with inclusion of nonadiabatic couplings using a suitable semi-classical method.

3 | Transient Absorption Pump-Probe Spectra

3.1 | UV Pump UV Probe Spectra

The early femtosecond time-resolved experiments of Zewail and coworkers on small molecules were based on photofragment detection [164, 165]. They stimulated the development of classical models for the photodissociation of diatomic (NaI) or triatomic (ICN) molecules [120, 166–168]. It was realized that the classical description works very well in this context because the wave packet prepared by the pump pulse is narrow, the de Broglie wavelength is short, and the width of the curve-crossing region (in NaI) is narrow.

The general quantum mechanical description of TA PP spectra was developed by Mukamel and coworkers in the framework of third-order density-matrix perturbation theory [118, 119, 169] and by Pollard, Lee, and Mathies in the framework of third-order wave-function perturbation theory [170, 171]. In the early articles of Mukamel and coworkers, the DW approximation was derived, and the classical limit of the DW approximation was formulated [118, 119]. Alternative classical descriptions of pump-probe or photon-echo spectra were developed, for example, by Stock [70], Martens and coworkers [155], Cina and coworkers [157, 172, 173] and Loring and coworkers [174, 175]. Stock and Miller developed a semiclassical theory based on the Meyer-Miller classical electron model [176], emphasizing ultrafast nonadiabatic dynamics

at conical intersections at an early stage. Alternative semi-classical descriptions were developed that were based on the Van Vleck-Gutzwiller propagator [177], the forward-backward initial value representation [178], linearizations of path integrals [179], the quasi-classical Langevin equation (QCLE) [180] or the semi-classical mapping model of Stock and Thoss [106, 181]. Vanicek and coworkers implemented Heller's thawed Gaussian wave-packet approximation [90] for the ab initio calculation of time-resolved spectra [182]. While all these semi-classical descriptions result in trajectory-based computational protocols, the discussion in the present article is restricted to quasi-classical trajectory approximations, as explained in the introduction.

In the TA PP signal, the material system experiences first two interactions with the pump pulse. Hence $\mathbf{k}_1 = \mathbf{k}_2$ in Equation (1), one cannot distinguish between rephasing and non-rephasing phase-matching directions, and the TA PP signal is obtained as the sum of rephasing and non-rephasing signals. The classical DW expression for the integral TA PP signal $I^{int}(\omega_{pu}, \omega_{pr}, T)$ as a function of the population time T and the probe frequency ω_{pr} is directly obtained from Equation (13),

$$I^{int}(\omega_{pu}, \omega_{pr}, T) = I_{\mathrm{R}}(0, T, 0) + I_{\mathrm{NR}}(0, T, 0) \tag{21}$$

$$= \mathrm{Re} \sum_{k=0,\mathrm{I},\mathrm{II}} a_k \left\langle W_k(\omega_{pr}, \mathbf{R}(T), \mathbf{P}(T), 0) D(\omega_{pu}, \mathbf{R}_g, \mathbf{P}_g) \right\rangle_{\mathrm{MC}}$$

where

$$D(\omega_{pu}, \mathbf{R}_g, \mathbf{P}_g) = D_{\mathrm{R}}(\omega_{pu}, \mathbf{R}_g, \mathbf{P}_g; 0) + D_{\mathrm{NR}}(\omega_{pu}, \mathbf{R}_g, \mathbf{P}_g; 0) \tag{22}$$

is the total (R + NR) doorway function.

If the nonadiabatic coupling elements $H_{0,\mathrm{I}}$ and $H_{\mathrm{I},\mathrm{II}}$ (see Appendix A) can be neglected on the timescale of interest, the time evolution of the molecular system in manifolds {0} and {I} is independent. The explicit formulas for the DW operators read in this case [160].

$$D(\omega_{pu}, \mathbf{R}_g, \mathbf{P}_g) = E_{pu}^2(\omega_{pu} - U_{eg}(\mathbf{R}_g)) (\mathbf{s}_{pu} \cdot \boldsymbol{\mu}_{ge}(\mathbf{R}_g))^2 \rho_g^{Wig}(\mathbf{R}_g, \mathbf{P}_g), \tag{23}$$

$$W_0(\omega_{pr}, \mathbf{R}_g(T), \mathbf{P}_g(T)) = \sum_{e'} E_{pr}^2(\omega_{pr} - U_{e'g}(\mathbf{R}_g(T))) (\mathbf{s}_{pr} \cdot \boldsymbol{\mu}_{ge'}(\mathbf{R}_g(T)))^2, \tag{24}$$

$$W_{\mathrm{I}}(\omega_{pr}, \mathbf{R}_e(T), \mathbf{P}_e(T)) = E_{pr}^2(\omega_{pr} - U_{e(T)g}(\mathbf{R}_e(T))) (\mathbf{s}_{pr} \cdot \boldsymbol{\mu}_{ge(T)}(\mathbf{R}_e(T)))^2, \tag{25}$$

$$W_{\mathrm{II}}(\omega_{pr}, \mathbf{R}_e(T), \mathbf{P}_e(T)) = \sum_f E_{pr}^2(\omega_{pr} - U_{fe(T)}(\mathbf{R}_e(T))) (\mathbf{s}_{pr} \cdot \boldsymbol{\mu}_{e(T)f}(\mathbf{R}_e(T)))^2. \tag{26}$$

Here D is the classical doorway distribution and W_k ($k = 0, \mathrm{I}, \mathrm{II}$) are the window functions for the GSB, SE and ESA contributions to the integral TA PP signal,

$$\mathbf{s}_1 = \mathbf{s}_2 = \mathbf{s}_{pu}, \ \mathbf{s}_3 = \mathbf{s}_4 = \mathbf{s}_{pr} \tag{27}$$

define the polarizations of the pump and probe pulses,

$$E_\alpha(\omega) = \int_{-\infty}^{\infty} d\omega e^{-i\omega t} E_\alpha(t) \tag{28}$$

are the Fourier transforms of the pulse envelopes, and the notation $e(T)$ implies that a trajectory launched at $t = 0$ in a state e of manifold {I} can end up at time $t = T$ in a state $e(T) \neq e$.

The dispersed TA PP signal is evaluated through the Fourier transform of Equation (13) with respect to the detection time τ_t

$$I^{dis}(\omega_{pu}, \omega_t, T) = I_{\mathrm{R}}(0, T, \omega_t) + I_{\mathrm{NR}}(0, T, \omega_t) \tag{29}$$

where

$$I_\alpha(0, T, \omega_t) = \int d\tau_t e^{i\omega_t \tau_t} I_\alpha(0, T, \tau_t). \tag{30}$$

In contrast to the integral PP signal, the dispersed PP signal depends on the optical dephasing rate, which determines the free induction decay of the third-order polarization (see Appendix D). In the DW approximation, it is assumed that the duration of the probe pulse is short compared to the time constant of optical dephasing. In the current implementation of the theory, the dephasing time constant is an empirical parameter. Dephasing time constants typically are on the order of a few tens of femtoseconds for polyatomic molecules in the gas phase and are possibly shorter for chromophores in solution at room temperature. This restricts the DW approximation for dispersed signals to rather short probe pulses in the few-fs regime. On the other hand, short probe pulses, anyway, are necessary for dispersed PP spectroscopy because the width of the frequency spectrum of the dispersed signal is inversely proportional to the duration of the probe pulse. The equations defining the DW approximation for the dispersed TA PP signal are given in Appendix D.

The DW formalism for the simulation of TA PP signals is also applicable in the more general case, in which nonadiabatic couplings between manifolds {0} and {I} cannot be neglected on the timescale of the experiment [183]. In this situation, the general expressions for the integral (21) and dispersed (29) signals remain valid, but the explicit form of the window functions is modified (see Appendix E).

For the evaluation of TA PP signals, the trajectories with initial positions and momenta $\mathbf{R}_g, \mathbf{P}_g$ are sampled from the Wigner distribution $\rho_g^{Wig}(\mathbf{R}_g, \mathbf{P}_g)$, while the initial populations of the states e in manifold {I} are sampled according to their oscillator strengths. Alternatively, $\mathbf{R}_g, \mathbf{P}_g$, and e can be sampled from the doorway function $D(\mathbf{R}_g, \mathbf{P}_g)$ (see Appendix G for a detailed discussion of the different options). For the evaluation of the GSB signal, $\mathbf{R}_g, \mathbf{P}_g$ are propagated on the PE surface of the electronic ground state, yielding the nuclear positions and momenta $\mathbf{R}_g(T)$, $\mathbf{P}_g(T)$ of the trajectory on the ground-state surface at detection time T. For the SE and ESA signals, the positions and momenta of the trajectories are propagated

in manifold {I} with a SH algorithm which takes nonadiabatic transitions within manifold {I} into account. Non-Condon effects for electronic transitions from manifold {0} to manifold {I} and from manifold {I} to manifold {II} are taken into account via the dependence of the TDMs on the nuclear coordinates. $\mathbf{R}_e(T)$, $\mathbf{P}_e(T)$ in Equations (25), (26) denote the nuclear positions and momenta in electronic state e after propagation in manifold {I} up to detection time T. The TDMs $\boldsymbol{\mu}_{ge(T)}\left(\mathbf{R}_e(T)\right)$ are evaluated for the active excited state at the geometry of the trajectory at the detection time T. In the ESA contribution, $\boldsymbol{\mu}_{e(T)f}\left(\mathbf{R}_e(T)\right)$ denotes the TDM from the excited state $e(T)$ in manifold {I} to state f in manifold {II} at detection time T. It should be noted that the electronic states of manifold {II} enter only through their TDMs. No trajectories have to be propagated in manifold {II}. Therefore, nonadiabatic couplings in manifold {II} need not be evaluated. Below we give three illustrations of the application of the above formalism for the evaluation of TA PP spectra of polyatomic chromophores.

The ultrafast nonadiabatic dynamics in the S_1, S_2 and S_3 excited singlet states of the pyrazine molecule may be one of the theoretically most thoroughly investigated excited-state dynamics of a polyatomic molecule in the literature. Pyrazine therefore was chosen as a representative example for the application of most of the computational methods of this review. The ultrafast relaxation dynamics within the valence excited states of pyrazine triggered by the optical excitation of the bright $B_{2u}(\pi\pi^*)$ state is well understood from numerous previous computational studies [184–193]. The imaging of the time-resolved electronic population dynamics of pyrazine with PP spectroscopies has been computationally explored for various ab initio based reduced-dimensional models [47, 184, 191, 193]. Pyrazine possesses four low-lying valence excited singlet states, one state of $\pi\pi^*$ character (B_{2u}) and three states of $n\pi^*$ character (B_{3u}, A_u, B_{2g}). The population of the optically prepared B_{2u} state decays on a time scale of about 20 fs to the B_{3u} state through a conical intersection. The B_{3u} state is in turn coupled to the A_u state through another conical intersection, resulting in rapid $B_{3u} - A_u$ population exchange which is driven by the vibrational excess energy available from the $B_{2u} \rightarrow B_{3u}$ relaxation. The B_{2g} state is a dark state and is not populated by relaxation from the bright B_{2u} state. This state therefore is not of relevance for the spectroscopy of the valence excited states of pyrazine. The relaxation of the valence excited states to the electronic ground state occurs on a time scale of the order of 20 ps [194] and therefore is negligible in the time range of interest (≈ 100 fs).

The computational protocol defined by Equations (21–26) was implemented for the simulation of TA PP signals of pyrazine [160]. The second-order Møller-Plesset (MP2) method was used for the electronic ground state and the ADC(2) (algebraic-diagrammatic construction of second order) method [195] was used for the excited electronic states. The harmonic Wigner distribution of the electronic ground state was constructed from the MP2 Hessian obtained with the aug-cc-pVDZ basis set. Trajectories were propagated on the ground-state PE surface (MP2) and on the coupled PE surfaces the manifold {I} of valence excited states (ADC(2)) with the cc-pVDZ basis set. The classical equations of motion were integrated with the velocity-Verlet algorithm using a time step of 0.5 fs. Nonadiabatic transitions in manifold {I} were taken into account by a LZSH algorithm [76, 77]. For the evaluation of the ESA signal, the next 30 electronic states with vertical excitation energies up to ≈ 10 eV were included in manifold {II}. As described in [160], the convergence of the signals with respect to the sampling by trajectories was explored in some detail. The results shown in Figure 1 were obtained with 200 trajectories in the electronic ground state and 300 trajectories in manifold {I}. The computationally more expensive ESA signal was evaluated for 200 trajectories.

Figure 1 displays the GSB, SE and ESA contributions and the total integral signal, computed for pump and probe pulses of 5 fs duration. The GSB signal is essentially stationary and carries little dynamical information. The SE signal, on the contrary, monitors the nonadiabatic wave-packet dynamics in manifold {I} through its projection on the ground-state PE surface. The initial population of the bright B_{2u} state gives rise to a strong SE signal which shifts to the red as the wave packet moves towards the minimum of the B_{2u} PE surface. At about 20 fs, the wave packet hits the B_{2u}/B_{3u} conical intersection, where it bifurcates. A fraction of the wave packet remains on the (adiabatic) B_{2u} surface and is reflected. The other fraction of the wave packet converts to the adiabatic B_{3u} surface, from which weak SE occurs at probe frequencies of ≈ 3.0 eV (see Figure 1) through vibronic intensity borrowing from the diabatic B_{2u} state. The SE intensity beyond 50 fs exhibits oscillations which reflect $B_{3u} - A_u$ nonadiabatic transitions driven by the high vibrational excess energy. This aspect of the dynamics will be analyzed in more detail in the context of the 2D signal in Section 4 below.

The vibrational signatures in Figure 1 can be associated with the two dominant tuning modes of the B_{2u}/B_{3u} conical intersection, ν_1 and ν_{6a}. The ultrafast nonadiabatic transition from the initially populated B_{2u} state to the B_{3u} state is also reflected in the ESA signal. When the pyrazine molecule is in the initial B_{2u} state, the ESA signal is located at a probe frequency between 5.0 and 6.0 eV. After the transition to the B_{3u} and A_u states, the ESA signal oscillates around probe frequencies near 4.5 eV, being spectrally separated from the SE signal (see Figure 1). The total signal is dominated by the (negative) ESA signal and the (positive) GSB signal.

A discussion of the simulated dispersed TA PP signal of pyrazine can be found in [160]. In contrast to the integral signal, the frequency resolution of the dispersed signal is not directly related to the duration of the probe pulse. On the other hand, the width of the spectrum of the probe pulse determines the spectral window of the dispersed signal. With 5 fs pulses, only a fraction of the dispersed signal of pyrazine can be observed. To cover the broad energy range of the excited-state dynamics of pyrazine, probe pulses in the range of 100 as are required (see [160] for more details).

Azomethane (Figure 2a) is the simplest azoalkane. It exhibits $S_1 \rightarrow S_0$ internal conversion on the timescale of several hundreds of femtoseconds [196–200]. The DW-SH simulations of the TA PP spectra of azomethane performed in [183] give an example of the application of the treatment of nonadiabatic dynamics at an $S_1 - S_0$ conical intersection described in Appendix E. The excited-state dynamics of azomethane was calculated at the XMS-CASPT2 (extended multistate multireference second-order

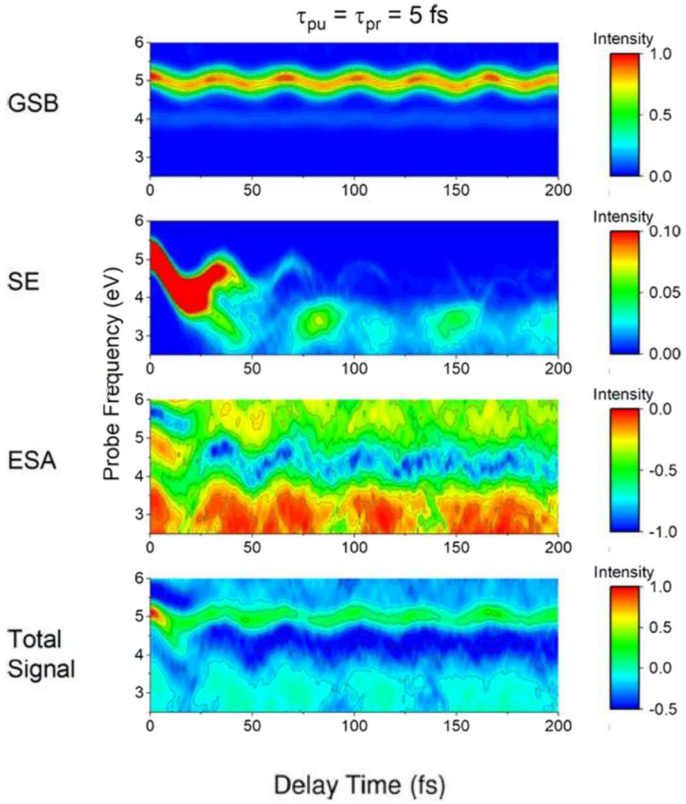

FIGURE 1 | GSB, SE, ESA contributions and total integral TA PP signal $I^{int}(\omega_{pu}, \omega_{pr}, T)$ of pyrazine as function of the probe pulse delay time T and probe pulse carrier frequency ω_{pr} for $\tau_j^{(p)} = 5$ fs durations of the PP pulses. The pump pulse ($\omega_{pu} = 5.2$ eV) is tuned into resonance with the $B_{2u}(\pi\pi^*)$ state. Adapted from [160]. Copyright American Chemical Society.

perturbation theory) level of the electronic-structure theory [201].

Figure 2b depicts the time evolution of the S_0 and S_1 populations. The S_1 state loses roughly half of its population within first 250 fs. The GSB signal in Figure 2d consists of the superposition of a "cold" component (the standard GSB signal) and a "hot" component (the GSB signal caused by the $S_1 \rightarrow S_0$ internal conversion). The cold component displays low-amplitude wavepacket motion in the electronic ground state and reflects the optically driven electronic transitions in the Franck-Condon region. The hot component exhibits erratic high-amplitude oscillations which reflect the large-amplitude nuclear motion triggered by the internal conversion from S_1 to S_0. The onset of the hot GSB signal in Figure 2d coincides with the appearance of ground-state population around 100 fs (Figure 2a).

The SE signal is shown in Figure 2e. It vanishes much faster than the S_1 population in Figure 2b. The reason is as follows. The S_1 population dynamics is governed by the $S_1 - S_0$ conical intersection, while the SE signal is sensitive not only to the conical intersection, but also to the TDMs. After the initial excitation, azomethane experiences central bond torsion which significantly reduces the TDM (Figure 2c). The TDM almost vanishes before the excited-state wavepacket reaches the $S_0 - S_1$ conical intersection. Hence the SE signal decays much faster than the S_1 population. The ESA signal (Figure 2f) is relatively strong at short T. The peak of the signal exhibits a red-shift (from 4.0 to 3.2 eV) within 50 fs. Beyond 50 fs, the peak of the signal returns to 4.0 eV and the intensity exhibits irregular oscillations. After about 230 fs, the ESA signal declines.

Assuming that the molecular system under study is fixed in space (e.g., immobilized in a polymer matrix or aligned by a static external field), one can consider polarization-sensitive signals $I^{int}_{s_{pu},s_{pr}}(\omega_{pu}, \omega_{pr}, T)$, where $s_{pu}, s_{pr} = X, Y, Z$ denote TDMs aligned along the corresponding axes of the laboratory frame (see Appendix C). This variant of TA PP spectroscopy is illustrated herein for a simple model dendrimer.

Dendrimers with branches consisting of phenylene-ethynylene units are of considerable interest due to their excellent photoharvesting and exciton-transport properties [202–206]. When the branches are of different lengths, the electronic excitation is localized on individual branches. Ultrafast excited-state energy transfer takes place from short branches (with higher excitation energies) to longer branches (with lower excitation energies). In [207], the DW-SH method was employed for the simulation of polarization-sensitive TA PP spectra of a typical phenylene-ethynylene dendrimer with meta-linked two-ring and three-ring branches (see Figure 3a). The on-the-fly SH simulations were performed with the FSSH algorithm [65, 74] at the TDDFT/CAM-B3LYP/6-31G level of electronic structure theory.

In our simulations, the dendrimer is aligned as shown in Figure 3a: The X-axis is parallel to the 3-ring unit, the Y-axis is perpendicular to the X-axis and lies within the molecular plane, and the Z-axis is perpendicular to the molecular plane. The blue

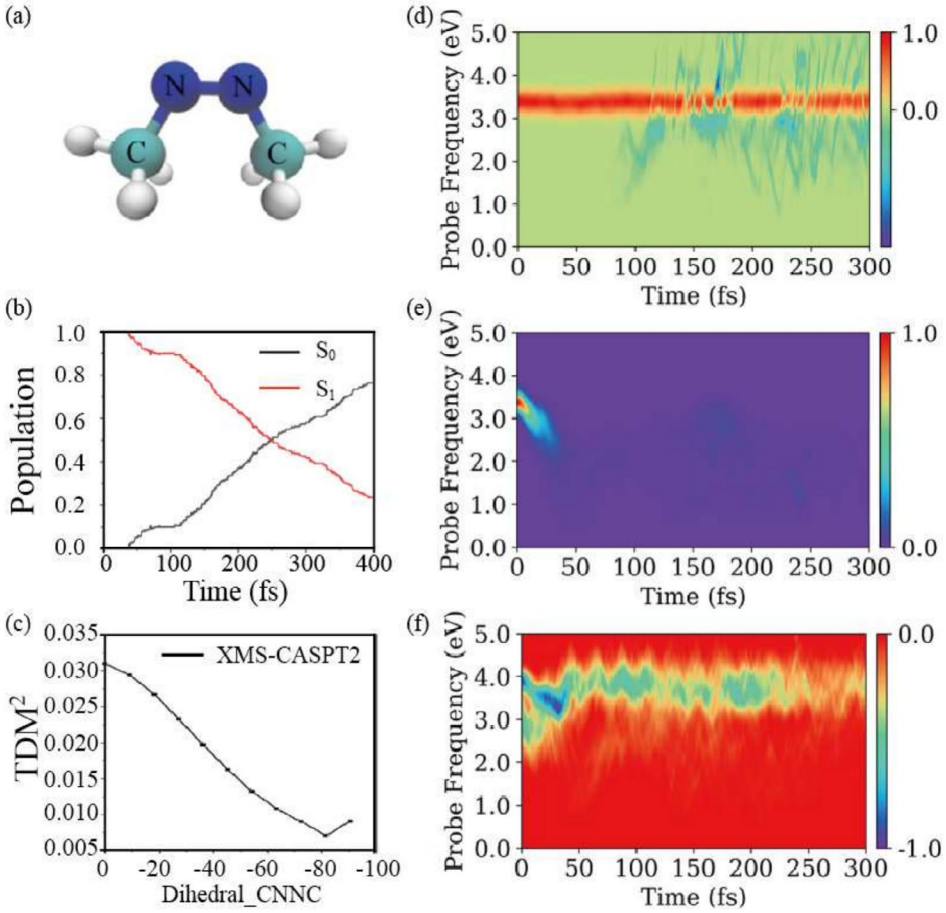

FIGURE 2 | (a) Structure of azomethane. (b) Time-dependent fractional occupations of the S_0 and S_1 electronic states of azomethane in nonadiabatic dynamics starting from the S_1 state. (c) Dependence of the TMD of azomethane on the central torsional angle. Normalized (d) GSB, (e) SE, and (f) ESA contributions to the integral TA PP signal of azomethane as a function of the pump-probe delay time T and the probe-pulse carrier frequency ω_{pr}. Duration of both pump and probe pulses is 5 fs. The carrier frequency ω_{pu} of the pump pulse is tuned into resonance with the $S_1(n\pi^*)$ state. Adapted from [183]. Copyright American Chemical Society.

arrows indicate the directions of the TDMs from S_0 to the three low-lying excited states. At the equilibrium geometry of the electronic ground state, the S_1 state (excitation energy 4.03 eV) is localized on the three-ring unit and the S_2 state (excitation energy 4.64 eV) is localized on the two-ring unit. After excitation of the S_1 state, no nonadiabatic dynamics takes place. After excitation to the S_2 state, on the contrary, the system undergoes fast internal conversion to the S_1 state (see Figure 3b-2), which is consistent with previous studies [208, 209]. This process corresponds to the energy transfer from the short-chain unit to the long-chain unit.

The TA PP spectra are evaluated with the pump and probe pulses of duration $\tau_{pu} = \tau_{pr} = 5$ fs for four combinations of the unit polarization vectors $\mathbf{s}_{pu}$ and $\mathbf{s}_{pr}$ along the axes X and Y: (X–X), (X–Y), (Y–Y), and (Y–X). The pump frequency $\omega_{pu} = 4.64$ eV is in resonance with the S_2 state.

The GSB signal is shown in in the leftmost column of Figure 3c. The signals in panels (a-1) and (b-1) are dominated by transitions to the states S_2 and S_1 which correspond to $\mathbf{s}_{pr} \parallel$ X and $\mathbf{s}_{pr} \parallel$ Y, respectively. The signals in panels (c-1) and (d-1) are similar to those in panels (b-1) and (a-1), and the minor difference between the two pairs of the signals is caused by slightly different doorway functions. The excitation to the S_2 state can also trigger the excitation of the S_3 state due to the small energy gap between the two states and a relatively large spectral width of the 5 fs pulse.

The SE signals are depicted in the second column of Figure 3. After the interaction with the pump pulse, the wavepacket in the S_2 PE surface exhibits oscillatory motion which is revealed by the SE signal for $\mathbf{s}_{pr} \parallel$ Y, see panels (b-2) and (c-2) in Figure 3c. This SE signal arises from the local excitation of the 2-ring unit. Afterwards, the wavepacket moves towards the S_1/S_2 conical intersection where it undergoes $S_2 \rightarrow S_1$ internal conversion. As a consequence, the oscillatory SE signal ($\mathbf{s}_{pr} \parallel$ Y) becomes weaker and nearly vanishes after 80 fs (see panels (b-2) and (c-2) in Figure 3c). The S_1 state corresponds to the local excitation at the 3-ring unit, the TDM is aligned along the X-axis and its value is quite large. Therefore, vanishing of the SE signal for $\mathbf{s}_{pr} \parallel$ Y goes in parallel with the rise of the SE signal for $\mathbf{s}_{pr} \parallel$ X (see panels (a-2) and (d-2) in Figure 3c). In other words, the excited-state energy transfer from the 2-ring to the 3-ring unit is monitored by the quenching of the SE signal in the Y direction and simultaneous rise of the SE signal in the X direction.

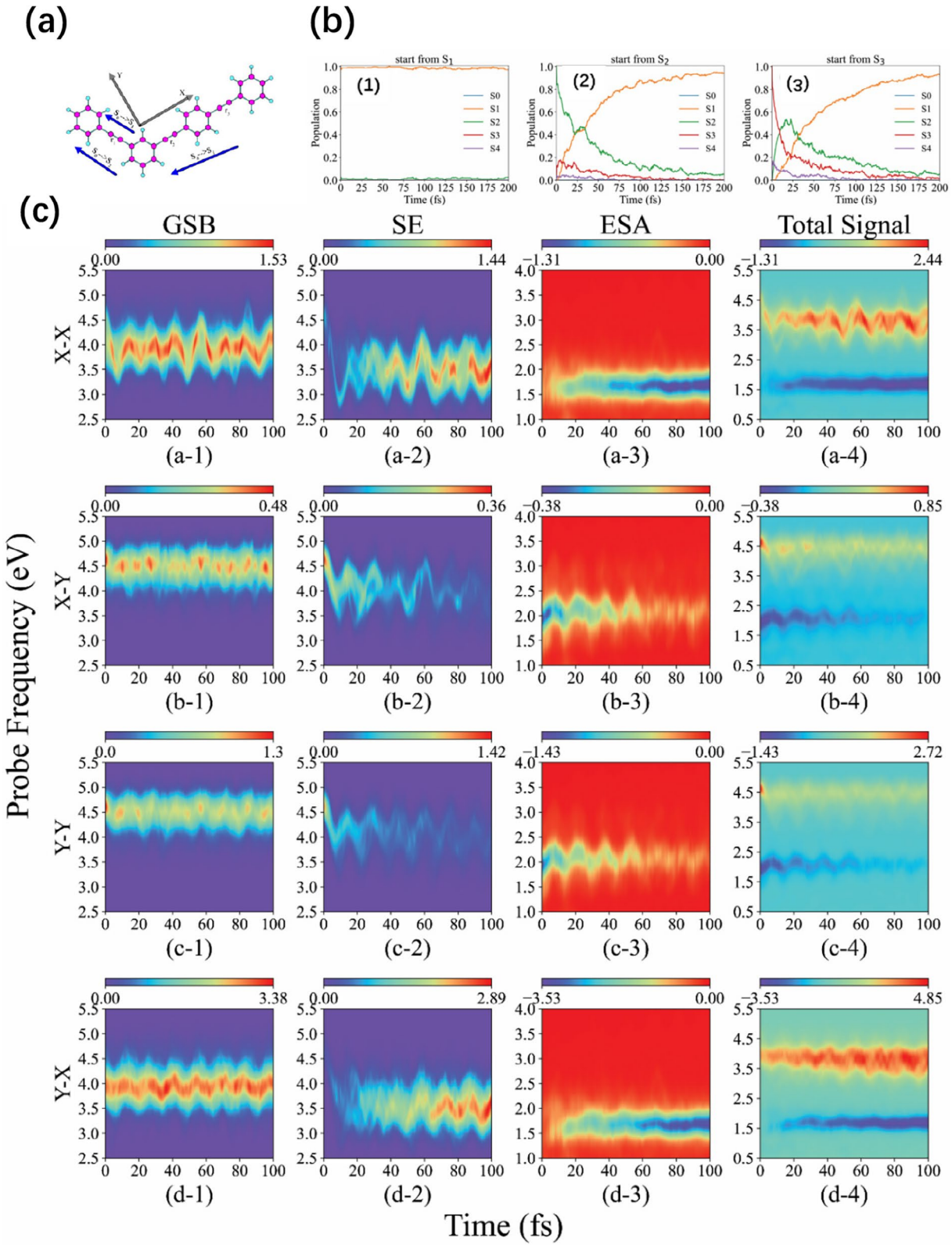

FIGURE 3 | (a) The model dendrimer. (b) Time-dependent electronic populations of the S_0-S_4 states. The dynamics starts from S_1 in (1), S_2 in (2), and S_3 in (3). 200 trajectories were used for each initial state. (c) (1) GSB, (2) SE, and (3) ESA contributions and (4) total integral signal $I^{int}(\omega_{pu}, \omega_{pr}, T)$ as a function of T and ω_{pr}. The notation $\alpha - \beta\,(\alpha, \beta = \mathrm{X}, \mathrm{Y})$ on the left side indicates that the pump pulse polarization $(\mathbf{s}_{pu})$ is along the α-axis direction, while the probe pulse polarization $(\mathbf{s}_{pr})$ is along the β-axis direction. The carrier frequency of the pump pulse is $\omega_{pu} = 4.64$ eV, and the pulse durations are $\tau_{pu} = \tau_{pr} = 5$ fs. Adapted from [207]. Copyright American Chemical Society.

The ESA signal (third column of Figure 3c) is determined by electronic transitions from the S_2 state to those states of manifold {II} which have transition frequencies around 2.0 eV. The ESA signal is qualitatively similar to the SE signal. For instance, the ESA signal also exhibits oscillations revealing wavepacket motion on the S_2 PE surface, albeit the oscillations are less pronounced. The ESA signal for $\mathbf{s}_{pr} \parallel$ Y ($\mathbf{s}_{pr} \parallel$ X) decreases (increases) with the delay time (see the third column in Figure 3c). This also is a signature of the 2-ring to 3-ring excited-state energy transfer. Interestingly, the $\mathbf{s}_{pr} \parallel$ X and $\mathbf{s}_{pr} \parallel$ Y components of the SE and ESA signals appear at different probe wavelengths.

The total TA PP signals are shown in the rightmost column of Figure 3c. The ESA signal is well separated from the GSB and SE signals. Its decline for Y-oriented polarization and rise for X-oriented polarization are signatures of the energy transfer from the 2-ring unit to the 3-ring unit. Thus, polarization-sensitive detection of TA PP signals provides direct evidence of excited-state energy-transfer pathways in dendrimers.

3.2 | UV Pump X-Ray Probe Spectra

While TA PP spectroscopy with UV/vis pump and probe pulses is a well-established and widely applied technique, TA PP spectroscopy with X-ray probe pulses is a relatively new development. It has been enabled by the availability of ultrashort, intense, and energy-tunable soft X-ray pulses, which are provided by third-generation synchrotrons, free-electron laser (FEL) facilities, or table-top high harmonic generation (HHG) instruments [6, 7, 210–212]. The wavelengths of these sources cover the K-shells of the elements carbon, nitrogen, and oxygen. In heteroatomic organic molecules, core excitations from these atoms are site-specific, which adds atomic resolution to the femtosecond time resolution of TA PP spectroscopy [7, 14]. While the pump pulse usually is tuned into resonance with a particular bright valence excited state and therefore is specific for a given chromophore, the broadband X-ray pulses with carrier frequencies near the carbon, nitrogen, or oxygen K-edges are essentially universal spectroscopic probes [7].

In UV pump X-ray probe TA PP spectroscopy, the SE signal is absent and the GSB signal can be experimentally removed by subtraction of the linear ground-state absorption spectrum from the TA PP signal. It is therefore sufficient to evaluate the ESA contribution to the TA PP spectrum. On the other hand, the accurate description of the electronic structure of core-excited states is considerably more challenging than the description of the electronic structure of valence excited states. The pronounced relaxation of the valence electrons upon the generation of core holes results in large shifts of the excitation energies of core-excited states and in a redistribution of the oscillator strength over numerous shake-up electronic states. For stationary (ground-state) X-ray absorption spectra, these problems have been addressed since decades and the standard approximation methods of quantum chemistry have been adapted to cope with the specific challenges of core excited states. The core-valence-separation (CVS) approximation [213–215] decouples the core excited states from the lower-lying valence excited states, enabling variational calculations for core excited states. In the context of spectroscopic applications, single-reference methods based on the polarization propagator, such as the ADC(n) family of methods, or on response functions, such as the response-function coupled-cluster family of methods, are usually the methods of choice, because they provide the dipole transition moments from the ground state to core excited states, see [216] for a detailed review.

The calculation of electronic transition energies and intensities from valence excited states to core excited states involves additional complications [217]. The excitation of a core electron into a hole of the valence shell (a so-called hole-filling transition) results in a final state that is singly excited with respect to the ground-state reference. On the contrary, the excitation of a core electron into an orbital that is unoccupied in the ground-state reference results in a final state that is doubly excited with respect to the ground-state reference. The former excited states are located in the pre-edge region (below the ionization potential of the core electron), while the latter are located in the post-edge region, that is, above the core ionization threshold. Being singly excited with respect to the ground-state reference, the pre-edge states are generally well described by cost-effective single-reference methods such as CC2, EOM-CCSD, or ADC(2). The post-edge doubly excited states, on the other hand, cannot adequately be described with single-reference methods. More sophisticated multi-configuration self-consistent field (MCSCF) methods, complemented with multi-reference configuration interaction (MRCI) or multi-reference perturbation theory (MRPT), are necessary for obtaining reasonably accurate transition energies and intensities [218].

The recent extension of the experimental capabilities and their application to numerous small and medium-sized molecules has stimulated the development of theoretical and computational methods for the simulation of transient XAS spectra, see [219] and [220] for recent reviews. Mukamel and coworkers addressed the detection of the dynamics through conical intersections via the imaging of electronic coherences with non-resonant X-ray Raman scattering processes, the so-called TRUECARS detection scheme [221]. In applications to uracil [222] and thiouracil [223] the TRUECARS signal was evaluated for two-dimensional models of conical intersections. The drawback of such non-resonant X-ray signals employing phase-controlled attosecond and femtosecond X-ray pulses is the very low intensity of the signal. In this review, we are more concerned with the detection of transient electronic populations of valence excited states with resonant X-ray PP spectroscopy. These resonant signals are more intense than non-resonant X-ray scattering signals by orders of magnitude.

Mukamel, Kowalewski, and coworkers calculated the transient X-ray absorption signal in perturbation theory for two-dimensional models of polyatomic molecules, adopting a nonperturbative description of the pump pulse. The imaging of wave-packet dynamics at conical intersections was illustrated for two-dimensional models of pyrrole [224] and thiouracil [225]. Vendrell and coworkers evaluated X-ray scattering and X-ray absorption signals by computing nonlinear response functions with the multi-layer multi-configuration time-dependent Hartree (ML-MCTDH) method for the pyrazine molecule [226–228].

In most applications reported in the recent literature, however, the evaluation of response functions was avoided. The transient spectra were instead approximated by an incoherent summation

of transition intensities from valence excited states to core excited states with different approximations of the excited-state dynamics. Garavelli, Mukamel and coworkers evaluated the valence-to-core transitions at local minima of the valence excited states and along the torsional reaction coordinate for the azobenzene molecule [229]. Hua et al. computed transient X-ray absorption spectra along the minimum-energy reaction path towards conical intersections in uracil [230]. Several groups combined SH or AIMS simulations of the nonadiabatic dynamics in valence excited states with the computation of vertical excitation energies to core-excited states. Wang et al. and Chang et al. simulated UV pump X-ray probe signals with FSSH trajectories for the photodissociation of methyl iodide [231, 232]. List et al. explored the probing of competing relaxation pathways in malonaldehyde for representative trajectories computed with AIMS [233]. Attosecond transient absorption spectra measured at the carbon K-edge of the ethylene cation were simulated with AIMS trajectories by Zinchenko et al. [234] Neville et al. computed vertical X-ray absorption spectra at the centroids of moving Gaussian basis functions determined with the AIMS method for the ethylene molecule [235, 236], while Northey et al. generated the moving Gaussians with the vMCG method to perform simulations of time-resolved XAS spectra of CF_4^+ and pyrazine [237, 238]. Tsuru et al. evaluated time-resolved XAS spectra of pyrazine at the centroids of nonadiabatic quantum wave packets which were computed with the MCTDH method [239]. The durations and shapes of the laser pulses do not enter in these computational protocols which are based on the incoherent summation of electronic transition intensities. They are simulated by an empirical broadening of the spectra in the energy domain.

The quasi-classical DW simulation protocol for TA PP spectra has recently been extended to the X-ray probe regime by Dreuw and coworkers for the example of the pyrazine molecule [241]. The nonadiabatic dynamics in the valence excited states of pyrazine was simulated with on-the-fly LZSH calculations at the ADC(2) level. It is the same simulation as described for the UV pump UV probe spectra of pyrazine above. The transition energies and transition moments from the valence excited states to the C1s and N1s core excited states were computed in the CVS approximation with the extended ADC(2) method (ADC(2)-x). The ADC(2)-x scheme includes the first-order matrix elements in the two-hole two-particle block and thus provides a more accurate description of the amplitudes of doubly excited states, which yields improved excitation energies of core excited states [216]. Thanks to the high accuracy of the CVS approximation, the state vectors obtained by the two separate ADC(2) calculations for valence and core excited states are nearly orthogonal, which simplifies the computation of the TDMs. As previously suggested by Tsuru et al. [239], it is insightful to consider the vertical absorption spectra at the local minima of the $^1B_{2u}$, $^1B_{3u}$ and ^1A_u valence excited states of pyrazine for the interpretation of the vibrational signatures of the PP spectra at the C1s and N1s edges, see Figure 4. At the C1s edge (left in Figure 4), the absorption from all three valence excited states gives rise to a pre-edge double peak with rather similar excitation energy. At the N1s edge, on the contrary, a single pre-edge absorption peak is observed and the excitation energies from the $^1B_{3u}$ and ^1A_u states differ by 1.5 eV. It is also noteworthy that the intensities of the $^1B_{3u}$ and ^1A_u states relative to the intensity of the $^1B_{2u}$ state are much higher at the N1s edge than at the C1s edge. Because the excitation energies of the post-edge states (shown as dashed lines in Figure 4) are not accurate at the ADC(2) level, the simulation of the transient X-ray absorption spectra was restricted to the pre-edge region.

The UV pump X-ray probe spectra of pyrazine, simulated with the classical DW protocol, assuming 5 fs pump and probe pulses, are displayed in Figure 5. The intense signal extending from $T = 0$ to $T \approx 20$ fs monitors the population of the bright $^1B_{2u}$ state. The blue-shift of the X-ray absorption signal reflects the wave-packet motion towards the minimum of the $^1B_{2u}$ surface (analogous to the red-shift of the UV probe signal in Figure 1). Beyond about 20 fs,

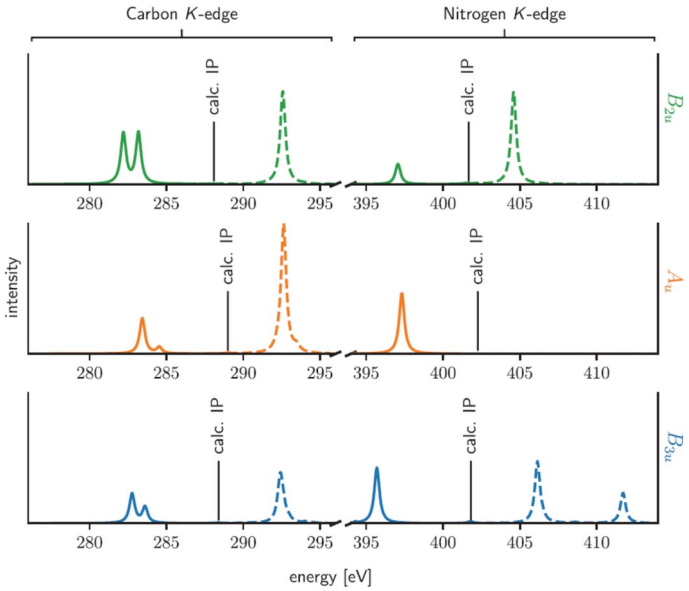

FIGURE 4 | ADC(2)/CVS-ADC(2)-x carbon and nitrogen K-edge ESA spectra for the B_{2u}, A_u, and B_{3u} valence-excited states of the pyrazine molecule. Spectra were computed at the minimum energy geometries of the respective electronic states. A Lorentzian broadening with a full width at half-maximum (FWHM) of 0.4 eV was applied. Ionization potentials were calculated with CVS-ADC(2)-x by placing very diffuse basis functions on all atoms [240]. The spectra of pre-edge states are shown as full lines, and the spectra of above-edge states as dashed lines. Adapted from [241]. Copyright American Chemical Society.

most of the excited electronic population resides in the $^1B_{3u}$ and ^1A_u states. When probed at the C1s edge, the absorption intensities from these $^1n\pi^*$ states are comparatively low (see Figure 5), resulting in a weak absorption signal. Moreover, the transition energies from these two states are similar (Figure 4), which leads to a relatively structureless signal in the frequency domain. At the N1s edge, on the contrary, the absorption intensities of the two $^1n\pi^*$ states are higher than the intensity of the $^1B_{2u}$ state and the transition energies at the respective minima are clearly separated, which results in a structured transient X-ray absorption signal. The high-energy peaks in the N1s signal at about 65 and 135 fs in Figure 5 can be assigned to the ^1A_u state, while the low-energy peak at about 80 fs can be assigned to the $^1B_{3u}$ state by comparison with Figure 4 [241]. The higher contrast of the imaging of the nonadiabatic dynamics at the N1s edge can be understood by inspection of the n, π and π^* orbitals of pyrazine [239, 241].

A transient X-ray absorption spectrum of pyrazine pumped via the $^1B_{2u}$ state and probed at the C1s edge has been recorded by Scutelnic et al. with an overall time resolution of 200 fs [242]. This resolution is not sufficient for resolving the sub-100 fs dynamics of the valence excited states of pyrazine. On the other hand, most of the experimentally observed signal is located in the post-edge region which could not be covered with the present electronic-structure methodology. The quantitative simulation of the complete transient X-ray absorption spectra of pyrazine at the C1s and N1s edges remains an open challenge.

4 | Two-Dimensional Electronic Spectra

The development of two-dimensional (2D) electronic spectroscopy was stimulated by earlier developments in nuclear magnetic resonance (NMR) spectroscopy [10, 243, 244]. In 2D spectroscopy, the pump pulse of TA PP spectroscopy is replaced by a pair of phase-coherent excitation pulses. The first pulse establishes a coherence between the electronic ground state and the bright excited electronic state. The second pulse, which is delayed by the so-called coherence time τ, converts the coherence into populations of the ground state and the excited state. After the so-called waiting time T, the probe pulse again generates a coherence which emits the signal field. The signal field is detected interferometrically by superposition with a known reference field, the so-called local oscillator, see Equation (2). Fourier transform of the signal with respect to τ and τ_t yields the two-dimensional spectrum

$$I_\alpha^{2D}(\omega_\tau, T, \omega_t) = \int d\tau d\tau_t e^{i(\xi_\alpha \omega_\tau \tau + \omega_t \tau_t)} I_\alpha(\tau, T, \tau_t) \qquad (31)$$

$$= \mathrm{Re} \sum_{k=0,\mathrm{I},\mathrm{II}} a_k \left\langle W_k(\mathbf{R}(T), \mathbf{P}(T); \omega_t) D_\alpha(\mathbf{R}_g, \mathbf{P}_g; \omega_\tau) \right\rangle_{\mathrm{MC}}$$

as a function of the waiting time T, where $\alpha = \mathrm{R},\ \mathrm{NR}$ (see Equation (1)).

By monitoring the correlation of two transition frequencies and their evolution with the waiting time, 2D spectroscopy provides dynamical information that is not exposed by one-dimensional PP spectroscopies [11, 12, 245, 246]. 2D spectroscopy in the visible regime has become the main tool for the exploration of exciton dynamics and energy transfer processes in multi-chromophoric systems, such as J and H aggregates [247–249] and biological antenna complexes [250–253]. The detection of unexpectedly long-lived coherences in antenna complexes at room temperature and their assignment to either inter-chromophore electronic coherence or intra-chromophore vibrational dynamics has been

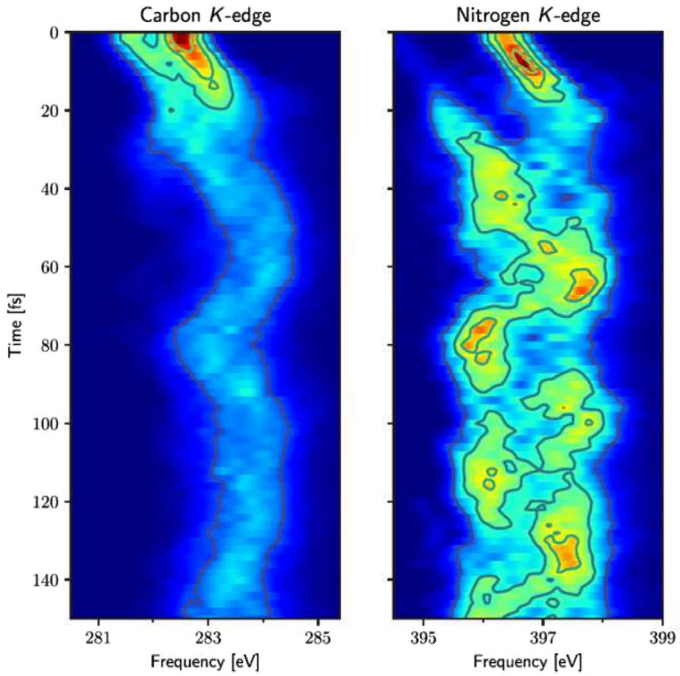

FIGURE 5 | Simulated time-resolved x-ray absorption spectrum at the (a) carbon and (b) nitrogen K edges for 5 fs pump and probe pulses. Adapted from [241]. Copyright American Chemical Society.

hotly disputed in the literature [254–256]. Recently, electronic 2D spectroscopy has been further developed by the detection of the signal via fluorescence [32, 257] and by applying laser pulses in the non-perturbative regime, resulting in an improved signal-to-noise ratio [29]. It was shown that clean n-th order multi-pulse signals can be experimentally extracted with a novel intensity-cycling scheme [258].

The theory of electronic 2D spectroscopy correspondingly was mainly developed in application to multi-chromophoric systems that are modeled by the Frenkel exciton Hamiltonian, including exciton-vibration coupling [115, 248]. For small model systems (dimers, trimers, etc.), a quantum mechanical description of the vibronic dynamics is possible. For example, Sun et al. applied the Davydov ansatz for the calculation of the dynamics and 2D spectra of J-aggregates [259]. Maly et al. developed a multi-level Redfield model to capture the role of resonant high-frequency vibrations in excitonically coupled two-level systems [260]. Yao et al. computed nonlinear response functions for 2D spectra for vibronically coupled exciton systems using the time-dependent density matrix renormalization group (DMRG) method [261]. The DMRG method also was applied by Jiang et al. to calculate spectra for finite-temperature molecular aggregates [262].

For larger excitonic systems, the vibrations usually are modeled as a heat bath. The hierarchical equation-of-motion (HEOM) formalism [263, 264] has been widely employed to obtain numerically exact results for the exciton dynamics and calculate spectra. Semi-classical methods based on the Meyer-Miller-Stock-Thoss mapping Hamiltonian [101, 102] have been applied for the simulation of 2D spectra of dissipative exciton systems, partly in comparison to the numerically exact HEOM results. Provazza et al. performed trajectory-based semi-classical path-integral calculations of 2D response functions for non-Markovian exciton dynamics [265]. Polley and Loring extended the semi-classical mapping Hamiltonian approach to multiple interacting electronic states [266]. The quasi-classical Ehrenfest and SH methods also were used for the simulation of 2D spectra of exciton systems. Van der Vegte et al. calculated 2D spectra for an excitonically coupled vibronic dimer and benchmarked the Ehrenfest results against numerically exact HEOM results [267]. Tempelaar et al. applied the SH method to simulate the dynamics of a vibronic dimer and to calculate 2D spectra [268]. Jain et al. proposed a simplified procedure for the calculation of 2D spectra from SH trajectories by restricting the simulations to the waiting time [269]. In a pioneering application, nonadiabatic excited-state dynamics was taken into account with ab initio SH simulations of 2D spectra at the CASSCF level by Richter and Fingerhut for the diphenylmethane molecule [270].

In general, the third-order dipole response functions of the 2D signal were computed in these studies; that is, the effects of finite duration of the laser pulses were neglected. Using the equation-of-motion phase-matching approach (EOM-PMA) [138], Shi and coworkers and Tan and coworkers demonstrated the effects of the inclusion of finite pulse durations, with application to 2D spectra of the light-harvesting complex II [271–273]. Alternatively, Gao and Geva [274] applied the nonperturbative equation-of-motion methodology [24] to include finite pulse durations; see also [275] for a review.

Experimentally, 2D spectroscopy was extended into the deep UV by several groups [12, 276–280]. This technical development enabled the application of 2D spectroscopy to smaller polyatomic molecules, such as, for example, cyclohexadiene, azulene, or pyrene, and in particular to organic molecules of biological interest, such as DNA bases [281–283]. While electronic 2D spectroscopy holds great potential for uncovering the pathways of radiationless electronic decay dynamics in polyatomic molecules [278, 284] as well as photochemical reaction mechanisms [285, 286], the spectral window of 2D spectroscopy is determined by the bandwidths of the laser pulses, which currently are rather limited. For the theoretical prediction of signals that can meaningfully be compared with experimental data, it is essential to include explicitly the durations and shapes of the laser pulses in the simulation.

Garavelli, Mukamel, and coworkers developed and extensively applied an ab initio protocol to simulate 2D signals for molecular chromophores [114, 287]. The calculation of electronic transition energies and dipole transition moments with MCSCF and MRPT methods at optimized ground-state and excited-state equilibrium geometries was combined with Brownian oscillator line shape functions and QM/MM simulations of environmental effects. Since excited-state dynamics were not explicitly treated, the calculations were restricted to zero waiting time or picosecond waiting times when the excited-state relaxation dynamics were completed [288, 289]. The ab initio protocol was applied to simulate linear and 2D electronic spectra of pyrene [290]. This strategy was also applied to the probing of intermediate species along photochemical reaction pathways of derivatives of benzene as well as of DNA nucleobases by 2D spectroscopy [291–293]. In an alternative approach, Begusic and Vanicek implemented Heller's semi-classical thawed Gaussian approximation [90] with ab initio on-the-fly electronic-structure calculations to compute 2D spectra for phenol and azulene [94]. Due to the local harmonic approximation, this approach is limited to dynamics on single adiabatic excited-state PE surfaces but could be extended to multiple-surface problems by using an expansion in a basis set of frozen Gaussians. The inclusion of finite-temperature effects in the framework of ab initio thermofield dynamics was demonstrated by Begusic and Vanicek for azulene [294].

Assuming for simplicity that the carrier frequencies, shapes, and polarizations of the pulse pairs 1, 2 and 3, 4 are identical (see Equations (5), (6), (27)), neglecting the nonadiabatic couplings $H_{0,\mathrm{I}}$ and $H_{\mathrm{I,II}}$ on the timescale of interest, and expressing the pulse envelopes through their back Fourier transforms according to Equation (28), we obtain the following explicit DW expressions for the on-the-fly evaluation of 2D signals: [160, 161].

$$D_\alpha\left(\mathbf{R}_g,\mathbf{P}_g;\omega_\tau\right)=\rho_g^{Wig}\left(\mathbf{R}_g,\mathbf{P}_g\right)\frac{E_1^2\left(\omega_\tau-\omega_p\right)\left(\mathbf{s}_{pu}\cdot\boldsymbol{\mu}_{ge}\left(\mathbf{R}_g\right)\right)^2}{\nu+i\xi_\alpha\left(U_{eg}\left(\mathbf{R}_g\right)-\omega_\tau\right)}, \tag{32}$$

is the doorway function, and

$$W_0\left(\mathbf{R}_g(T),\mathbf{P}_g(T);\omega_t\right)=\sum_{e'}\frac{E_4^2\left(\omega_t-\omega_p\right)\left(\mathbf{s}_{pr}\cdot\boldsymbol{\mu}_{ge'}\left(\mathbf{R}_g(T)\right)\right)^2}{\nu+i\left(U_{e'g}\left(\mathbf{R}_g(T)\right)-\omega_t\right)}, \tag{33}$$

$$W_{\mathrm{I}}\left(\omega_t, \mathbf{R}_e(T), \mathbf{P}_e(T); \omega_t\right) = \frac{E_4^2\left(\omega_t - \omega_p\right)\left(\mathbf{s}_{pr} \cdot \boldsymbol{\mu}_{ge(T)}\left(\mathbf{R}_e(T)\right)\right)^2}{\nu + i\left(U_{e(T)g}\left(\mathbf{R}_e(T)\right) - \omega_t\right)}, \tag{34}$$

$$W_{\mathrm{II}}\left(\mathbf{R}_e(T), \mathbf{P}_e(T); \omega_t\right) = \sum_f \frac{E_4^2\left(\omega_t - \omega_p\right)\left(\mathbf{s}_{pr} \cdot \boldsymbol{\mu}_{fe(T)}\left(\mathbf{R}_e(T)\right)\right)^2}{\nu + i\left(U_{fe(T)}\left(\mathbf{R}_e(T)\right) - \omega_t\right)} \tag{35}$$

are the window functions. Recall that the angular brackets in Equation (31) denote Monte Carlo sampling of the initial nuclear coordinates and momenta $\mathbf{R}_g$, $\mathbf{P}_g$, summation over the states e of manifold {I}, as well as a sampling of the hopping probabilities in the evaluation of W_{I} and W_{II}.

The classical doorway and window functions of 2D spectroscopy differ from the corresponding functions of the integral TA PP signal in two respects. First, they depend on the dephasing rates of the electronic transitions, which are approximated by a single average dephasing rate ν in Equations (32–35). They reflect the fact that the material system is in coherence during the coherence time τ and the detection time $_\tau$. Second, the doorway and window functions of 2D spectroscopy are complex-valued rather than positive definite, which may affect the convergence of the Monte Carlo sampling of the trajectories.

In deriving Equations (32–35), it was assumed that $E_1(\omega) = E_2(\omega)$ and $E_3(\omega) = E_4(\omega)$. This assumption can be relaxed and all four pulses can be different, if desired. If 2D signals are detected with a spectrometer (i.e., without heterodyning by pulse number 4), then $E_4^2\left(\omega_t - \omega_4\right)$ should be replaced by $E_4\left(\omega_t - \omega_4\right)$ in Equations (33–35). The 2D spectrum in the impulsive limit ($E_j(t) \to \delta(t)$) is recovered by setting $E_j(\omega) \to 1$.

The expressions of Equations (31–35) for the 2D signal were evaluated for the pyrazine molecule. For the evaluation of the SE signal, a sample of 1000 nonadiabatic excited-state trajectories was computed with the LZSH algorithm and the ADC(2) electronic-structure method up to 200 fs [160]. To compute the GSB signal, 300 trajectories were stochastically sampled from the ground-state Wigner distribution and propagated on the PE surface of the electronic ground state up to 200 fs. To compute the ESA signal, the excitation energies from the states of manifold {I} to the 30 lowest states of manifold {II} and the corresponding transition moments were computed for 200 randomly selected trajectories of manifold {I}. Gaussian pulse envelopes with a pulse duration of 0.1 fs were chosen to ensure a spectral window which covers the energy range of the $^1B_{2u}$, $^1B_{3u}$ and ^1A_u electronic states of pyrazine. The dephasing parameter is chosen as 0.1 eV, corresponding to a dephasing time constant of 6.6 fs. This is to be understood as a compromise between the dephasing time of the $S_0 - ^1B_{2u}$ transition of about 30 fs [187, 295] and the dephasing times of the ESA transitions, which are expected to be shorter than 10 fs.

The calculated non-rephasing 2D signals of pyrazine for four representative waiting times, $T = 0$, 20, 35, and 60 fs, are displayed in Figure 6. The corresponding rephasing signals are similar, differing just in the peak shapes. The peak shapes of the present simulation carry little relevant information due to the crude approximation of the propagation during the coherence and detection times in the present version of the classical DW approximation. The relevant information is in the positions of the peaks in ω_τ, ω_t space and in the evolution of the peak intensities with the waiting time T. For better visibility, the signals in Figure 6 were scaled to equal intensity within each row. The signals without re-scaling of the peak intensities can be found in the Supporting Information of [161].

All peaks in Figure 6 are located at $\omega_\tau \approx 5.0$ eV, which corresponds to the vertical excitation energy of the $^1B_{2u}$ state of pyrazine. Peaks with $\omega_t \neq \omega_\tau$ are so-called cross peaks which carry information on dynamical processes in the excited-state manifold. The GSB signal in the first row of Figure 6 is essentially independent of T and carries no dynamical information. The intensity of the SE signal in the second row of Figure 6 decays on a time scale of about 20 fs as discussed above for the TA PP signals with UV and X-ray probing (Figures 1 and 5). This effect is suppressed in Figure 6 by the re-scaling of the intensities. The SE peak at $T = 20$ fs is significantly red shifted due to the motion of the wave packet towards the minimum of the $^1B_{2u}$ PE surface. The cross peaks at $T = 35$ fs and $T = 60$ fs reflect the transfer of population to the $^1B_{3u}$ and ^1A_u states, respectively. These nominally dark states become visible in emission due to intensity borrowing from the bright $^1B_{2u}$ state.

The ESA signal in the third row of Figure 6 is considerably more intense than the SE signal. It features distinct peaks which cover a range of about 4.0 eV in ω_t with dynamically varying intensities as function of the waiting time. The comparison of the 2D ESA signal with the ESA signal of UV TA PP spectroscopy (Figure 1) reveals the enhanced information content of the 2D ESA signal. In this relatively simple molecule of high symmetry, the individual peaks of the ESA signal can be assigned to specific electronic transitions from manifold {I} to manifold {II}. As discussed in detail in [161], the peaks can be assigned to either "particle-type" transitions, in which the electron residing in the lowest unoccupied molecular orbital (LUMO) of the electronic ground state is excited to higher π^* orbitals, or "hole-type" transitions, in which the hole in the $6a_g(n)$ orbital is filled by transitions from lower occupied orbitals. Broadly, the ESA peaks at T = 35 fs are dominated by excitations from the $^1B_{3u}$ state, while the ESA peaks at $T = 60$ fs represent excitations from the ^1A_u state. Like the UV pump X-ray probe PP signal (Figure 5), the UV 2D spectrum of pyrazine exhibits fingerprints of the transient population of the ^1A_u state.

The total 2D signal is displayed in the fourth row of Figure 6. It is dominated by the GSB and ESA contributions. The few snapshots in the waiting time in Figure 6 do not capture the rich dynamics reflected in the 2D spectrum of pyrazine. A movie showing the ESA signal in time steps of 1 fs up to 200 fs is available in the Supporting Information of [161].

5 | Femtosecond Time-Resolved Photoelectron Spectra

In femtosecond time-resolved photoelectron spectroscopy (TRPES), a femtosecond visible or UV pump pulse excites a molecule to one or several valence excited states. A time-delayed femtosecond probe pulse ionizes the photoexcited molecule, and the

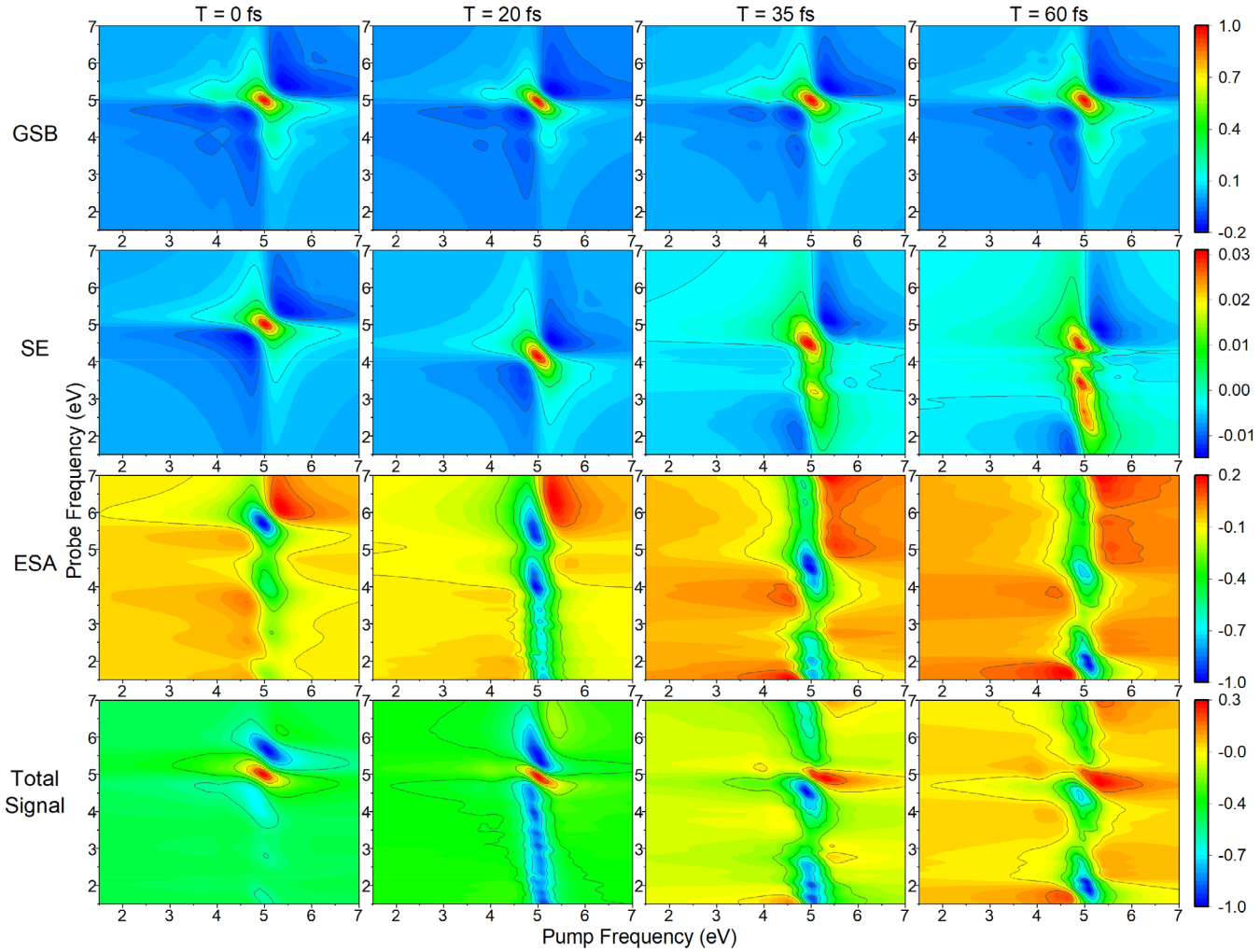

FIGURE 6 | Non-rephasing 2D spectra of pyrazine at waiting times $T = 0$, 20, 35, and 60 fs. For better visibility, each of the GSB, SE, ESA, and total signals (from top to bottom) is rescaled to cover the same intensity range for different T. Adapted from [161]. Copyright American Chemical Society.

energy spectrum of the photoejected electrons is recorded as a function of the delay time of the pulses. By the Franck-Condon principle, the time-resolved energy distribution of the photoelectrons carries information on the excited-state dynamics of the molecule. The theory of TRPES was developed, and theoretical simulations of TRPE signals were performed [33, 34] before the first experimental realizations of the technique were reported [15, 296]. These early formulations of the theory were based on a quantum wave-packet description of the nuclear motion and a discretization of the electron continua [33, 34, 36, 297]. The interaction of the molecule with the laser fields was described either perturbatively [34] or non-perturbatively [33, 36, 297]. The formal theory of time-resolved photoelectron angular distributions was worked out by Seideman and coworkers [35, 298, 299]. Takatsuka, McKoy, and coworkers developed a more elaborate description in which the dependence of the photoionization matrix elements on energy and nuclear geometry is taken into account by first-principles electron scattering calculations [37, 300, 301].

Experimentally, the mapping of vibrational wave-packet dynamics with TRPES was first demonstrated by Baumert and coworkers for ionization of Na_2 [15] and by Neumark and coworkers for electron photodetachment from I_2^- [296]. Stolow and coworkers first demonstrated the versatility of TRPES for the unraveling of radiationless decay processes in a linear polyene [16], while Hertel and coworkers demonstrated the insights which can be obtained with this uniquely sensitive technique for molecular clusters [17]. Meanwhile, a number of excellent reviews of TRPES and its applications have been published, see, for example [5, 19–21, 302–304].

The first theoretical descriptions of femtosecond TRPES based on a classical treatment of the nuclear motion were developed by Stock and coworkers [152] and Meier and Engel [305] for a reduced-dimensional model of pyrazine and for a diatomic molecule, respectively. A semi-classical simulation using the semi-classical forward-backward initial-value representation was performed by Miller and coworkers for the photodetachment of I_2^- [306]. Employing the classical path approximation [66] and the classical time-dependent Franck-Condon principle [162], Meyer and Engel derived a computational recipe which is equivalent to the classical DW approximation for the TRPE signal to be discussed below [305]. In an independent development, Mitrić, Bonačić-Koutecký and coworkers developed the classical

theory of TRPES for non-Born-Oppenheimer dynamics in polyatomic molecules. In the original formulation, the dependence of the photoionization matrix elements on energy and nuclear geometry was neglected [307, 308]. In subsequent work, Stieltjes imaging was employed to compute energy-dependent TDMs in the continuum [309]. In addition to the perturbative approach (in the radiation-matter interaction), SH simulations including the laser fields in a non-perturbative manner (field-induced SH) were performed [310]. Approximating the electron continuum wave functions by Coulomb waves, a scheme for the calculation of photoelectron angular distributions was developed [311] and applied to the pyrazine molecule within the TDDFT electronic-structure model [312].

Martinez and coworkers developed a combination of the Fermi Golden Rule (FGR) description of the ionization process with time-dependent AIMS simulations [60] of the excited-state dynamics [313]. The TRPE signal is approximated as an incoherent sum of ionization probabilities from neutral excited states to the electronic states of the cation. This computationally efficient recipe requires that the ionization process is much faster than the nonadiabatic excited-state dynamics. A formal derivation of this approximation from a more general theory has been given by Mukamel and coworkers [314]. The methodology was applied to simulate several TRPE signals of polyatomic molecules with the AIMS method [315–318]. The FGR approximation also was applied in combination with classical SH simulations of the excited-state dynamics by Mukamel and coworkers [319], Gonzalez and coworkers [320] and Matsika and coworkers [321, 322]. In a conceptually similar approach, Barbatti and coworkers applied the nuclear ensemble method [65] to compute time-resolved photoelectron spectra from SH simulations [323]. The disadvantage of these ad hoc "snapshot" descriptions of the ionization process is that they do not take the shapes and durations of the laser pulses into account. The latter have to be introduced in an empirical manner by convolutions of the signals with Gaussian functions in frequency and/or time. The idea of combining the DW approximation with on-the-fly trajectory simulations for the simulation of photoelectron spectra was first suggested by Bonačić-Koutecký and Mitrić [324] and Rahav and Mukamel [325].

In TRPES, the molecules are excited to a state e of manifold {I} with a pump pulse and subsequently photoionized to the electron continua of cationic states. The molecular and system-field interaction Hamiltonians governing these processes are presented in Appendix A. The pump process in TRPES is the same as in TA PP spectroscopy, see Section 3.1. The trajectories are initialized by sampling from the classical doorway distribution of Equation (23)

$$D(\omega_{pu},\mathbf{R}_g,\mathbf{P}_g)=E_{pu}^2\left(\omega_{pu}-\Delta E_{eg}(\mathbf{R}_g)\right)\left(\mathbf{s}_{pu}\cdot\boldsymbol{\mu}_{ge}(\mathbf{R}_g)\right)^2\rho_g^{Wig}(\mathbf{R}_g,\mathbf{P}_g) \tag{36}$$

where $\Delta E_{eg}(\mathbf{R})=E_e(\mathbf{R})-E_g(\mathbf{R})$ is the vertical excitation energy from the ground state g to the excited state e, $\boldsymbol{\mu}_{ge}(\mathbf{R})$ are the TDMs from the ground state g to the excited states e in manifold {I}, and $\rho_g^{Wig}(\mathbf{R},\mathbf{P})$ is the ground-state Wigner distribution function [163]. The trajectories are propagated in the vibronically coupled excited states of manifold I with a SH algorithm as described in Section 3.1.

The classical window function for TRPES is the same as the window function for the ESA component of the TA PP signal (Equation 26), except that the final electronic states are continuum states rather than bound states. The discrete set of TDMs $\boldsymbol{\mu}_{ef}$ is replaced by a continuous distribution of electronic TDMs, $\boldsymbol{\mu}_{e,E_k,\theta,\phi}$, where E_k denotes the energy of the photoelectron and θ and ϕ denote the polar and azimuthal angles of the $\boldsymbol{k}$-vector of the electron (see Appendix A). The continuum states are scattering wave functions of the electron in the field of the molecular cation with appropriate boundary conditions [300]. The quasi-classical window function for the energy and angle resolved TRPE signal thus reads

$$W_{\mathrm{PE}}(\omega_{pr},\mathbf{R}_e(T),\mathbf{P}_e(T),E_k(T),\theta,\phi)= \tag{37}$$

$$\sum_f\left(E_{pr}\left(\omega_{pr}-E_k(T)-IP_{ef}(\mathbf{R}_e(T))\right)\right)^2\left(\mathbf{s}_{pr}\cdot\boldsymbol{\mu}_{ef,E_k,\theta,\phi}(\mathbf{R}_e(T))\right)^2.$$

Here $IP_{ef}(\mathbf{R}_e(T))$ denotes the vertical ionization energy of an electron from the excited state e to the electronic state f of the molecular cation at the nuclear geometry $\mathbf{R}_e(T)$. The simplicity of Equation (37) should be noted: the contribution of final state f to the window function is given by the product of the power spectrum of the probe pulse with the square of the TDM distribution of the continuum. The energy and angle resolved TRPE signal

$$\begin{aligned}&I_{\mathrm{PE}}(\omega_{pu},\omega_{pr},T,E_k,\theta,\phi)=\\&\left\langle W_{\mathrm{PE}}(\omega_{pr},\mathbf{R}_e(T),\mathbf{P}_e(T),E_k(T),\theta,\phi)D(\omega_{pu},\mathbf{R}_g,\mathbf{P}_g)\right\rangle_{\mathrm{MC}}\end{aligned} \tag{38}$$

is obtained by Monte Carlo sampling of the initial conditions and the SH events. The sampling includes the Monte Carlo integration over the states e of manifold {I} weighted by their oscillator strengths. The energy resolved integral signal $I_{\mathrm{PE}}(\omega_{pu},\omega_{pr},T,E_k)$ is obtained by integration of the differential signal (Equation (38)) over the solid angle of the photoelectron. Additional integration over the photoelectron energy and summation over the ionization channels f yields the total ion signal $I_{\mathrm{ion}}(\omega_{pu},\omega_{pr},T)$.

The theory of the electron angular distribution of resonant two-photon ionization signals has been worked out by Dixit and McKoy and Zare and coworkers in the CW limit [326, 327]. The formal theory was extended to TRPES by Seideman [35, 299] and McKoy and coworkers [300] within a quantum wave-packet formulation of the excited-state dynamics. Since the description of the electron continuum is the same in quantum and quasi-classical formulations of the nuclear dynamics, these results apply also to the latter. In the most general case of arbitrary polarization vectors $\mathbf{s}_{pu},\mathbf{s}_{pr}$, the photoelectron angular distribution in the laboratory frame is neither cylindrically symmetric nor is it symmetric with respect to $\theta=\pi$. For parallel polarization vectors, the angular distribution simplifies to [35].

$$I_{\mathrm{PE}}(\theta,\phi)=\sum_L A_L P_L(\cos\theta) \tag{39}$$

where the P_L are Legendre polynomials of degree L. The angular distribution (Equation 39) differs from the standard photoelectron angular distribution specified by the asymmetry parameter β [328].

$$I_{\mathrm{PE}}(\theta,\phi) = A\big(1+\beta P_2(\cos\theta)\big) \tag{40}$$

because the pump pulse generates an aligned distribution of excited molecules.

While the formal expression for the window function of the TRPE signal (Equation 37) is completely analogous to the expression for the window function of the TAP PP signal (Equation 26), the physics of these signals is fundamentally different. In the case of the polarization-detected integral TAP PP signal, the probe process is completed by the end of the probe pulse; that is, on femtosecond time scales. In TRPES, on the contrary, the photoelectron is detected asymptotically on time scales that are much longer than the pump-probe delay time. Before the electron hits the detector, the electron and the molecular cation are entangled, and the electron carries the full information on the coupling of cationic channels (such as fragmentation into neutrals via dissociative superexcited bound states) as well as on the dynamics within the cation (such as internal conversion between electronic states) until the detection time. Accurate first-principles calculations of TRPE signals, therefore, are extremely challenging.

For a given photon energy E and at large distances r of the photoelectron, the continuum wave function asymptotically approaches a linear combination of products of cationic states and single-particle continuum functions

$$\Phi^{(-)}_{E\alpha}(\boldsymbol{r},\boldsymbol{R}) \overrightarrow{r\to\infty} \sum_{f'} \Psi_{f'}(\boldsymbol{r},\boldsymbol{R})\phi^{(-)}_{f'E\alpha}(\boldsymbol{r},\boldsymbol{R}) \tag{41}$$

where the summation runs over all states accessible at a given photon energy (open channels), α serves as a collective index for the quantum numbers needed to uniquely specify the solution and the superscript $(-)$ denotes incoming wave boundary conditions [329]. In contemporary applications, the continuum wave functions have been calculated for uncoupled electronic channels as antisymmetrized products

$$\Phi^{(-)}_{f\mathbf{k}_f}(\mathbf{r},\mathbf{R}) = \mathcal{A}\Big(\Psi_f(\mathbf{r},\mathbf{R})\phi^{(-)}_{f\mathbf{k}_f}(\mathbf{r},\mathbf{R})\Big) \tag{42}$$

where $\Psi_f(\mathbf{r},\mathbf{R})$ is the wavefunction of the final ionic state and $\phi^{(-)}_{fk_f}(\mathbf{r},\mathbf{R})$ is the wavefunction of the free electron.

In TRPES, highly correlated wavefunction methods are required to accurately describe the bound states of the electronically excited N-electron neutral molecule Ψ_e and the $(N-1)$-electron cationic states Ψ_f. Within the single-channel approximation (Equation (42)), the calculation of the TDM matrix elements for the $e\to f$ ionization channel

$$\boldsymbol{\mu}_{ef\mathbf{k}_f} = \left\langle \Psi_e \middle| \boldsymbol{\mu} \middle| \Phi^{(-)}_{f\mathbf{k}_f} \right\rangle \tag{43}$$

can be reduced to one-particle matrix elements $\left\langle \phi^{(-)}_{f\mathbf{k}_f} \middle| \mu \middle| \phi^D \right\rangle$ by expressing the dipole moment $\boldsymbol{\mu}$ as a sum of single particle operators and defining the Dyson orbital $|\,\phi^D\rangle$

$$|\,\phi^D\rangle = \sum_j \chi_{fj}\phi_j \tag{44}$$

where the amplitudes χ_{fj} are given as

$$\chi_{\mathrm{fj}} = \langle \Psi_f \,|\, \hat{a}_j \,|\, \Psi_e \rangle \tag{45}$$

and $\hat{a}_j$ is the annihilation operator acting on the molecular orbital ϕ_j of the neutral molecule. The Dyson orbital represents the effective orbital from which the electron is emitted. In the frozen-core Hartree-Fock approximation, it is simply the molecular orbital from which the electron is ejected. Algorithms for evaluating of the overlap integral (Equation 45) for correlated wave functions have been implemented for TDDFT [311, 312], CASSCF [313, 320, 330], ADC(2) [331], coupled-cluster (CC) [332–335], and extended multistate (XMS) complete active space second-order perturbation theory (CASPT2) [336]. Details of the calculation of Dyson orbitals at the XMS-CASPT2 level are provided in Appendix F, while readers are referred to the original publications for other methods.

When the kinetic energy of the ejected electron is sufficiently high, the photoelectron and the cation become effectively decoupled. The intensity of a transition is then approximated as the square of the matrix element of the electric dipole operator taken with the Dyson orbital and the one-electron continuum wave function. The ionization process is thus modeled as a one-electron event. These continuum orbitals, representing the scattering states of an electron in the field of the cationic channel f, require solving coupled differential equations with appropriate boundary conditions.37 [300, 301, 337, 338], Accurate continuum states can be obtained using the Schwinger variational principle [339], R-matrix theory [328, 340], or the Galerkin method [341, 342]. These approaches are implemented in several recently developed computational codes [343–345], but they have been rarely employed in the simulation of TRPES experiments.

Since a TRPE spectrum is typically recorded over a time window of several hundred femtoseconds, accurately simulating such spectra with reasonable intervals of 2–3 femtoseconds would require thousands of evaluations of photoionization matrix elements. Due to this high computational cost, more approximate methods, such as orthogonalized Coulomb waves or even free-particle plane waves, are often used as continuum orbitals in TRPES simulations of polyatomic organic molecules [311, 312, 316, 332–334, 346]. Decleva and co-workers assessed the quality of approximate methods for treating continuum states by comparing them against accurate continuum one-particle wave functions computed in a multicenter B-spline basis at the density functional theory (DFT) level (see Appendix F) [331]. For the example of furan, they showed that the results obtained with approximate methods (e.g. orthogonalized Coulomb waves) may be qualitatively different from those obtained with accurate continuum wave functions.

As the first application of the quasi-classical DW formalism to TRPES, we consider again the pyrazine molecule. Femtosecond time-resolved imaging of the nonadiabatic excited-state dynamics of pyrazine was pursued by Suzuki and coworkers for more than 25 years with ever improving time resolution and signal-to-noise ratio [194, 347–352] By employing VUV

probe pulses, the complete cascade of radiationless transitions from the $S_2(B_{2u})$ state to the electronic ground state could be monitored [194]. The experimentally observed decay rate of the $S_2(B_{2u})$ state of 20 fs [194, 352] is in excellent agreement with early quantum dynamics predictions [353] as well as with quasi-classical simulations [192, 309, 312]. On the other hand, no evidence of the computationally predicted rapid population of the $^1A_u(n\pi^*)$ state [188–190, 192] could be found in the experimental TRPE signals.

The simulation of the TRPE spectra of pyrazine was recently revisited with the ab initio quasi-classical DW approach described in the present review, employing the FSSH algorithm for the nonadiabatic trajectory dynamics. The comparison of the computed [336] and experimental [194] signals for resonant excitation of the bright $^1B_{2u}(\pi\pi^*)$ state are displayed as functions of time delay and photoelectron kinetic energy (PKE) in Figure 7. The calculations qualitatively reproduce the experimental observation of three bands near 1.1 eV (band 1), 2.5 eV (band 2) and 4.5 eV (band 3) and the evolution of their intensities with the delay time. Bands 1 and 3 increase in intensity with delay time, while band 2 markedly decreases in intensity. A closer analysis of the ionization channels of pyrazine (see Figure 5 of [336]) reveals that band 2 arises purely from the ionization of the initially excited $S_3(^1B_{2u})$ state to the $D_3(B_{2g})$ state of the pyrazine cation. The decay of this band therefore directly reports the lifetime of the $S_3(^1B_{2u})$ excited state (≈ 20 fs). Band 3 arises from the ionization of the $S_1(B_{3u})$ and $S_2(A_u)$ states to the $D_0(A_g)$ state of the cation, with a smaller contribution from the $S_3(B_{2u}) \rightarrow D_1(B_{1g})$ ionization. The rise of intensity of this band with delay time reflects the radiationless electronic population transfer from the $S_3(B_{2u})$ state to the $S_1(B_{3u})$ and $S_2(A_u)$ states.

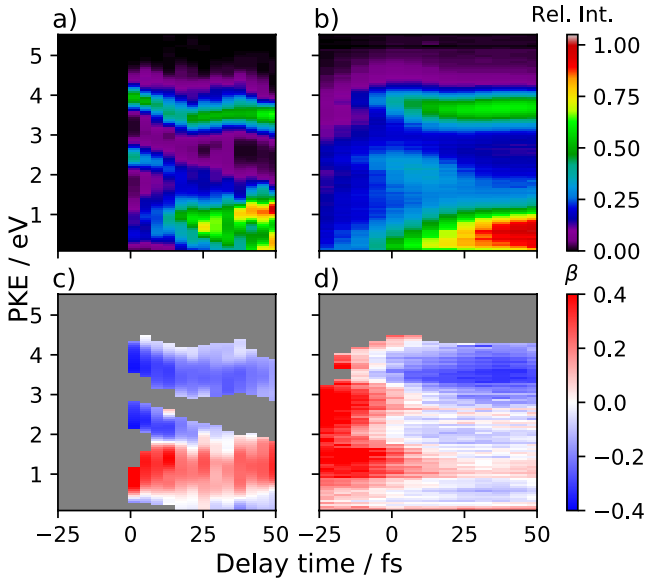

FIGURE 7 | Simulated (a, c) and experimental (b, d) time-resolved photoelectron spectra and anisotropy maps of pyrazine excited by a 4.7 eV (264 nm) pump pulse and ionized by a 9.3 eV (133 nm) probe pulse. The photoelectron spectrum was computed according to Equation (38). The experimental spectrum (b) is from [194] Adapted from [336] Copyright American Chemical Society.

Since the ionization cross sections of the $S_1(B_{3u})$ and $S_2(A_u)$ states are very similar, it is not possible to extract the population dynamics of the B_{3u} and A_u states from the integral TRPES signal. The low-energy band 1 arises primarily from the ionization of the $S_1(B_{3u})$ and $S_2(A_u)$ states to the $D_4(B_{3u})$, $D_5(B_{2u})$ and $D_7(B_{1u})$ channels, with minor contributions from the $S_3(B_{2u}) \rightarrow D_3(B_{2g})$ ionization. To describe the intensities of the different bands correctly, it is essential to include an accurate treatment of the ionization continuum. In the TRPES simulations of [336], the continuum one-particle wave functions were obtained in a multicenter B-spline basis at the SE-DFT level. Nevertheless, we notice that the intensity of band 1 near the threshold is underestimated. This is anticipated because the SE-DFT approach is known to be inadequate in the low-energy region. However, it appears that the increase in the intensity of band 1 is actually only delayed, which may be the result of the FSSH dynamics being too slow. Also, the experimental signal at very low energies (left part of band 1) may contain contributions from autoionizing Rydberg states and may additionally be contaminated by stray electrons.

The comparison between computed and experimental photoelectron angular distributions is shown in the lower panels of Figure 7. The data reveal that the photoionization process is fairly isotropic, as indicated by the relatively small variation of the β parameter with photoelectron kinetic energy (PKE), ranging from −0.4 to 0.2. However, a negative correlation with PKE is observed, which is consistent with the experimental findings. Specifically, in the PKE region below 2.5 eV, the β values are slightly positive (0.0–0.2), whereas in the range of 2.0 to 4.0 eV, β becomes negative, reaching approximately −0.4.

Very recently, the Suzuki group reported TRPES data for pyrazine with an unprecedented time resolution of 13 fs. With this time resolution and the high signal-to-noise ratio of photoelectron detection, it was possible to resolve for the first time the oscillatory dynamics of the tuning modes ν_1, ν_{6a} and ν_{9a} of the $^1B_{2u}/^1B_{3u}$ conical intersection. While the vibrations in the electronic ground state (detected in the GSB signal) are long lived, the vibrational dynamics in the excited states is damped on sub-ps time scales due to the $^1B_{2u}/^1B_{3u}$ conical intersection, as predicted by early simulations [353].

The photoinduced ring-opening of 1,3-cyclohexadiene (CHD) to 1,3,5-hexatriene (HT) is a classic example of a pericyclic reaction [354, 355] governed by the Woodward-Hoffmann (WH) rules [356–358]. This is one of the most studied reactions in photochemistry, both experimentally [359–365] and theoretically [363–377]. Specific computational studies include reaction path calculations [366, 368, 369], quantum dynamics simulations [370, 371, 378, 379] full-dimensional multiple spawning [363, 380, 381] and SH simulations [373–377]. These studies revealed that the reaction begins with optical excitation to the bright singly excited S_1 state, labeled 1^1B, and predominantly proceeds on the adiabatic S_1 surface until a conical intersection with the S_0 state is reached at around 70 fs [364, 365, 377]. At the S_1/S_0 conical intersection the reaction is either aborted and the system returns to the ground state of cyclic CHD, or continues, leading to the formation of HT with a yield slightly lower than 0.5. However, according to the WH rules, the conrotatory ring-opening of CHD is mediated by a doubly-excited electronic state with the same symmetry as the ground state (1^1A^-) [356–358].

This implies that a transition to a dark, doubly excited state must take place during the evolution on the adiabatic S_1 surface. It is typically assumed that this doubly excited state is the second excited state at the FC geometry, 2^1A^-.

The fact that the reaction takes place on a single adiabatic surface which arises from a mixture of several diabatic surfaces makes the unambiguous identification of the reactive state challenging (see Refs [364, 375, 377]). Polyak et al. [377] simulated the reaction with FSSH using the XMS-CASPT2 method and showed that a state with double excitation character, presumably 2^1A^-, contributes to the character of the S_1 and S_2 states at the minimum energy S_1/S_2 conical intersection and afterward.

From the experimental side, the reaction is best followed by photoelectron spectroscopy since the reactive state is optically dark. Recently, Suzuki and coworkers [364] decomposed the 2D maps of photoelectron spectra into contributions from two states, which they denoted S_1^* and S_1^{**} to highlight their single and double excitation character, but did not assign these states. In the experiment of Piancastelli and coworkers [365] the pump was at 267 nm and the probe was valence photoelectron spectroscopy with a photon energy of 19.23 eV.

The TRPE spectrum was calculated by Travnikova et al. using the DW computational protocol of Equations (26–38) [365]. A set of initial geometries **R** and momenta **P** as well as the initial excited state e were sampled from the doorway function, Equation (36). The FSSH algorithm was used to propagate the trajectories for 2000 fs in the manifold of the three lowest electronic states (S_0, S_1, S_2) using the XMS(3)-CASPT2(6,6) method and the cc-pVDZ basis set. The window function, Equation (37), describes the action of the probe. The time-resolved photoelectron spectrum $P(E_k, t)$ was obtained by averaging over all trajectories as given by Equation (38).

In the time-resolved valence photoelectron spectra of CHD, the signature of the excited-state dynamics is found in the low-binding-energy region (below 8 eV), whereas the 10 eV region is characteristic of GSB features (see Figure 1 of [365]). Figure 8a displays the simulated spectrum in the 3–7 eV binding energy range. Two bands are clearly visible. Band 1 begins at approximately 3.2 eV and its energy sharply increases within 15 fs. Beyond 15 fs, the energy saturates at a value of about 4.5 eV. At around 30 fs, band 1 loses intensity. This band originates from the $S_1 \rightarrow D_0$ transition. The increase in ionization energy is due to the motion towards the minimum of the S_1 state. This motion is accompanied by the extension of the C_1–C_6 bond which breaks during the isomerization process, and the energy of the ground state of the CHD cation (D_0) increases. Band 2 starts at 7.0 eV, but its energy quickly drops to the 5.8–6.2 eV binding energy range. The rapid stabilization of Band 2 is attributed to the crossing of the D_1 and D_2 states of the cation (see fig. S9 of [365]). Band 2 achieves maximum intensity at ~ 40 fs.

By comparing the average population of the adiabatic states (Figure 8b) with the time evolution of Bands 1 and 2, one sees that the decrease in intensity of band 1 corresponds to a transient

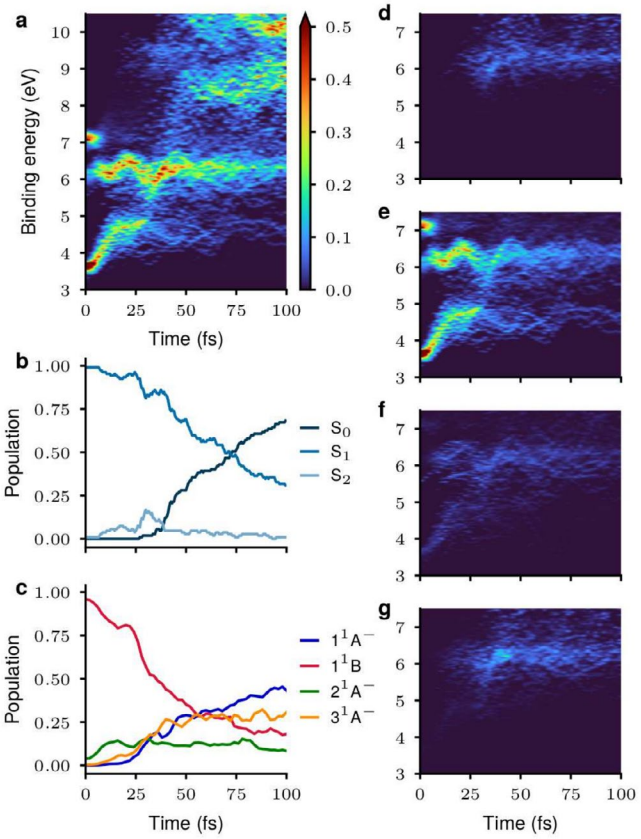

FIGURE 8 | Time resolved photoelectron spectra computed for short delay times. The ground-state bleach component is not taken into account. (b) Time evolution of the adiabatic population of electronic states obtained from SH nonadiabatic dynamics simulations. (c) Time evolution of the diabatic population of electronic states obtained by diabatization of electronic states along nonadiabatic trajectories. (d–g) Decomposition of the time-resolved photoelectron spectrum in terms of contributions of the diabatic states 1^1A^- (d), 1^1B (e), 2^1A^- (f), and 3^1A^- (g). Adapted from [365] Copyright American Chemical Society.

transfer of ~ 15 – 20% of the S_1 population to the S_2 state, peaking at around 30 fs. As for band 2, it is not possible to relate the maximum intensity of the band at ~ 40 fs to any change in the population of excited adiabatic states.

To resolve this issue, the time-dependent population probabilites of the diabatic states were computed. To this end, the diabatization scheme of Simah et al. [382] was extended from CASSCF to XMS-CASPT2 states. At the FC geometry, the energies of the lowest seven adiabatic states were computed using the XMS(6)-CASPT2(6,6) method. The states 2^1A^-, 1^1A^+, and 3^1A^-, located at 5.18 eV, 8.31 eV, and 8.66 eV, respectively, exhibit pronounced double excitation character. Inspection of the electron density differences between the excited states and the ground state revealed that excitation to the 1^1B (S_1 at the FC geometry) and high-lying 3^1A^- states leads to the depletion of electron density on the C_1–C_6 bond, which is to be broken. In contrast, excitation to the 2^1A^- and 1^1A^+ states leaves the electron density on that bond nearly unchanged. This is an indication that the previously unexplored 3^1A^- state plays a significant role in the ring-opening reaction of CHD.

The time evolution of the diabatic state populations, illustrated in Figure 8c, offers insight into the intricate dynamics of the ring-opening reaction. After the optical excitation of the adiabatic 1^1B state, its population steadily decreases. The diabatic 2^1A^- state is briefly populated early on, but its population never exceeds 0.2. Between ∼ 30 and 35 fs, the populations of the diabatic 1^1A^- (blue) and 3^1A^- (orange) states increase and the system evolves in the superposition of these two diabatic states [365]. The fate of the system at the S_1/S_0 conical intersection depends on the current character of the S_1 state. If the conical intersection is encountered while the S_1 state has dominantly 1^1A^- character, CHD is formed. Conversely, if the conical intersection is encountered while the S_1 state has dominant 3^1A^- character, HT is formed.

The photoelectron signals could be decomposed in [365] into contributions from the diabatic states. Figures 8d–g clearly show that the increase in the intensity of Band 2 at ∼ 40 fs originates from the 3^1A^- state. This result is in excellent agreement with the measurements of Suzuki and coworkers [364] where the authors concluded that the decay of the singly excited state $\left(S_1^*\right)$ population occurs in approximately 31–34 fs. Furthermore, panel (c) shows that the 2^1A^- state, which was considered to be the driving state, does not play a significant role in the dynamics.

The example of CHD isomerization confirms that TRPES is a powerful technique for the characterization of optically dark states. Again, theoretical support was necessary to extract relevant information and obtain a deeper understanding of the ring-opening reaction.

6 | Conclusions

The computation of femtosecond time-resolved spectroscopic signals from first principles is essential for thorough interpretations of experimental spectra. In the weak-field limit, the third-order dipole response functions are the basis for the calculation of pump-probe and four-wave mixing signals. However, the evaluation of the multi-time response functions and the calculation of the multiple integrals over intermediate time variables is challenging for first-principles descriptions of polyatomic chromophores. The combination of the DW approximation with quasi-classical or semi-classical trajectory descriptions of the nuclear motion greatly simplifies such calculations and enables the simulation of transient spectra with ab initio on-the-fly trajectory calculations.

In this article, the derivation of trajectory-based DW approximations from the quantum mechanical third-order response functions in an ab initio context is outlined in detail. The conditions for the applicability of the quasi-classical DW approximation are (i) non-overlapping pump and probe pulses, (ii) pulses that are short on the time scale of the intrinsic system dynamics, and (iii) the classical Condon approximation. In the DW approximation, the intrinsic system dynamics during the action of the laser pulses are neglected. The resulting expressions are well suited for evaluation by Monte Carlo sampling from ensembles of classical trajectories. Integral and dispersed TA PP spectra, 2D electronic spectra, and TRPES signals were considered as specific examples.

Quasi-classical trajectory simulations, such as Ehrenfest or SH simulations, provide information on the time evolution of the population probabilities of electronic states. Quasi-classical trajectory simulations, therefore, are restricted to spectroscopic signals that are not sensitive to electronic coherences generated by the laser pulses. For a rigorous treatment of electronic coherences induced by the laser pulses and possibly by the Liouvillian dynamics of the system, semi-classical trajectory-based propagation methods have to be used. Semi-classical methods derived from the Meyer-Miller-Stock-Thoss mapping Hamiltonian [101, 102], for example, have been tested for various few-state multi-mode models of molecular chromophores, and ab initio implementations can be expected in the near future.

While TRPES generally has been considered a different experiment that requires a separate theoretical description, the TRPES signal is included in the present formulation of the theory as a special case of the ESA contribution to the TA PP signal. In the TRPES signal, the bound upper states of the ESA contribution to the TA PP signal are replaced by a multi-channel electron scattering continuum.

In principle, any electronic-structure computational method and any quasi-classical or semi-classical trajectory protocol for the excited-state dynamics can be employed for the simulation of femtosecond time-resolved transient spectra. In the examples included in this review, either the computationally efficient single-reference ADC(2) method [195] or the multi-configuration CASSCF method [383] were employed. For the excited-state dynamics, two alternate SH protocols, Tully's FSSH algorithm [72] and Belyaev's LZ-based algorithm [77], were used. Very recently, the classical DW methodology was also interfaced with the on-the-fly Ehrenfest propagation method [384]. In addition, it was demonstrated that machine learning techniques can substantially facilitate numerical LZ-based SH simulations within the DW formalism [385].

The general computational protocol for the evaluation of transient signals with quasi-classical trajectory methods is given in Appendix G. It should be straightforward to adapt this protocol to the computation of other spectroscopic signals and to implement it with alternate electronic-structure methods or quasi-classical trajectory methods. The sampling from the quasi-classical doorway distribution does not cost more than the standard sampling from the Wigner distribution, whereas the evaluation of the window function involves more computational effort than the evaluation of time-dependent electronic population probabilities. In the case of the TRPES signal, the computation of sufficiently accurate electronic continuum wave functions represents a considerable challenge. Oversimplified models, such as plane waves or Coulomb-distorted waves, are in general not sufficient for reliable simulations of TRPES signals [335].

In general, the accuracy of first-principles simulations of time-resolved nonlinear spectra is limited by the accuracy of the underlying ab initio electronic-structure method and by the accuracy of the quasi-classical or semi-classical approximation method. At the present stage, the limitations of the electronic-structure protocols may be more severe than the limitations of the quasi-classical or semi-classical protocols, because only

computationally inexpensive electronic-structure methods (such as single-reference methods or strongly restricted multi-configuration methods) can be employed. Considering the current rapid progress in the construction of computationally efficient multi-sheeted multi-dimensional potential-energy surfaces with machine-learning techniques, the electronic-structure bottleneck may possibly become less severe in the near future. There is currently also significant progress in the development of ever more accurate trajectory-based quasi-classical or semi-classical approximation methods. Eventually, the inaccuracies inherent in the DW approximation may become the limiting factor and more advanced approximations of the third-order response functions have to be considered.

This review is restricted to the consideration of time-resolved nonlinear signals of isolated molecular systems (experimentally, dilute ensembles of chromophores). Needless to say, many experimental fs-time-resolved spectra are recorded for chromophores in solution, for molecular aggregates, or for extended materials. Even classic gas-phase techniques, such as transient X-ray spectroscopy or TRPES, have been extended to the condensed phase by using liquid jets in vacuum [386–388]. While the extension of the formal theory of time-resolved third-order signals to condensed phases at the empirical level is well established [8], simulations of time-resolved signals for condensed phases with all-atom DFT [389–391] or QM/MM methods [392, 393] are challenges for future research.

Author Contributions

Maxim F. Gelin: conceptualization (equal), writing – original draft (equal), writing – review and editing (equal). **Zhenggang Lan:** conceptualization (equal), writing – original draft (equal), writing – review and editing (equal). **Nađa Došlić:** conceptualization (equal), writing – original draft (equal), writing – review and editing (equal). **Wolfgang Domcke:** conceptualization (equal), writing – original draft (equal), writing – review and editing (equal).

Acknowledgments

M.F.G. acknowledges support from the National Natural Science Foundation of China (No. 22373028). Z.L. acknowledges support from the National Natural Science Foundation of China (No. 22333003, 22361132528, 21933011) N.D. acknowledges support from the Croatian Science Foundation (HRZZ grant no. HRZZ-IP-2022-10-4658). Open Access funding enabled and organized by Projekt DEAL.

Conflicts of Interest

The authors declare no conflicts of interest.

Data Availability Statement

Data sharing is not applicable to this article as no new data were created or analyzed in this study.

Related WIREs Articles

Newton-X: a surface-hopping program for nonadiabatic molecular dynamic

Theoretical study of excitation energy transfer and nonlinear spectroscopy

Time-resolved photoelectron spectroscopy via trajectory surface hopping

References

1. C. V. Shank and B. I. Greene, "Femtosecond Spectroscopy and Chemistry," *Journal of Physical Chemistry* 87 (1983): 732–734.

2. G. R. Fleming, "Subpicosecond Spectroscopy," *Annual Review of Physical Chemistry* 37 (1986): 81–104.

3. U. Megerle, I. Pugliesi, C. Schriever, and E. Riedle, "Sub-50 Fs Broadband Absorption Spectroscopy With Tunable Excitation: Putting the Analysis of Ultrafast Molecular Dynamics on Solid Ground," *Applied Physics B: Lasers and Optics* 96 (2009): 215–231.

4. M. Chergui, "Ultrafast Molecular Photophysics in the Deep Ultraviolet," *Journal of Chemical Physics* 150 (2019): 070901.

5. T. Suzuki, "Ultrafast Electronic Dynamics in Polyatomic Molecules Studied Using Femtosecond Vacuum Ultraviolet and x-Ray Pulses," *Journal of Physics B: Atomic, Molecular and Optical Physics* 47 (2014): 124001.

6. L. Fang, T. Osipov, B. F. Murphy, et al., "Probing Ultrafast Electronic and Molecular Dynamics With Free-Electron Lasers," *Journal of Physics B: Atomic, Molecular and Optical Physics* 47 (2014): 124006.

7. A. Bhattacherjee and S. R. Leone, "Ultrafast x-Ray Transient Absorption Spectroscopy of Gas-Phase Photochemical Reactions: A New Universal Probe of Photoinduced Molecular Dynamics," *Accounts of Chemical Research* 51 (2018): 3203–3211.

8. S. Mukamel, *Principles of Nonlinear Optical Spectroscopy* (Oxford University Press, 1995).

9. D. Polli, L. Lüer, and G. Cerullo, "High-Time-Resolution Pump-Probe System With Broadband Detection for the Study of Time-Domain Vibrational Dynamics," *Review of Scientific Instruments* 78 (2007): 103–108.

10. P. Tian, D. Keusters, Y. Suzaki, and W. S. Warren, "Femtosecond Phase-Coherent Twodimensional Spectroscopy," *Science* 300 (2003): 1553–1555.

11. D. M. Jonas, "Two-Dimensional Femtosecond Spectroscopy," *Annual Review of Physical Chemistry* 54 (2003): 425–463.

12. F. D. Fuller and J. P. Ogilvie, "Experimental Implementations of Two-Dimensional Fourier Transform Electronic Spectroscopy," *Annual Review of Physical Chemistry* 66 (2015): 667–690.

13. M. Cho, *Two-Dimensional Optical Spectroscopy* (CRC Press, 2009).

14. T. J. A. Wolf, R. H. Myhre, J. P. Cryan, et al., "Probing Ultrafast $\pi\pi^*/n\pi^*$ Internal Conversion in Organic Chromophores via K-Edge Resonant Absorption," *Nature Communications* 8 (2017): 29.

15. A. Assion, M. Geisler, J. Helbing, V. Seyfried, and T. Baumert, "Femtosecond Pump-Probe Photoelectron Spectroscopy: Mapping of Vibrational Wave-Packet Motion," *Physical Review A* 54 (1996): R4605–R4608.

16. V. Blanchet, M. Z. Zgierski, T. Seideman, and A. Stolow, "Discerning Vibronic Molecular Dynamics Using Time-Resolved Photoelectron Spectroscopy," *Nature* 401 (1999): 52–54.

17. V. Stert, W. Radloff, C. P. Schulz, and I. V. Hertel, "Ultrafast Photoelectron Spectroscopy: Femtosecond Pump-Probe Coincidence Detection of Ammonia Cluster Ions and Electrons," *European Physical Journal D: Atomic, Molecular, Optical and Plasma Physics* 5 (1999): 97–106.

18. A. Stolow, A. E. Bragg, and D. M. Neumark, "Femtosecond Time-Resolved Photoelectron Spectroscopy," *Chemical Reviews* 104 (2004): 1719–1757.

19. T. Suzuki, "Femtosecond Time-Resolved Photoelectron Imaging," *Annual Review of Physical Chemistry* 57 (2006): 555–592.

20. A. Stolow and J. G. Underwood, "Time-Resolved Photoelectron Spectroscopy," *Advances in Chemical Physics* 139 (2008): 497–583.

21. H. H. Fielding and G. A. Worth, "Using Time-Resolved Photoelectron Spectroscopy to Unravel the Electronic Relaxation Dynamics of Photoexcited Molecules," *Chemical Society Reviews* 47 (2018): 309–321.

22. M. S. Schuurman and V. Blanchet, "Time-Resolved Photoelectron Spectroscopy: The Continuing Evolution of a Mature Technique," *Physical Chemistry Chemical Physics* 24 (2022): 20012–20024.

23. P. Hamm and M. Zanni, *Concepts and Methods of 2D Infrared Spectroscopy* (Cambridge University Press, 2011).

24. L. Seidner, G. Stock, and W. Domcke, "Nonperturbative Approach to Femtosecond Spectroscopy: General Theory and Application to Multidimensional Nonadiabatic Photoisomerization Processes," *Journal of Chemical Physics* 103 (1995): 3998–4011.

25. T. Kato and Y. Tanimura, "Multi-Dimensional Vibrational Spectroscopy Measured From Different Phase-Matching Conditions," *Chemical Physics Letters* 341 (2001): 329–337.

26. S. Meyer and V. Engel, "Non-Perturbative Wave-Packet Calculations of Time-Resolved Four-Wave-Mixing Signals," *Applied Physics B: Lasers and Optics* 71 (2000): 293–297.

27. H. Wang and M. Thoss, "Nonperturbative Quantum Simulation of Pump-Probe Spectra for Electron-Transfer Reactions in the Condensed Phase," *Chemical Physics Letters* 389 (2004): 43–50.

28. M. F. Gelin, B. J. Rao, M. Nest, and W. Domcke, "Domain of Validity of the Perturbative Approach to Femtosecond Optical Spectroscopy," *Journal of Chemical Physics* 139 (2013): 224107.

29. J. Lüttig, P. A. Rose, P. Maly, et al., "High-Order Pump-Probe and High-Order Two-Dimensional Electronic Spectroscopy on the Example of Squaraine Oligomers," *Journal of Chemical Physics* 158 (2023): 234201.

30. M. F. Gelin, L. Chen, and W. Domcke, "Equation-Of-Motion Methods for the Calculation of Femtosecond Time-Resolved 4-Wave-Mixing and N-Wave Mixing Signals," *Chemical Reviews* 122, 17 (2022): 17339–17396.

31. D. Keusters, H.-S. Tan, and W. S. Warren, "Role of Pulse Phase and Direction in Two-Dimensional Optical Spectroscopy," *Journal of Physical Chemistry A* 103 (1999): 10369–10380.

32. P. F. Tekavec, G. A. Lott, and A. H. Marcus, "Fluorescence-Detected Two-Dimensional Electronic Coherence Spectroscopy by Accusto-Optic Phase Modulation," *Journal of Chemical Physics* 127 (2007): 214307.

33. M. Seel and W. Domcke, "Femtosecond Time-Resolved Ionization Spectroscopy of Ultrafast Internal-Conversion Dynamics in Polyatomic Molecules: Theory and Computational Studies," *Journal of Chemical Physics* 95 (1991): 7806–7822.

34. C. Meier and V. Engel, "Electron Kinetic Energy Distributions From Multiphoton Ionization of Na_2 With Femtosecond Laser Pulses," *Chemical Physics Letters* 212 (1993): 691–696.

35. T. Seideman, "Time-Resolved Photoelectron Angular Distributions: A Nonperturbative Theory," *Journal of Chemical Physics* 107 (1997): 7859–7868.

36. C. Meier, V. Engel, and U. Manthe, "An Effective Method for the Quantum Mechanical Description of Photoionization With Ultrashort Laser Pulses," *Journal of Chemical Physics* 109 (1998): 36–41.

37. Y. Arasaki, K. Takatsuka, K. Wang, and V. McKoy, "Femtosecond Energy- and Angle-Resolved Photoelectron Spectra," *Chemical Physics Letters* 302 (1999): 363–374.

38. M. Klessinger and J. Michl, *Excited States and Photochemistry of Organic Molecules* (VCH, 1995).

39. F. Bernardi, M. Olivucci, and M. A. Robb, "Potential Energy Surface Crossings in Organic Photochemistry," *Chemical Society Reviews* 25 (1996): 321–328.

40. D. R. Yarkony, "Diabolical Conical Intersections," *Reviews of Modern Physics* 68 (1996): 985–1013.

41. W. Domcke, D. Yarkony, and H. Köppel, eds., "Conical Intersections: Electronic Structure, Dynamics & Spectroscopy," in *Advanced Series in Physical Chemistry* (World Scientific, 2004).

42. M. Baer, *Beyond Born-Oppenheimer: Conical Intersections and Nonadiabatic Coupling Terms* (Wiley Interscience, 2006).

43. W. Domcke, D. Yarkony, and H. Köppel, eds., "Conical Intersections: Theory, Computation and Experiment," in *Advanced Series in Physical Chemistry* (World Scientific, 2011).

44. S. Matsika and P. Krause, "Nonadiabatic Events and Conical Intersections," *Annual Review of Physical Chemistry* 62 (2011): 621–643.

45. M. S. Schuurman and A. Stolow, "Dynamics at Conical Intersections," *Annual Review of Physical Chemistry* 69 (2018): 427–450.

46. H. Köppel, W. Domcke, and L. S. Cederbaum, "Multimode Molecular Dynamics Beyond the Born-Oppenheimer Approximation," *Advances in Chemical Physics* 57 (1984): 59–246.

47. W. Domcke and G. Stock, "Theory of Ultrafast Nonadiabatic Excited-State Processes and Their Spectroscopic Detection in Real Time," *Advances in Chemical Physics* 100 (1997): 1–169.

48. G. A. Worth and L. S. Cederbaum, "Beyond Born-Oppenheimer: Molecular Dynamics Through a Conical Intersection," *Annual Review of Physical Chemistry* 55 (2004): 127–158.

49. B. G. Levine and T. J. Martínez, "Isomerization Through Conical Intersections," *Annual Review of Physical Chemistry* 58 (2007): 613–634.

50. M. H. Beck, G. A. Jäckle, G. A. Worth, and H.-D. Meyer, "The Multiconfiguration Time-Dependent Hartree (MCTDH) Method: A Highly Efficient Algorithm for Propagating Wavepackets," *Physics Reports* 324 (2000): 1–105.

51. H.-D. Meyer, F. Gatti, and G. A. Worth, eds., *Multidimensional Quantum Dynamics: MCTDH Theory and Applications* (Wiley-VCH, 2009).

52. U. Manthe, "Wavepacket Dynamics and the Multi-Configurational Time-Dependent Hartree Approach," *Journal of Physics. Condensed Matter* 29 (2017): 253001.

53. I. V. Oseledets and E. E. Tyrtyshnikov, "Breaking the Curse of Dimensionality and or How to Use SVD in Many Dimensions," *SIAM Journal on Scientific Computing* 31 (2009): 3744–3759.

54. Y. Kurashige, "Matrix Product State Formulation of the Multiconfiguration Time-Dependent Hartree Theory," *Journal of Chemical Physics* 149 194 (2018): 194114.

55. B. Kloss, Y. Bar Lev, and D. Reichman, "Time-Dependent Variational Principle in Matrix Product State Manifolds: Pitfalls and Potential," *Physical Review B* 97 (2018): 024307.

56. T. G. Kolda and T. W. Bader, "Tensor Decompositions and Applications," *SIAM Review* 51 (2009): 455–500.

57. I. V. Oseledets, "Tensor-Train Decomposition," *SIAM Journal on Scientific Computing* 33 (2011): 2295–2317.

58. C. Lubich, I. V. Oseledets, and B. Vandereycken, "Time Integration of Tensor Trains," *SIAM Journal on Numerical Analysis* 53 (2015): 917–941.

59. H. R. Larsson, "A Tensor Network View of the Multilayer Multiconfiguration Time-Dependent Hartree Methods," *Molecular Physics* 122 (2024): e2306881.

60. M. Ben-Nun and T. J. Martínez, "Ab Initio Quantum Molecular Dynamics," *Advances in Chemical Physics* 121 (2002): 439–512.

61. X. Li, J. C. Tully, H. B. Schlegel, and M. J. Frisch, "Ab Initio Ehrenfest Dynamics," *Journal of Chemical Physics* 123 (2005): 084106.

62. B. F. E. Curchod, U. Rothlisberger, and I. Tavernelli, "Trajectory-Based Nonadiabatic Dynamics With Time-Dependent Density Functional Theory," *ChemPhysChem* 14 (2013): 1314–1340.

63. M. Persico, G. Granucci, "An Overview of Nonadiabatic Dynamics Simulation Methods, With Focus on the Direct Approach Versus the Fitting of Potential Energy Surfaces," *Theoretical Chemistry Accounts* 133 (2014): 1526.

64. S. Pratihar, X. Ma, Z. Homayoon, G. L. Barnes, and W. L. Hase, "Direct Chemical Dynamics Simulations," *Journal of the American Chemical Society* 139 (2017): 3570–3590.

65. R. Crespo-Otero and M. Barbatti, "Recent Advances and Perspectives on Nonadiabatic Mixed Quantum-Classical Dynamics," *Chemical Reviews* 118 (2018): 7026–7068.

66. N. F. Mott, "On the Theory of Excitation by Collision With Heavy Particles," *Proceedings of the Cambridge Philosophical Society* 27 (1931): 553–560.

67. W. B. Case, "Wigner Functions and Weyl Transforms for Pedestrians," *American Journal of Physics* 76 (2008): 937–946.

68. D. J. Diestler, "Analysis of Infrared Absorption Line Shapes in Condensed Media: Application of a Classical Limit of Heisenberg's Equations of Motion," *Journal of Chemical Physics* 78 (1983): 2240–2247.

69. H. J. C. Berendsen and J. Mavri, "Quantum Simulation of Reaction Dynamics by Density Matrix Evolution," *Journal of Physical Chemistry* 97 (1993): 13464–13468.

70. G. Stock, "Classical Description of Nonadiabatic Photoisomerization Processes and Their Real-Time Detection via Femtosecond Spectroscopy," *Journal of Chemical Physics* 103 (1995): 10015–10029.

71. D. V. Shalashilin, "Multiconfigurational Ehrenfest Approach to Quantum Coherent Dynamics in Large Molecular Systems," *Faraday Discussions* 153 (2011): 105–116.

72. J. C. Tully and R. K. Preston, "Trajectory Surface Hopping Approach to Nonadiabatic Molecular Collisions: The Reaction of H^+ With D_2," *Journal of Chemical Physics* 55 (1971): 562–572.

73. E. Nikitin and S. Umanskii, "General Formulation of Scattering Problem Under Quasiclassical Conditions," in *Theory of Slow Atomic Collisions* (Springer, 1984).

74. J. C. Tully, "Molecular Dynamics With Electronic Transitions," *Journal of Chemical Physics* 93 (1990): 1061–1071.

75. G. Grannucci and M. Persico, "Critical Appraisal of the Fewest Switches Algorithm for Surface Hopping," *Journal of Chemical Physics* 126 (2007): 134114.

76. A. K. Belyaev and O. V. Lebedev, "Nonadiabatic Nuclear Dynamics of Atomic Collisions Based on Branching Classical Trajectories," *Physical Review A* 2011 (2015): 84.

77. A. K. Belyaev, C. Lasser, and G. Triglia, "Landau-Zener Type Surface Hopping Algorithms," *Journal of Chemical Physics* 140 (2014): 224108.

78. C. Zhu, K. Nobusada, and H. Nakamura, "New Implementation of the Trajectory Surface Hopping Method With the Use of the Zhu-Nakamura Theory," *Journal of Chemical Physics* 115 (2001): 3031–3044.

79. L. Yu, C. Xu, Y. Lei, C. Zhu, and Z. Wen, "Trajectory-Based Nonadiabatic Molecular Dynamics Without Calculating Nonadiabatic Coupling in the Avoided Crossing Case: Trans-Cis Photoisomerization in Azobenzene," *Physical Chemistry Chemical Physics* 16 (2014): 25883–25895.

80. X. Huang and W. Domcke, "Ab Initio Trajectory Surface-Hopping Dynamics Studies of Excited-State Proton-Coupled Electron Transfer Reactions in Trianisoleheptazine-Phenol Complexes," *Physical Chemistry Chemical Physics* 24 (2022): 15925–15936.

81. A. Abedi, N. T. Maitra, and E. K. U. Gross, "Exact Factorization of the Time-Dependent Electron-Nuclear Wave Function," *Physical Review Letters* 105 (2010): 123002.

82. A. Abedi, N. T. Maitra, and E. K. U. Gross, "Correlated Electron-Nuclear Dynamics: Exact Factorization of the Molecular Wave Function," *Journal of Chemical Physics* 137 (2012): 22A530.

83. J.-K. Ha, I. S. Lee, and S. K. Min, "Surface Hopping Dynamics Beyond Nonadiabatic Couplings for Quantum Coherence," *Journal of Physical Chemistry Letters* 9 (2018): 1097–1104.

84. C. Pieroni and F. Agostini, "Nonadiabatic Dynamics With Coupled Trajectories," *Journal of Chemical Theory and Computation* 17 (2021): 5969–5991.

85. F. F. de Carvalho, M. E. E. Bouduban, B. F. E. Curchod, and I. Tavernelli, "Nonadiabatic Molecular Dynamics Based on Trajectories," *Entropy* 16 (2014): 62–85.

86. L. M. Ibele, Y. Lassmann, T. J. Martinez, and B. F. E. Curchod, "Comparing (Stochastic Selection) Ab Initio Multiple Spawning With Trajectory Surface Hopping for the Photodynamics of Cyclopropanone, Fulvene, and Dithiane," *Journal of Chemical Physics* 154 (2021): 104110.

87. V. M. Freixas, A. J. White, T. Nelson, et al., "Nonadiabatic Excited-State Molecular Dynamics Methodologies: Comparison and Convergence," *Journal of Physical Chemistry Letters* 12 (2021): 2970–2982.

88. E. X. Salazar, M. F. S. J. Menger, and S. Faraji, "Ultrafast Photoinduced Dynamics in 1,3-Cyclohexadiene: A Comparison of Trajectory Surface Hopping Schemes," *Journal of Chemical Theory and Computation* 20 (2024): 5796–5806.

89. R. S. Mattos, S. Mukherjee, and M. Barbatti, "Quantum Dynamics From Classical Trajectories," *Journal of Chemical Theory and Computation* 20 (2024): 7728–7743.

90. E. J. Heller, "Time-Dependent Approach to Semiclassical Dynamics," *Journal of Chemical Physics* 62 (1975): 1544–1555.

91. E. J. Heller, "Time-Dependent Variational Approach to Semiclassical Dynamics," *Journal of Chemical Physics* 64 (1976): 63–73.

92. P. A. Kovac and J. A. Cina, "Mixed Quantum/Semiclassical Wave-Packet Dynamical Method for Condensed-Phase Molecular Spectroscopy Signals," *Journal of Chemical Physics* 147 (2017): 224112.

93. A. Patoz, T. Begušić, and J. Vaníček, "On-The-Fly Ab Initio Semicalssical Evaluation of Absorption Spectra of Polyatomic Molecules Beyond the Condon Approximation," *Journal of Physical Chemistry Letters* 9 (2018): 2367–2372.

94. T. Begušić and J. Vaníček, "On-The-Fly Ab Initio Semiclassical Evaluation of Third-Order Response Functions for Two-Dimensional Electronic Spectroscopy," *Journal of Chemical Physics* 153 (2020): 184110.

95. M. J. Davis and E. J. Heller, "Semiclassical Gaussian Basis Set Method for Molecular Vibrational Wave Functions," *Journal of Chemical Physics* 71 (1979): 3383–3395.

96. M. Ben-Nun and T. J. Martínez, "Nonadiabatic Molecular Dynamics: Validation of the Multiple Spawning Method for a Multidimensional Problem," *Journal of Chemical Physics* 108 (1998): 7244–7257.

97. R. Brook, C. Symonds, and D. V. Shalashilin, "Full Wave Function Cloning for Improving Convergence of the Multiconfigurational Ehrenfest Method: Tests in the Zero-Temperature Spin-Boson Model Regime," *Journal of Chemical Physics* 161 (2024): 064102.

98. G. A. Worth, M. A. Robb, and I. Burghardt, "A Novel Algorithm for Non-Adiabatic Direct Dynamics Using Variational Gaussian Wavepackets," *Faraday Discussions* 127 (2004): 307–323.

99. M. C. Gutzwiller, *Chaos in Classical and Quantum Mechanics* (Springer, 1990).

100. M. F. Herman and E. Kluk, "A Semiclassical Justification of the Use of Non-Spreading Wavepackets in Dynamics Calculations," *Chemical Physics* 91 (1984): 27–34.

101. H. D. Meyer and W. H. Miller, "A Classical Analog for Electronic Degrees of Freedom in Nonadiabatic Collision Processes," *Journal of Chemical Physics* 70 (1979): 3214–3223.

102. G. Stock and M. Thoss, "Semiclassical Description of Nonadiabatic Quantum Dynamics," *Physical Review Letters* 78 (1997): 578–581.

103. J. Schwinger, *Quantum Theory of Angular Momentum*, eds B. L. B. Biedenharn and H. V. Dam (Academic Press, 1965).

104. J. Liu, "A Unified Theoretical Framework for Mapping Models for the Multi-State Hamiltonian," *Journal of Chemical Physics* 145 (2016): 204105.

105. J. E. Runeson and J. O. Richardson, "Spin-Mapping Approach for Nonadiabatic Dynamics," *Journal of Chemical Physics* 151 (2019): 044119.

106. X. Gao, M. A. C. Saller, Y. Liu, A. Kelly, J. O. Richardson, and E. Geva, "Benchmarking Quasiclassical Mapping Hamiltonian Methods for Simulating Electronically Nonadiabatic Molecular Dynamics," *Journal of Chemical Theory and Computation* 16 (2020): 2883–2895.

107. J. E. Runeson and J. O. Richardson, "Generalized Spin Mapping for Quantum-Classical Dynamics," *Journal of Chemical Physics* 152 (2020): 084110.

108. X. He, B. Wu, Y. Shang, B. Li, X. Cheng, and J. Liu, "New Phase Space Formulations and Quantum Dynamics Approaches," *WIREs Computational Molecular Science* 12 (2022): e1619.

109. J. E. Runeson and D. E. Manolopoulos, "A Multi-State Mapping Approach to Surface Hopping," *Journal of Chemical Physics* 159 (2023): 094115.

110. B. Wu, X. He, and J. Liu, "Nonadiabatic Field on Quantum Phase Space: A Century After Ehrenfest," *Journal of Physical Chemistry Letters* 15 (2024): 644–658.

111. R. Kapral, "Progress in the Theory of Mixed Quantum-Classical Dynamics," *Annual Review of Physical Chemistry* 57 (2006): 129–157.

112. Q. Shi and E. Geva, "A Derivation of the Mixed Quantum-Classical Liouville Equation From the Influence Functional Formalism," *Journal of Chemical Physics* 121 (2004): 3393–3404.

113. Y. R. Shen, *The Principles of Nonlinear Optics* (Wiley, 1984).

114. I. Conti, G. Cerullo, A. Nenov, and M. Garavelli, "Ultrafast Spectroscopy of Photoactive Molecular Systems From First Principles: Where We Stand Today and Where We Are Going," *Journal of the American Chemical Society* 142 (2020): 16117–16139.

115. T. L. C. Jansen, "Computational Spectroscopy of Complex Systems," *Journal of Chemical Physics* 155 (2021): 170901.

116. J. Krumland, M. Guerrini, A. De Sio, C. Lienau, and C. Cocchi, "Two-Dimensional Electronic Spectroscopy From First Principles," *Applied Physics Reviews* 11 (2024): 011305.

117. S. Faraji, D. Picconi, and E. Palacino-González, "Advanced Quantum and Semiclassical Methods for Simulating Photoinduced Molecular Dynamics and Spectroscopy," *WIREs Computational Molecular Science* 14 (2024): e1731.

118. Y. J. Yan, L. E. Fried, and S. Mukamel, "Ultrafast Pump-Probe Spectroscopy: Femtosecond Dynamics in Liouville Space," *Journal of Physical Chemistry* 93 (1989): 8149–8162.

119. Y. J. Yan and S. Mukamel, "Femtosecond Pump-Probe Spectroscopy of Polyatomic Molecules in Condensed Phases," *Physical Review A* 41 (1990): 6485–6504.

120. L. E. Fried and S. Mukamel, "A Classical Theory of Pump-Probe Photodissociation for Arbitrary Pulse Durations," *Journal of Chemical Physics* 93 (1990): 3063–3071.

121. A. Okada, V. Chernyak, and S. Mukamel, "Solvent Reorganization in Long-Range Electron Transfer: Density Matrix Approach," *Journal of Physical Chemistry* A 102 (1998): 1241–1251.

122. V. Chernyak, T. Minami, and S. Mukamel, "Exciton Transport in Molecular Aggregates Probed by Time and Frequency Gated Optical Spectroscopy," *Journal of Chemical Physics* 112 (2000): 7953–7963.

123. J. C. Kirkwood, C. Scheurer, V. Chernyak, and S. Mukamel, "Simulations of Energy Funneling and Time- and Frequency-Gated Fluorescence in Dendrimers," *Journal of Chemical Physics* 114 (2001): 2419–2429.

124. M. F. Gelin, A. V. Pisliakov, and W. Domcke, "Time and Frequency Gated Spontaneous Emission as a Tool for Studying Vibrational Dynamics in the Excited State," *Physical Review A* 65 (2002): 062507.

125. A. V. Pisliakov, M. F. Gelin, and W. Domcke, "Detection of Electronic and Vibrational Coherence Effects in Electron-Transfer Systems by Femtosecond Time-Resolved Fluorescence Spectroscopy: Theoretical Aspects," *Journal of Physical Chemistry A* 107 (2003): 2657–2666.

126. R. Tempelaar, F. C. Spano, J. Knoester, and T. L. C. Jansen, "Mapping the Evolution of Spatial Exciton Coherence Through Time-Resolved Fluorescence," *Journal of Physical Chemistry Letters* 5 (2014): 1505–1510.

127. P. C. Arpin and D. B. Turner, "Signatures of Vibrational and Electronic Quantum Beats in Femtosecond Coherence Spectra," *Journal of Physical Chemistry A* 125 (2021): 2425–2435.

128. V. Novoderezhkin, R. Monshouwer, and R. van Grondelle, "Electronic and Vibrational Coherence in the Core Light-Harvesting Antenna of Rhodopseudomonas Viridis," *Journal of Physical Chemistry B* 104 (2000): 12056–12071.

129. V. I. Novoderezhkin, M. A. Palacios, H. van Amerongen, and R. van Grondelle, "Energy Transfer Dynamics in the LHCII Complex of Higher Plants: Modified Redfield Approach," *Journal of Physical Chemistry B* 108 (2004): 10363–10375.

130. B. Balzer and G. Stock, "Transient Spectral Features of a Cis-Trans Photoreaction in the Condensed Phase: A Model Study," *Journal of Physical Chemistry A* 108 (2004): 6464–6473.

131. W. M. Zhang, T. Meier, V. Chernyak, and S. Mukamel, "Exciton-Migration and Three-Pulse Femtosecond Optical Spectroscopies of Photosynthetic Antenna Complexes," *Journal of Chemical Physics* 108 (1998): 7763–7774.

132. S. Mukamel and D. Abramavicius, "Many-Body Approaches for Simulating Coherent Nonlinear Spectroscopies of Electronic and Vibrational Excitons," *Chemical Reviews* 104 (2004): 2073–2098.

133. D. Abramavicius, B. Palmieri, D. V. Voronine, F. Šanda, and S. Mukamel, "Coherent Multidimensional Optical Spectroscopy of Excitons in Molecular Aggregates and Quasiparticle vs. Supermolecule Perspective," *Chemical Reviews* 109 (2009): 2350–2408.

134. M. F. Gelin, A. V. Pisliakov, D. Egorova, and W. Domcke, "A Simple Model for the Calculation of Nonlinear Optical Response Functions and Femtosecond Time-Resolved Spectra," *Journal of Chemical Physics* 118 (2003): 5287–5301.

135. T. Hasegawa and Y. Tanimura, "Nonequilibrium Molecular Dynamics Simulations With a Backward-Forward Trajectories Sampling for Multidimensional Infrared Spectroscopy of Molecular Vibrational Modes," *Journal of Chemical Physics* 128 (2008): 064511.

136. T. Mančal and V. May, "Interplay of Non-Markovian Relaxation and Ultrafast Optical State Preparation in Molecular Systems: The Laguerre Polynomial Method," *Journal of Chemical Physics* 114 (2001): 1510–1523.

137. M. F. Gelin, D. Egorova, A. V. Pisliakov, and W. Domcke, "Unified Description of Sequential and Coherent Contributions to Time-Resolved Spontaneous Emission Signals: Generalized Doorway-Window Approach," *Chemical Physics Letters* 391 (2004): 234–242.

138. M. F. Gelin, D. Egorova, A. V. Pisliakov, and W. Domcke, "Transient Phenomena in Time- and Frequency-Gated Spontaneous Emission," *Journal of Physical Chemistry A* 109 (2005): 3587–3597.

139. M. F. Gelin and D. S. Kosov, "Doorway-Window Description of Sequential Three-Pulse Photon Echo Signals," *Chemical Physics* 347 (2008): 177–184.

140. M. F. Gelin and W. Domcke, "Alternative View of Two-Dimensional Spectroscopy," *Journal of Chemical Physics* 144 (2016): 194104.

141. V. I. Novoderezhkin, T. A. Cohen Stuart, and R. van Grondelle, "Dynamics of Exciton Relaxation in LH2 Antenna Probed by Multipulse Nonlinear Spectroscopy," *Journal of Physical Chemistry A* 115 (2011): 3834–3844.

142. M. F. Gelin, D. Egorova, and W. Domcke, "Manipulating Electronic Couplings and Nonadiabatic Nuclear Dynamics With Strong Laser Pulses," *Journal of Chemical Physics* 131 (2009): 124505.

143. M. F. Gelin, D. Egorova, and W. Domcke, "Optical N-Wave-Mixing Spectroscopy With Strong and Temporally Well-Separated Pulses: The Doorway-Window Representation," *Journal of Physical Chemistry B* 115 (2011): 5648–5658.

144. M. F. Gelin, D. Egorova, and W. Domcke, "Strong-Pump Strong-Probe Spectroscopy: Effects of Higher Excited Electronic States," *Physical Chemistry Chemical Physics* 15 (2013): 8119–8131.

145. L. Chen, E. Palacino-González, M. F. Gelin, and W. Domcke, "Nonperturbative Response Functions: A Tool for the Interpretation of Four-Wave-Mixing Signals Beyond Third Order," *Journal of Chemical Physics* 147 (2017): 234104.

146. G. Bressan and J. J. van Thor, "Theory of Two-Dimensional Spectroscopy With Intense Laser Fields," *Journal of Chemical Physics* 154 (2021): 244111.

147. Y. Tanimura and S. Mukamel, "Real-Time Path-Integral Approach to Quantum Coherence and Dephasing in Nonadiabatic Transitions and Nonlinear Optical Response," *Physical Review E* 47 (1993): 118–136.

148. Y. Tanimura and S. Mukamel, "Description of Nonlinear Optical Response Using Phase Space Wave Packets," *Journal of Physical Chemistry* 97 (1993): 12596–12601.

149. J. Olsina and T. Mančal, "Parametric Projection Operator Technique for Second Order Nonlinear Response," *Chemical Physics* 404 (2012): 103–115.

150. W. P. de Boeij, M. S. Pshenichnikov, and D. A. Wiersma, "Heterodyne-Detected Stimulated Photon Echo: Applications to Optical Dynamics in Solution," *Chemical Physics* 233 (1998): 287–309.

151. L. Valkunas, D. Abramavicius, and T. Mančal, *Molecular Excitation Dynamics and Relaxation* (Wiley-VCH, 2013).

152. S. Dilthey, S. Hahn, and G. Stock, "Approximate Calculation of Femtosecond Pump-Probe Spectra Monitoring Nonadiabatic Excited-State Dynamics," *Journal of Chemical Physics* 112 (2000): 4910–4922.

153. I. Uspenskiy, B. Strodel, and G. Stock, "Classical Calculation of Transient Absorption Spectra Monitoring Ultrafast Electron Transfer Processes," *Journal of Chemical Theory and Computation* 2 (2006): 1605–1617.

154. B. J. Schwartz and P. J. Rossky, "Pump-Probe Spectroscopy of the Hydrated Electron: A Quantum Molecular Dynamics Simulation," *Journal of Chemical Physics* 101 (1994): 6917–6926.

155. Z. Li, J.-Y. Fang, and C. C. Martens, "Simulation of Ultrafast Dynamics and Pump-Probe Spectroscopy Using Classical Trajectories," *Journal of Chemical Physics* 104 (1996): 6919–6929.

156. J. Che, W. Zhang, and Y. J. Yan, "A Classical Time-Frequency Theory of Transient Absorption Spectroscopy," *Journal of Chemical Physics* 106 (1997): 6947–6956.

157. L. W. Ungar and J. A. Cina, "Short-Time Fluorescence Stokes Shift Dynamics," *Advances in Chemical Physics* 100 (1997): 171–228.

158. V. A. Ermoshin and V. Engel, "Femtosecond Pump-Probe Fluorescence Signals From Classical Trajectories: Comparison With Wave-Packet Calculations," *European Physical Journal D: Atomic, Molecular, Optical and Plasma Physics* 15 (2001): 413–422.

159. A. Heidenreich and J. Jortner, "Pump-Probe Spectroscopy of Ultrafast Structural Relaxation of Electronically Excited Rare Gas Heteroclusters," *Journal of Electron Spectroscopy and Related Phenomena* 106 (2000): 187–197.

160. M. F. Gelin, X. Huang, W. Xie, L. Chen, N. Došlić, and W. Domcke, "Ab Initio Surface Hopping Simulation of Femtosecond Transient-Absorption Pump-Probe Signals of Nonadiabatic Excited-State Dynamics Using the Doorway-Window Representation," *Journal of Chemical Theory and Computation* 17 (2021): 2394–2408.

161. X. Huang, W. Xie, N. Došlić, M. F. Gelin, and W. Domcke, "Ab Initio Quasiclassical Simulation of Femtosecond Time-Resolved Two-Dimensional Electronic Spectra of Pyrazine," *Journal of Physical Chemistry Letters* 12 (2021): 11736–11744.

162. M. Lax, "The Franck-Condon Principle and Its Application to Crystals," *Journal of Chemical Physics* 20 (1952): 1752–1760.

163. M. Hillery, R. F. O'Connel, M. O. Scully, and E. P. Wigner, "Distribution Functions in Physics: Fundamentals," *Physics Reports* 106 (1984): 121–167.

164. M. Dantus, M. J. Rosker, and A. H. Zewail, "Femtosecond Real-Time Probing of Reactions. II. The Dissociation of ICN," *Journal of Chemical Physics* 89 (1988): 6128–6140.

165. T. S. Rose, M. J. Rosker, and A. H. Zewail, "Femtosecond Real-Time Probing of Reactions. IV. The Reactions of Alkali Halides," *Journal of Chemical Physics* 91 (1989): 7415–7436.

166. R. Bersohn and A. H. Zewail, "Time Dependent Absorption of Fragments During Dissociation," *Berichte der Bunsengesellschaft für Physikalische Chemie* 92 (1988): 373–378.

167. S.-Y. Lee, W. T. Pollard, and R. A. Mathies, "Classical Theory for Real-Time Femtosecond Probing of the NaI* Photodissociation," *Journal of Chemical Physics* 90 (1989): 6146–6150.

168. R. E. Walkup, J. A. Misewich, J. H. Glownia, and P. P. Sorokin, "Classical Model of Femtosecond Time-Resolved Absorption Spectra of Dissociating Molecules," *Journal of Chemical Physics* 94 (1991): 3389–3406.

169. Y. J. Yan and S. Mukamel, "Photo Echoes of Polyatomic Molecules in Condensed Phases," *Journal of Chemical Physics* 94 (1991): 179–190.

170. W. T. Pollard, S.-Y. Lee, and R. A. Mathies, "Wave Packet Theory of Dynamic Absorption Spectra in Femtosecond Pump-Probe Experiments," *Journal of Chemical Physics* 92 (1990): 4012–4029.

171. W. T. Pollard and R. A. Mathies, "Analysis of Femtosecond Dynamic Absorption Spectra of Nonstationary States," *Annual Review of Physical Chemistry* 43 (1992): 497–523.

172. T. J. Smith, L. W. Ungar, and J. A. Cina, "Resonant Short-Pulse Effects on Nuclear Motion in the Electronic Ground State," *Journal of Luminescence* 58 (1994): 66–73.

173. Y.-C. Shen and J. A. Cina, "What Can Short-Pulse Pump-Probe Spectroscopy Tell Us About Franck-Condon Dynamics?," *Journal of Chemical Physics* 110 (1999): 9793–9806.

174. S. A. Pentidis and R. F. Loring, "Calculation of Photon Echo With Mixed-State Propagation," *Chemical Physics Letters* 287 (1998): 217–223.

175. S. M. Gruenbaum and R. F. Loring, "Semiclassical Mean-Trajectory Approximation for Nonlinear Spectroscopic Response Functions," *Journal of Chemical Physics* 129 (2008): 124510.

176. G. Stock and W. H. Miller, "Classical Formulation of the Spectroscopy of Nonadiabatic Excited-State Dynamics," *Journal of Chemical Physics* 99 (1993): 1545–1555.

177. M. A. Selpulveda and S. Mukamel, "Semiclassical Theory of Molecular Nonlinear Polarization," *Journal of Chemical Physics* 102 (1995): 9327–9344.

178. P. L. McRobbie and E. Geva, "A Benchmark Study of Different Methods for Calculating One- and Two-Dimensional Optical Spectra," *Journal of Physical Chemistry A* 113 (2009): 10425–10434.

179. Q. Shi and E. Geva, "A Comparison Between Different Semiclassical Approximations for Optical Response Functions in Nonpolar Liquid Solutions," *Journal of Chemical Physics* 122 (2005): 064506.

180. F. Martínez, N. Rekik, and G. Hanna, "Simulation of Nonlinear Optical Signals via Approximate Solutions of the Quantum-Classical Liouville Equation: Application to the Pump-Probe Spectroscopy of a Condensed Phase Electron Transfer Reaction," *Chemical Physics Letters* 573 (2013): 77–83.

181. K. Polley and R. F. Loring, "Spectroscopic Response Theory With Classical Mapping Hamiltonians," *Journal of Chemical Physics* 153 (2020): 204103.

182. T. Begušić, J. Roulet, and J. Vaníček, "On-The-Fly Ab Initio Semiclassical Evaluation of Time-Resolved Electronic Spectra," *Journal of Chemical Physics* 149 (2018): 244115.

183. C. Xu, K. Lin, D. Hu, F. L. Gu, M. F. Gelin, and Z. Lan, "Ultrafast Internal Conversion Dynamics Through the On-The-Fly Simulation of Transient Absorption Pump–Probe Spectra With Different Electronic Structure Methods," *Journal of Physical Chemistry Letters* 13 (2021): 661–668.

184. G. Stock, R. Schneider, and W. Domcke, "Theoretical Studies on the Femtosecond Real-Time Measurement of Ultrafast Electronic Decay in Polyatomic Molecules," *Journal of Chemical Physics* 90 (1989): 7184–7194.

185. R. Schneider, W. Domcke, and H. Köppel, "Aspects of Dissipative Electronic and Vibrational Dynamics of Strongly Vibronically Coupled Systems," *Journal of Chemical Physics* 92 (1990): 1045–1061.

186. G. A. Worth, H. D. Meyer, and L. S. Cederbaum, "Relaxation of a System With a Conical Intersection Coupled to a Bath: A Benchmark 24-Dimensional Wave Packet Study Treating the Environment Explicitly," *Journal of Chemical Physics* 109 (1998): 3518–3529.

187. A. Raab, G. Worth, H.-D. Meyer, and L. S. Cederbaum, "Molecular Dynamics of Pyrazine After Excitation to the S_2 Electronic State Using a Realistic 24-Mode Model Hamiltonian," *Journal of Chemical Physics* 110 (1999): 936–946.

188. U. Werner, R. Mitrić, T. Suzuki, and V. Bonačić-Koutecký, "Nonadiabatic Dynamics Within the Time Dependent Density Functional Theory: Ultrafast Photodynamics of Pyrazine," *Chemical Physics* 349 (2008): 319–324.

189. M. Sala, B. Lasorne, F. Gatti, and S. Guerin, "The Role of the Low-Lying Dark nπ* States in the Photophysics of Pyrazine: A Quantum Dynamics Study," *Physical Chemistry Chemical Physics* 16 (2014): 15957–15967.

190. M. Sala, S. Guerin, and F. Gatti, "Quantum Dynamics of the Photostability of Pyrazine," *Physical Chemistry Chemical Physics* 17 (2015): 29518–29530.

191. L. Chen, M. F. Gelin, and W. Domcke, "Multimode Quantum Dynamics With Multiple Davydov D2 Trial States: Application to a 24-Dimensional Conical Intersection Model," *Journal of Chemical Physics* 150 (2019): 024101.

192. W. Xie, M. Sapunar, N. Došlić, M. Sala, and W. Domcke, "Assessing the Performance of Trajectory Surface Hopping Methods: Ultrafast Internal Conversion in Pyrazine," *Journal of Chemical Physics* 150 (2019): 154119.

193. K. Sun, W. Xie, L. Chen, W. Domcke, and M. F. Gelin, "Multi-Faceted Spectroscopic Mapping of Ultrafast Nondiabatic Dynamics Near Conical Intersections: A Computational Study," *Journal of Chemical Physics* 153 (2020): 174111.

194. T. Horio, R. Spesyvtsev, K. Nagashima, R. A. Ingle, Y. Suzuki, and T. Suzuki, "Full Observation of Ultrafast Cascaded Radiationless Transitions From $S_2(\pi\pi^*)$ State of Pyrazine Using Vacuum Ultraviolet Photoelectron Imaging," *Journal of Chemical Physics* 145 (2016): 044306.

195. J. Schirmer, "Beyond the Random-Phase Approximation: A New Approximation Scheme for the Polarization Propagator," *Physical Review A* 26 (1982): 2395–2416.

196. P. Cattaneo and M. Persico, "Semiclassical Simulations of Azomethane Photochemistry in the Gas Phase and in Solution," *Journal of the American Chemical Society* 123 (2001): 7638–7645.

197. E. W.-G. Diau and A. H. Zewail, "Femtochemistry of Trans-Azomethane: A Combined Experimental and Theoretical Study," *ChemPhysChem* 4 (2003): 445–446.

198. B. Sellner, M. Ruckenbauer, I. Stambolić, M. Barbatti, A. J. Aquino, and H. Lischka, "Photodynamics of Azomethane: A Nonadiabatic Surface-Hopping Study," *Journal of Physical Chemistry A* 114 (2010): 8778–8785.

199. P. G. Szalay, A. J. Aquino, M. Barbatti, and H. Lischka, "Theoretical Study of the Excitation Spectrum of Azomethane," *Chemical Physics* 380 (2011): 9–16.

200. A. Gaenko, A. DeFusco, S. A. Varganov, T. J. Martínez, and M. S. Gordon, "Interfacing the Ab Initio Multiple Spawning Method With Electronic Structure Methods in GAMESS: Photodecay of Transazomethane," *Journal of Physical Chemistry A* 118 (2014): 10902–10908.

201. T. Shiozaki, W. Gyorffy, P. Celani, and H.-J. Werner, "Extended Multi-State Complete Active Space Second-Order Perturbation Theory: Energy and Nuclear Gradients," *Journal of Chemical Physics* 135 (2011): 081106.

202. S. Raychaudhuri, Y. Shapir, V. V. Chernyak, and S. Mukamel, "Excitonic Funneling in Extended Dendrimers With Nonlinear and Random Potentials," *Physical Review Letters* 85 (2000): 282–285.

203. A. Tortschanoff and S. Mukamel, "Pump-Probe Simulation Study of the Two-Exciton Manifold of Dendrimers," *Journal of Physical Chemistry A* 106 (2002): 7521–7529.

204. E. Atas, Z. Peng, and V. D. Kleiman, "Energy Transfer in Unsymmetrical Phenylene Ethynylene Dendrimers," *Journal of Physical Chemistry B* 109 (2005): 13553–13560.

205. S. Fernandez-Alberti, A. E. Roitberg, V. D. Kleiman, T. Nelson, and S. Tretiak, "Shishiodoshi Unidirectional Energy Transfer Mechanism in Phenylene Ethynylene Dendrimers," *Journal of Chemical Physics* 137 (2012): 22A526.

206. V. M. Freixas, D. Ondarse-Alvarez, S. Tretiak, D. V. Makhov, D. V. Shalashilin, and S. Fernandez-Alberti, "Photoinduced Non-Adiabatic Energy Transfer Pathways in Dendrimer Building Blocks," *Journal of Chemical Physics* 150 (2019): 124301.

207. D. Hu, J. Peng, L. Chen, M. F. Gelin, and Z. Lan, "Spectral Fingerprint of Excited-State Energy Transfer in Dendrimers Through Polarization-Sensitive Transient-Absorption Pump–Probe Signals: On-The-Fly Nonadiabatic Dynamics Simulations," *Journal of Physical Chemistry Letters* 12 (2021): 9710–9719.

208. S. Fernandez-Alberti, V. D. Kleiman, S. Tretiak, and A. E. Roitberg, "Nonadiabatic Molecular Dynamics Simulations of the Energy Transfer Between Building Blocks in a Phenylene Ethynylene Dendrimer," *Journal of Physical Chemistry A* 113 (2009): 7535–7542.

209. S. Fernandez-Alberti, D. V. Makhov, S. Tretiak, and D. V. Shalashilin, "Non-Adiabatic Excited State Molecular Dynamics of Phenylene Ethynylene Dendrimer Using a Multiconfigurational Ehrenfest Approach," *Physical Chemistry Chemical Physics* 18 (2016): 10028–10040.

210. M. Chergui, "Time-Resolved X-Ray Spectroscopies of Chemical Systems: New Perspectives," *Structural Dynamics* 3 (2016): 031001.

211. Y. Pertot, C. Schmidt, M. Matthews, et al., "Time-Resolved X-Ray Absorption Spectroscopy With a Water Window High-Harmonic Source," *Science* 355 (2017): 264–267.

212. L. Young, K. Ueda, M. Gühr, et al., "Roadmap of Ultrafast X-Ray Atomic and Molecular Physics," *Journal of Physics B: Atomic, Molecular and Optical Physics* 51 (2018): 032003.

213. L. S. Cederbaum, W. Domcke, and J. Schirmer, "Many-Body Theory of Core Holes," *Physical Review A* 22 (1980): 206–222.

214. J. Wenzel and A. Dreuw, "Calculating Core-Level Excitations and X-Ray Absorption Spectra of Medium-Sized Closed-Shell Molecules With the Algebraic-Diagrammatic Construction Scheme for the Polarization Propagator," *Journal of Computational Chemistry* 35 (2014): 1900–1915.

215. M. L. Vidal, X. Feng, E. Epifanovsky, A. I. Krylov, and S. Coriani, "New and Efficient Equation-Of-Motion Coupled-Cluster Framework for Core-Excited and Core-Ionized States," *Journal of Chemical Theory and Computation* 15 (2019): 3117–3133.

216. P. Norman and A. Dreuw, "Simulating X-Ray Spectroscopies and Calculating Core-Excited States of Molecules," *Chemical Reviews* 118 (2018): 7208–7248.

217. S. Tsuru, M. L. Vidal, M. Papai, A. I. Krylov, K. B. Moller, and S. Coriani, "An Assessment of Different Electronic Structure Approaches for Modeling Time-Resolved X-Ray Absorption Spectroscopy," *Structural Dynamics* 8 (2021): 024101.

218. R. C. Couto, L. Kjellson, H. Agren, et al., "The Carbon and Oxygen K-Edge NEXAFS Spectra of CO^+," *Physical Chemistry Chemical Physics* 22 (2020): 16215–16223.

219. K. Bennett, Y. Zhang, M. Kowalewski, W. Hua, and S. Mukamel, "Multidimensional Resonant Nonlinear Spectroscopy With Coherent Broadband X-Ray Pulses," *Physica Scripta* T169 (2016): 014002.

220. D. Keefer, S. M. Cavaletto, J. R. Rouxel, M. Garavelli, H. Yong, and S. Mukamel, "Ultrafast X-Ray Probes of Elementary Molecular Events," *Annual Review of Physical Chemistry* 74 (2023): 73–97.

221. M. Kowalewski, K. Bennett, K. E. Dorfman, and S. Mukamel, "Catching Conical Intersections in the Act: Monitoring Transient Electronic Coherences by Attosecond Stimulated X-Ray Raman Signals," *Physical Review Letters* 115 (2015): 193003.

222. D. Keefer, T. Schnappinger, R. de Vivie-Riedle, and S. Mukamel, "Visualizing Conical Intersection Passages via Vibronic Coherence Maps Generated by Stimulated Ultrafast X-Ray Raman Signals," *Proceedings of the National Academy of Sciences of the USA* 117 (2020): 24069–24075.

223. Y. Nam, D. Keefer, A. Nenov, et al., "Conical Intersection Passages of Molecules Probed by X-Ray Diffraction and Stimulated Raman Spectroscopy," *Journal of Physical Chemistry Letters* 12 (2021): 300–309.

224. D. Jadoun, M. Gudem, and M. Kowalewski, "Capturing Fingerprints of Conical Intersection: Complementary Information of Non-Adiabatic Dynamics From Linear X-Ray Probes," *Structural Dynamics* 8 (2021): 034101.

225. Y. Nam, F. Montorsi, D. Keefer, et al., "Time-Resolved Optical Pump-Resonant X-Ray Probe Spectroscopy of 4-Thiouracil: A Simulation Study," *Journal of Chemical Theory and Computation* 18 (2022): 3075–3088.

226. A. Freibert, D. Mendive-Tapi, N. Huse, and O. Vendrell, "Femtosecond X-Ray Absorption Spectroscopy of Pyrazine at the Nitrogen K-Edge: On the Validity of the Lorentzian Limit," *Journal of Physics B: Atomic, Molecular and Optical Physics* 54 (2021): 244003.

227. A. Freibert, D. Mendive-Tapi, N. Huse, and O. Vendrell, "Time-Dependent Resonant Inelastic X-Ray Scattering of Pyrazine at the Nitrogen K-Edge: A Quantum Dynamics Approach," *Journal of Chemical Theory and Computation* 20 (2024): 2167–2180.

228. A. Freibert, D. Mendive-Tapi, O. Vendrell, and N. Huse, "A Fully Dynamical Description of Time-Resolved Resonant Inelastic X-Ray Scattering of Pyrazine," *Physical Chemistry Chemical Physics* 26 (2024): 572.

229. F. Segatta, A. Nenov, S. Orlandi, A. Arcioni, S. Mukamel, and M. Garavelli, "Exploring the Capabilities of Optical Pump X-Ray Probe NEXAFS Spectroscopy to Track Photoinduced Dynamics Mediated by Conical Intersections," *Faraday Discussions* 221 (2020): 245–264.

230. W. Hua, S. Mukamel, and Y. Luo, "Transient X-Ray Absorption Spectral Fingerprints of the S_1 Dark State in Uracil," *Journal of Physical Chemistry Letters* 10 (2019): 7172–7178.

231. H. Wang, M. Odelius, and D. Prendergast, "A Combined Multi-Reference Pump-Probe Simulation Method With Application to XUV Signatures of Ultrafast Methyl Iodide Photodissociation," *Journal of Chemical Physics* 151 (2019): 124106.

232. K. F. Chang, H. Wang, S. M. Poullain, D. Prendergast, D. M. Neumark, and S. R. Leone, "Mapping Wave Packet Bifurcation at a Conical Intersection in CH_3I by Attosecond XUV Transient Absorption Spectroscopy," *Journal of Chemical Physics* 154 (2021): 234301.

233. N. H. List, A. L. Dempwolff, A. Dreuw, P. Norman, and T. J. Martínez, "Probing Competing Relaxation Pathways in Malonaldehyde With Transient X-Ray Absorption Spectroscopy," *Chemical Science* 11 (2020): 4180–4193.

234. K. S. Zinchenko, F. Ardana-Lamas, I. Seidu, et al., "Sub-7-Fs Conical-Intersection Dynamics Probed at the Carbon K-Edge," *Science* 371 (2021): 489–494.

235. S. P. Neville, V. Averbuk, S. Patchkovskii, et al., "Beyond Structure: Ultrafast X-Ray Absorption Spectroscopy as a Probe of Non-Adiabatic Wavepacket Dynamics," *Faraday Discussions* 194 (2016): 117–145.

236. S. P. Neville, M. Chergui, A. Stolow, and M. S. Schuurman, "Ultrafast X-Ray Spectroscopy of Conical Intersections," *Physical Review Letters* 120 (2018): 243001.

237. T. Northey, J. Duffield, and T. J. Penfold, "Non-Equilibrium X-Ray Spectroscopy Using Direct Quantum Dynamics," *Journal of Chemical Physics* 149 (2018): 124107.

238. T. Northey, J. Norell, A. E. A. Fouda, N. A. Besley, M. Odelius, and T. J. Penfold, "Ultrafast Nonadiabatic Dynamics Probed by Nitrogen K-Edge Absorption Spectroscopy," *Physical Chemistry Chemical Physics* 22 (2020): 2667–2676.

239. S. Tsuru, M. L. Vidal, M. Papai, A. I. Krylov, K. B. Moller, and S. Coriani, "Time-Resolved Near-Edge X-Ray Absorption Fine Structure of Pyrazine From Electronic Structure and Nuclear Wave Packet Dynamics Simulations," *Journal of Chemical Physics* 151 (2019): 124114.

240. J. F. Stanton and J. A. Gauss, "Simple Scheme for the Direct Calculation of Ionization Potentials With Coupled-Cluster Theory That Exploits Established Excitation Energy Methods," *Journal of Chemical Physics* 111 (1999): 8785–8788.

241. T. Kaczun, A. L. Dempwolff, X. Huang, M. F. Gelin, W. Domcke, and A. Dreuw, "Tuning UV Pump X-Ray Probe Spectroscopy on the Nitrogen K Edge Reveals the Radiationless Relaxation of Pyrazine: Ab Initio Simulations Using the Quasiclassical Doorway-Window Approximation," *Journal of Physical Chemistry Letters* 14 (2023): 5648–5656.

242. V. Scutelnic, S. Tsuru, M. Papai, et al., "X-Ray Transient Absorption Reveals the $^1A_u(n\pi^*)$ State of Pyrazine in Electronic Relaxation," *Nature Communications* 12 (2021): 5003.

243. J. D. Hybl, A. A. Ferro, and D. M. Jonas, "Two-Dimensional Fourier Transform Electronic Spectroscopy," *Journal of Chemical Physics* 115 (2001): 6606–6622.

244. D. M. Jonas, "Optical Analogs of 2D NMR," *Science* 300 (2003): 1515–1517.

245. M. Cho, "Coherent Two-Dimensional Optical Spectroscopy," *Chemical Reviews* 108 (2008): 1331–1418.

246. F. Milota, J. Sperling, A. Nemeth, T. Mančal, and H. F. Kaufmann, "Two-Dimensional Electronic Spectroscopy of Molecular Excitons," *Accounts of Chemical Research* 42 (2009): 1364–1374.

247. S. Tretiak and S. Mukamel, "Density Matrix Analysis and Simulation of Electronic Excitations in Conjugated and Aggregated Molecules," *Chemical Reviews* 102 (2002): 3171–3212.

248. M. Schröter, S. D. Ivanov, J. Schulze, S. P. Polyutov, Y. Yan, and D. Pullerits, "Exciton-Vibrational Coupling in the Dynamics and Spectroscopy of Frenkel Excitons in Molecular Aggregates," *Physics Reports* 567 (2015): 1–78.

249. N. J. Hestand and F. C. Spano, "Expanded Theory of H- and J-Molecular Aggregates: The Effects of Vibronic Coupling and Intermolecular Charge Transfer," *Chemical Reviews* 118 (2018): 7069–7163.

250. T. Renger, V. May, and O. Kühn, "Ultrafast Excitation Energy Transfer Dynamics in Photosynthetic Pigment-Protein Complexes," *Physics Reports* 343 (2001): 137–254.

251. N. S. Ginsberg, Y.-C. Cheng, and G. R. Fleming, "Two-Dimensional Electronic Spectroscopy of Molecular Aggregates," *Accounts of Chemical Research* 42 (2009): 1352–1363.

252. Y.-C. Cheng and G. R. Fleming, "Dynamics of Light Harvesting in Photosynthesis," *Annual Review of Physical Chemistry* 60 (2009): 241–262.

253. T. Mirkovic, E. E. Ostroumov, J. M. Anna, R. van Grondelle, and S. G. D. Govindjee, "Light Absorption and Energy Transfer in the Antenna Complexes of Photosynthetic Organisms," *Chemical Reviews* 117 (2017): 249–293.

254. G. S. Engel, T. R. Calhoun, E. L. Read, et al., "Evidence of Wavelike Energy Transfer Through Quantum Coherence in Photosynthetic Systems," *Nature* 446 (2007): 782–786.

255. H.-G. Duan, V. I. Prokhorenko, R. J. Cogdell, et al., "Nature Does Not Rely on Long-Lived Electronic Quantum Coherence for Photosynthetic Energy Transfer," *Proceedings of the National Academy of Sciences of the USA* 114 (2017): 8493–8498.

256. J. Cao, R. J. Cogdell, D. F. Coker, et al., "Quantum Biology Revisited," *Science Advances* 6 (2020): eaaz4888.

257. S. Mueller, S. Draeger, X. Ma, et al., "Fluorescence-Detected Two-Quantum and One-Quantum-Two-Quantum 2D Electronic Spectroscopy," *Journal of Physical Chemistry Letters* 9 (2018): 1964–1969.

258. P. Maly, J. Lüttig, P. A. Rose, et al., "Separating Single- From Multi-Particle Dynamics in Nonlinear Spectroscopy," *Nature* 616 (2023): 280–287.

259. K.-W. Sun, M. F. Gelin, V. Y. Chernyak, and Y. Zhao, "Davydov Ansatz as an Efficient Tool for the Simulation of Nonlinear Optical Response of Molecular Aggregates," *Journal of Chemical Physics* 142 (2015): 212448.

260. P. Maly, O. J. G. Somsen, V. I. Novoderezhkin, T. Mančal, and R. van Grondelle, "The Role of Resonant Vibrations in Electronic Energy Transfer," *ChemPhysChem* 17 (2016): 1356–1368.

261. Y. Yao, K.-W. Sun, Z. Luo, and H. Ma, "Full Quantum Dynamics Simulation of a Realistic Molecular System Using the Adaptive Time-Dependent Density Matrix Renormalization Group Method," *Journal of Physical Chemistry Letters* 9 (2018): 413–419.

262. T. Jiang, W. Li, L. Ren, and Z. Shuai, "Finite Temperature Dynamical Density Matrix Renormalization Group for Spectroscopy in Frequency Domain," *Journal of Physical Chemistry Letters* 11 (2020): 3761–3768.

263. A. Ishizaki and Y. Tanimura, "Quantum Dynamics of Systems Strongly Coupled to Lowtemperature Colored Noise Bath: Reduced Hierarchy Equations Approach," *Journal of the Physical Society of Japan* 74 (2005): 3131–3134.

264. Y. Tanimura, "Numerically 'Exact' Approach to Open Quantum Dynamics: The Hierarchical Equations of Motion (HEOM)," *Journal of Chemical Physics* 153 (2020): 020901.

265. J. Provazza, F. Segatta, M. Garavelli, and D. F. Coker, "Semiclassical Path Integral Calculation of Nonlinear Optical Spectroscopy," *Journal of Chemical Theory and Computation* 14 (2018): 856–866.

266. K. Polley and R. F. Loring, "Two-Dimensional Vibronic Spectra From Classical Trajectories," *Journal of Chemical Physics* 150 (2019): 164114.

267. C. P. van der Vegte, A. G. Dijkstra, J. Knoester, and T. L. C. Jansen, "Calculating Two-Dimensional Spectra With the Mixed Quantum-Classical Ehrenfest Method," *Journal of Physical Chemistry A* 117 (2013): 5970–5980.

268. R. Tempelaar, C. P. van der Vegte, J. Knoester, and T. L. C. Jansen, "Surface Hopping Modeling of Two-Dimensional Spectra," *Journal of Chemical Physics* 138 (2013): 164106.

269. A. Jain, A. S. Petit, J. M. Anna, and J. E. Subotnik, "Simple and Efficient Theoretical Approach to Compute 2D Optical Spectra," *Journal of Physical Chemistry B* 123 (2019): 1602–1617.

270. M. Richter and B. P. Fingerhut, "Simulation of Multi-Dimensional Signals in the Optical Domain: Quantum-Classical Feedback in Nonlinear Exciton Propagation," *Journal of Chemical Theory and Computation* 12 (2016): 3284–3294.

271. X. Leng, S. Yue, Y.-X. Weng, K. Song, and Q. Shi, "Effects of Finite Laser Pulse Width on Two-Dimensional Electronic Spectroscopy," *Chemical Physics Letters* 667 (2017): 79–86.

272. X. Leng, Y.-M. Yan, D.-R. Zhu, K. Song, Y.-X. Weng, and Q. Shi, "Simulation of the Two-Dimensional Electronic Spectroscopy and Energy Transfer Dynamics of Light-Harvesting Complex II at Ambient Temperature," *Journal of Physical Chemistry B* 122 (2018): 4642–4652.

273. X. Leng, T. H. Do, P. Akhtar, H. L. Nguyen, P. H. Lambrev, and H. S. Tan, "Hierarchical Equations of Motion Simulation of Temperature-Dependent Two-Dimensional Electronic Spectroscopy of the Chlorophyll a Manifold in LHCII," *Chemistry, an Asian Journal* 15 (2020): 1996–2004.

274. X. Gao and E. Geva, "A Nonperturbative Methodology for Simulating Multidimensional Spectra of Multiexcitonic Molecular Systems via Quasiclassical Mapping Hamiltonian Methods," *Journal of Chemical Theory and Computation* 16 (2020): 6491–6502.

275. Y. Yan, Y. Liu, Y. Xing, and Q. Shi, "Theoretical Study of Excitation Energy Transfer and Nonlinear Spectroscopy of Photosynthetic Light-Harvesting Complexes Using the Nonperturbative Reduced Dynamics Method," *WIREs Computational Molecular Science* 11 (2020): e1498.

276. C.-h. Tseng, S. Matsika, and T. C. Weinacht, "Two-Dimensional Ultrafast Fourier Transform Spectroscopy in the Deep Ultraviolet," *Optics Express* 17 (2009): 18788–18793.

277. U. Selig, C.-F. Schleussner, M. Foerster, F. Langhojer, P. Nuernberger, and T. Brixner, "Coherent Two-Dimensional Ultraviolet Spectroscopy in Fully Noncollinear Geometry," *Optics Letters* 35 (2010): 4178–4180.

278. B. A. West and A. M. Moran, "Two-Dimensional Electronic Spectroscopy in the Ultraviolet Wavelength Range," *Journal of Physical Chemistry Letters* 3 (2012): 2575–2581.

279. N. Krebs, I. Pugliesi, J. Hauer, and E. Riedle, "Two-Dimensional Fourier Transform Spectroscopy in the Ultraviolet With Sub-20 fs Pump Pulses and 250–720 nm Supercontinuum Probe," *New Journal of Physics* 15 (2013): 085016.

280. B. A. West, B. P. Molesky, P. G. Giokas, and A. M. Moran, "Uncovering Molecular Relaxation Processes With Nonlinear Spectroscopies in the Deep UV," *Chemical Physics* 423 (2013): 92–104.

281. B. A. West, J. M. Womick, and A. M. Moran, "Probing Ultrafast Dynamics in Adenine With Mid-UV Four-Wave Mixing Spectroscopies," *Journal of Physical Chemistry A* 115 (2011): 8630–8637.

282. C.-h. Tseng, P. Sandor, M. Kotur, T. C. Weinacht, and S. Matsika, "Two-Dimensional Fourier Transform Spectroscopy of Adenine and Uracil Using Shaped Ultrafast Laser Pulses in the Deep UV," *Journal of Physical Chemistry A* 116 (2012): 2654–2661.

283. V. I. Prokhorenko, A. Picchiotti, M. Pola, A. G. Dijkstra, and R. J. D. Miller, "New Insights Into the Photophysics of DNA Nucleobases," *Journal of Physical Chemistry Letters* 7 (2016): 4445–4450.

284. A. Picchiotti, A. Nenov, A. Giussani, et al., "Pyrene, a Test Case for Deep-Ultraviolet Molecular Photophysics," *Journal of Physical Chemistry Letters* 10 (2019): 3481–3487.

285. M. Kullmann, S. Ruetzelo, J. Buback, P. Nuernberger, and T. Brixner, "Reaction Dynamics of a Molecular Switch Unveiled by Coherent Two-Dimensional Electronic Spectroscopy," *Journal of the American Chemical Society* 133 (2011): 13074–13080.

286. P. Nuernberger, S. Ruetzel, and T. Brixner, "Multidimensional Electronic Spectroscopy of Photochemical Reactions," *Angewandte Chemie, International Edition* 54 (2015): 11368–11386.

287. J. Segarra-Marti, S. Mukamel, M. Garavelli, A. Nenov, and I. Rivalta, "Towards Accurate Simulation of Two-Dimensional Electronic Spectra," *Topics in Current Chemistry* 376 (2018): 24.

288. I. Rivalta, A. Nenov, G. Cerullo, S. Mukamel, and M. Garavelli, "Ab Initio Simulations of Two-Dimensional Electronic Spectra: The SOS// QM/MM Approach," *International Journal of Quantum Chemistry* 114 (2014): 85–93.

289. I. Rivalta, A. Nenov, O. Weingart, G. Cerullo, M. Garavelli, and S. Mukamel, "Modelling Time-Resolved Two-Dimensional Electronic Spectroscopy of the Primary Photoisomerization Event in Rhodopsin," *Journal of Physical Chemistry A* 118 (2014): 8396–8405.

290. A. Nenov, A. Giussani, B. P. Fingerhut, et al., "Spectral Lineshapes in Nonlinear Electronic Spectroscopy," *Physical Chemistry Chemical Physics* 17 (2015): 30925–30936.

291. A. Nenov, S. Mukamel, M. Garavelli, and I. Rivalta, "Two-Dimensional Electronic Spectroscopy of Benzene, Phenol, and Their Dimer: An Efficient First-Principles Simulation Protocol," *Journal of Chemical Theory and Computation* 11 (2015): 3755–3771.

292. A. Nenov, J. Segarra-Marti, A. Giussani, et al., "Probing Deactivation Pathways of DNA Nucleobases by Two-Dimensional Electronic Spectroscopy: First Principles Simulations," *Faraday Discussions* 177 (2015): 345–362.

293. J. Segarra-Marti, F. Segatta, T. A. Mackenzie, et al., "Modeling Multidimensional Spectral Lineshapes From First Principles: Application to Water-Solvated Adenine," *Faraday Discussions* 221 (2020): 219–244.

294. T. Begušić and J. Vaníček, "Finite-Temperature, Anharmonicity and Duschinsky Effects on the Two-Dimensional Electronic Spectra From Ab Initio Thermo-Field Gaussian Wavepacket Dynamics," *Journal of Physical Chemistry Letters* 12 (2021): 2997–3005.

295. C. Woywod, W. Domcke, A. L. Sobolewski, and H.-J. Werner, "Characterization of the S_1-S_2 Conical Intersection in Pyrazine Using Ab Initio Multiconfiguration Self-Consistent-Field and Multireference Configuration-Interaction Methods," *Journal of Chemical Physics* 100 (1994): 1400–1413.

296. M. T. Zanni, T. R. Taylor, B. J. Greenblatt, B. Soep, and D. M. Neumark, "Characterization of the I^-_2 Anion Ground State Using Conventional and Femtosecond Photoelectron Spectroscopy," *Journal of Chemical Physics* 107 (1997): 7613–7619.

297. E. Charron and A. Suzor-Weiner, "Femtosecond Dynamics of NaI Ionization and Dissociative Ionization," *Journal of Chemical Physics* 108 (1998): 3922–3931.

298. S. C. Althorpe and T. Seideman, "Molecular Alignment From Femtosecond Time-Resolved Photoelectron Angular Distributions: Nonperturbative Calculations on NO," *Journal of Chemical Physics* 110 (1999): 147–155.

299. T. Seideman, "Time-Resolved Photoelectron Angular Distributions as a Means of Studying Polyatomic Nonadiabatic Dynamics," *Journal of Chemical Physics* 113 (2000): 1677–1680.

300. Y. Arasaki, K. Takatsuka, K. Wang, and V. McKoy, "Femtosecond Energy and Angle-Resolved Photoelectron Spectroscopy," *Journal of Chemical Physics* 112 (2000): 8871–8884.

301. Y. Arasaki, K. Takatsuka, K. Wang, and V. McKoy, "Studies of Electron Transfer in NaI With Pump-Probe Femtosecond Photoelectron Spectroscopy," *Journal of Chemical Physics* 119 (2003): 7913–7923.

302. V. Blanchet, S. Lochbrunner, M. Schmitt, et al., "Towards Disentangling Coupled Electronic-Vibrational Dynamics in Ultrafast Non-Adiabatic Processes," *Faraday Discussions* 115 (2000): 33–48.

303. A. Stolow, "Femtosecond Time-Resolved Photoelectron Spectroscopy of Polyatomic Molecules," *Annual Review of Physical Chemistry* 54 (2003): 89–119.

304. T. Suzuki, "Spiers Memorial Lecture: Introduction to Ultrafast Spectroscopy and Imaging of Photochemical Reactions," *Faraday Discussions* 228 (2021): 11–38.

305. C. Meier and V. Engel, "Time-Resolved Photoelectron Spectroscopy of Molecular Photodissociation: Classical Trajectory Versus Quantum Wave-Packet Calculations," *Physical Chemistry Chemical Physics* 4 (2002): 5014–5019.

306. V. S. Batista, M. T. Zanni, B. J. Greenblatt, D. M. Neumark, and W. H. Miller, "Femtosecond Photoelectron Spectroscopy of the I^-_2 Anion: A Semiclassical Molecular Dynamics Simulation Method," *Journal of Chemical Physics* 110 (1999): 3736–3747.

307. J. Stanzel, F. Burmeister, M. Neeb, et al., "Size-Dependent Dynamics in Excited States of Gold Clusters: From Oscillatory Motion to Photoinduced Melting," *Journal of Chemical Physics* 127 (2007): 164312.

308. R. Mitrić, U. Werner, and V. Bonačić-Koutecký, "Nonadiabatic Dynamics and Simulation of Time Resolved Photoelectron Spectra Within Time-Dependent Density Functional Theory: Ultrafast Photoswitching in Benzylideneaniline," *Journal of Chemical Physics* 129 (2008): 164118.

309. U. Werner, R. Mitrić, and V. Bonačić-Koutecký, "Simulation of Time Resolved Photoelectron Spectra With Stieltjes Imaging Illustrated on Ultrafast Internal Conversion in Pyrazine," *Journal of Chemical Physics* 132 (2010): 174301.

310. R. Mitrić, J. Petersen, M. Wohlgemuth, et al., "Time-Resolved Femtosecond Photoelectron Spectroscopy by Field-Induced Surface Hopping," *Journal of Physical Chemistry* A 115 (2010): 3755–3765.

311. A. Humeniuk, M. Wohlgemuth, T. Suzuki, and R. Mitrić, "Time-Resolved Photoelectron Imaging Spectra From Non-Adiabatic Molecular Dynamics Simulations," *Journal of Chemical Physics* 139 (2013): 134104.

312. G. Tomasello, A. Humeniuk, and R. Mitrić, "Exploring Ultrafast Dynamics of Pyrazine by Time-Resolved Photoelectron Imaging," *Journal of Physical Chemistry A* 118 (2014): 8437–8445.

313. H. R. Hudock, B. G. Levine, A. L. Thompson, et al., "Ab Initio Molecular Dynamics and Time-Resolved Photoelectron Spectroscopy of Electronically Excited Uracil and Thymine," *Journal of Physical Chemistry A* 111 (2007): 8500–8508.

314. K. Bennett, M. Kowalewski, and S. Mukamel, "Probing Electronic and Vibrational Dynamics in Molecules by Time-Resolved

Photoelectron and Auger-Electron and and X-Ray Photon Scattering Spectroscopy," *Faraday Discussions* 177 (2015): 405–428.

315. A. L. Thompson and T. J. Martínez, "Time-Resolved Photoelectron Spectroscopy From First Principles: Excited State Dynamics of Benzene," *Faraday Discussions* 150 (2011): 293–311.

316. H. Tao, T. K. Allison, T. W. Wright, et al., "Ultrafast Internal Conversion in Ethylene. I. The Excited State Lifetime," *Journal of Chemical Physics* 134 (2011): 244306.

317. T. J. A. Wolf, T. S. Kuhlman, O. Schalk, et al., "Hexamethylcyclopentadiene: Time-Resolved Photoelectron Spectroscopy and Ab Initio Multiple Spawning Simulations," *Physical Chemistry Chemical Physics* 16 (2014): 11770–11779.

318. R. J. MacDonell, O. Schalk, T. Geng, et al., "Excited-State Dynamics of Acrylonitrile: Substituent Effects at Conical Intersections Interrogated via Time-Resolved Photoelectron Spectroscopy and Ab Initio Simulation," *Journal of Chemical Physics* 145 (2016): 114306.

319. H. Ren, B. P. Fingerhut, and S. Mukamel, "Time Resolved Photoelectron Spectroscopy of Thioflavin T Photoisomerization: A Simulation Study," *Journal of Physical Chemistry A* 117 (2013): 6096–6104.

320. M. Ruckenbauer, S. Mai, P. Marquetand, and L. González, "Revealing Deactivation Pathways Hidden in Time-Resolved Photoelectron Spectra," *Scientific Reports* 6 (2016): 35522.

321. Y. Liu, P. Chakraborty, S. Matsika, and T. Weinacht, "Excited State Dynamics of Cis,Cis-1,3-Cyclooctadiene: UV Pump VUV Probe Time-Resolved Photoelectron Spectroscopy," *Journal of Chemical Physics* 153 (2020): 074301.

322. P. Chakraborty, Y. Liu, S. McClung, T. Weinacht, and S. Matsika, "Time Resolved Photoelectron Spectroscopy as a Test of Electronic Structure and Nonadiabatic Dynamics," *Journal of Physical Chemistry Letters* 12 (2021): 5099–5104.

323. W. Arbelo-Gonzalez, R. Crespo-Otero, and M. Barbatti, "Steady and Time-Resolved Photoelectron Spectra Based on Nuclear Ensembles," *Journal of Chemical Theory and Computation* 12 (2016): 5037–5049.

324. V. Bonačić-Koutecký and R. Mitrić, "Theoretical Exploration of Ultrafast Dynamics in Atomic Clusters: Analysis and Control," *Chemical Reviews* 105 (2005): 11–65.

325. S. Rahav and S. Mukamel, "Multidimensional Attosecond Photoelectron Spectroscopy With Shaped Pulses and Quantum Optical Fields," *Physical Review A* 81 (2010): 063810.

326. S. N. Dixit and V. McKoy, "Theory of Resonantly Enhanced Multiphoton Processes in Molecules," *Journal of Chemical Physics* 82 (1985): 3546–3553.

327. K. L. Reid, D. J. Leahy, and R. N. Zare, "Effect of Breaking Cylindrical Symmetry on Photoelectron Angular Distributions Resulting From Resonance-Enhanced Two-Photon Ionization," *Journal of Chemical Physics* 95 (1991): 1746–1756.

328. P. G. Burke, *R-Matrix Theory of Atomic Collisions: Application to Atomic, Molecular and Optical Processes* (Springer, 2011).

329. R. Schinke, *Photodissociation Dynamics* (Cambridge University Press, 1993).

330. A. Ponzi, C. Angeli, R. Cimiraglia, S. Coriani, and P. Decleva, "Dynamical Photoionization Observables of the CS Molecule: The Role of Electron Correlation," *Journal of Chemical Physics* 140 (2014): 204304.

331. A. Ponzi, M. Sapunar, C. Angeli, R. Cimiraglia, N. Došlić, and P. Decleva, "Photoionization of Furan From the Ground and Excited Electronic States," *Journal of Chemical Physics* 144 (2016): 084307.

332. C. M. Oana and A. I. Krylov, "Dyson Orbitals for Ionization From the Ground and Electronically Excited States Within Equation-Of-Motion Coupled-Cluster Formalism: Theory, Implementation, and Examples," *Journal of Chemical Physics* 127 (2007): 234410.

333. C. M. Oana and A. I. Krylov, "Cross Sections and Photoelectron Angular Distributions in Photodetachment From Negative Ions Using Equation-Of-Motion Coupled-Cluster Dyson Orbitals," *Journal of Chemical Physics* 131 (2009): 124114.

334. S. Gozem, A. O. Gunina, T. Ichino, D. L. Osborn, J. F. Stanton, and A. I. Krylov, "Photoelectron Wave Function in Photoionization: Plane Wave or Coulomb Wave?," *Journal of Physical Chemistry Letters* 6 (2015): 4532–4540.

335. T. Moitra, A. Ponzi, H. Koch, S. Coriani, and P. Decleva, "Accurate Description of Photoionization Dynamical Parameters," *Journal of Physical Chemistry Letters* 11 (2020): 5330–5337.

336. T. Piteša, M. Sapunar, A. Ponzi, et al., "Combined Surface-Hopping, Dyson Orbital, and B-Spline Approach for the Computation of Time-Resolved Photoelectron Spectroscopy Signals: The Internal Conversion in Pyrazine," *Journal of Chemical Theory and Computation* 17 (2021): 5098–5109.

337. H. Bachau, E. Cormier, P. Decleva, J. E. Hansen, and F. Martín, "Applications of B-Splines in Atomic and Molecular Physics," *Reports on Progress in Physics* 64 (2001): 1815–1943.

338. D. Toffoli, M. Stener, G. Fronzoni, and P. Decleva, "Convergence of the Multicenter B-Spline DFT Approach for the Continuum," *Chemical Physics* 276 (2002): 25–43.

339. R. R. Lucchese, K. Takatsuka, and V. McKoy, "Applications of the Schwinger Variational Principle to Electron-Molecule Collisions and Molecular Photoionization," *Physics Reports* 131 (1986): 147–221.

340. P. Descouvemont and D. Baye, "The R-Matrix Theory," *Reports on Progress in Physics* 73 (2010): 036301.

341. C. Froese Fischer and M. Idrees, "Spline Algorithms for Continuum Functions," *Computers in Physics* 3 (1989): 53–58.

342. M. Brosolo and P. Decleva, "Variational Approach to Continuum Orbitals in a Spline Basis: An Application to H_2^+ Photoionization," *Chemical Physics* 159 (1992): 185–196.

343. C. Marante, M. Klinker, I. Corral, J. González-Vázquez, L. Argenti, and F. Martín, "Hybrid-Basis Close-Coupling Interface to Quantum Chemistry Packages for the Treatment of Ionization Problems," *Journal of Chemical Theory and Computation* 13 (2017): 499–514.

344. Z. Mašín, J. Benda, J. D. Gorfinkiel, A. G. Harvey, and J. Tennyson, "UKRmol+: A Suite for Modelling Electronic Processes in Molecules Interacting With Electrons, Positrons and Photons Using the R-Matrix Method," *Computer Physics Communications* 249 (2020): 107092.

345. P. Decleva, M. Stener, and D. Toffoli, "Continuum Electronic States: The 'TIRESIA' Code," *Molecules* 27 (2022): 2026.

346. W. J. Glover, T. Mori, M. S. Schuurman, et al., "Excited State Non-Adiabatic Dynamics of the Smallest Polyene, Trans 1,3-Butadiene. II. Ab Initio Multiple Spawning Simulations," *Journal of Chemical Physics* 148 (2018): 164303.

347. T. Suzuki, L. Wang, and H. Kohguchi, "Femtosecond Time-Resolved Photoelectron Imaging of Ultrafast Electronic Dephasing in an Isolated Molecule," *Journal of Chemical Physics* 111 (1999): 4859–4861.

348. J. K. Song, M. Tsubouchi, and T. Suzuki, "Femtosecond Photoelectron Imaging on Pyrazine: Spectroscopy of 3s and 3p Rydberg States," *Journal of Chemical Physics* 115 (2001): 8810–8818.

349. T. Horio, T. Fuji, Y.-I. Suzuki, and T. Suzuki, "Probing Ultrafast Internal Conversion Through Conical Intersection via Time-Energy Map of Photoelectron Angular Distribution," *Journal of the American Chemical Society* 131 (2009): 10392–10393.

350. Y.-I. Suzuki, T. Fuji, T. Horio, and T. Suzuki, "Time-Resolved Photoelectron Imaging of Ultrafast $S_2 \rightarrow S_1$ Internal Conversion

Through Conical Intersection in Pyrazine," *Journal of Chemical Physics* 132 (2010): 174302.

351. T. Suzuki, "Time-Resolved Photoelectron Spectroscopy of Non-Adiabatic Electronic Dynamics in Gas and Liquid Phases," *International Reviews in Physical Chemistry* 31 (2012): 265–318.

352. S. Karashima, A. Humeniuk, and T. Suzuki, "Vibrational Motions in Ultrafast Electronic Relaxation of Pyrazine," *Journal of the American Chemical Society* 146 (2024): 11067–11071.

353. R. Schneider and W. Domcke, "$S_1 - S_2$ Conical Intersection and Ultrafast $S_2 \rightarrow S_1$ Internal Conversion in Pyrazine," *Chemical Physics Letters* 150 (1988): 235–242.

354. S. Deb and P. M. Weber, "The Ultrafast Pathway of Photon-Induced Electrocyclic Ring-Opening Reactions: The Case of 1,3-Cyclohexadiene," *Annual Review of Physical Chemistry* 62 (2011): 19–39.

355. B. C. Arruda and R. J. Sension, "Ultrafast Polyene Dynamics: The Ring Opening of 1,3-Cyclohexadiene Derivatives," *Physical Chemistry Chemical Physics* 16 (2014): 4439–4455.

356. R. B. Woodward and R. Hoffmann, "The Conservation of Orbital Symmetry," *Angewandte Chemie, International Edition* 8 (1969): 781–853.

357. W. T. A. M. van der Lugt and L. J. Oosterhoff, "Quantum-Chemical Interpretation of Photo-Induced Electrocyclic Reactions," *Chemical Communications (London)* 20 (1968): 1235–1236.

358. W. T. A. M. van der Lugt and L. J. Oosterhoff, "Symmetry Control and Photoinduced Reactions," *Journal of the American Chemical Society* 91 (1969): 6042–6049.

359. M. Kotur, T. Weinacht, B. J. Pearson, and S. Matsika, "Closed-Loop Learning Control of Isomerization Using Shaped Ultrafast Laser Pulses in the Deep Ultraviolet," *Journal of Chemical Physics* 130 (2009): 134311.

360. C. C. Pemberton, Y. Zhang, K. Saita, A. Kirrander, and P. M. Weber, "From the (1B) Spectroscopic State to the Photochemical Product of the Ultrafast Ring-Opening of 1,3-Cyclohexadiene: A Spectral Observation of the Complete Reaction Path," *Journal of Physical Chemistry A* 119 (2015): 8832–8845.

361. S. Adachi, M. Sato, and T. Suzuki, "Direct Observation of Ground-State Product Formation in a 1,3-Cyclohexadiene Ring-Opening Reaction," *Journal of Physical Chemistry Letters* 6 (2015): 343–346.

362. A. R. Attar, A. Bhattacherjee, C. D. Pemmaraju, et al., "Femtosecond X-Ray Spectroscopy of an Electrocyclic Ring-Opening Reaction," *Science* 356 (2017): 54–59.

363. T. J. A. Wolf, D. M. Sanchez, J. Yang, et al., "The Photochemical Ring-Opening of 1,3-Cyclohexadiene Imaged by Ultrafast Electron Diffraction," *Nature Chemistry* 11 (2019): 504–509.

364. S. Karashima, A. Humeniuk, R. Uenishi, et al., "Ultrafast Ring-Opening Reaction of 1,3-Cyclohexadiene: Identification of Nonadiabatic Pathway via Doubly Excited State," *Journal of the American Chemical Society* 143 (2021): 8034–8045.

365. O. Travnikova, T. Piteša, A. Ponzi, et al., "Photochemical Ring-Opening Reaction of 1,3-Cyclohexadiene: Identifying the True Reactive State," *Journal of the American Chemical Society* 144 (2022): 21878–21886.

366. P. Celani, M. Ottani, F. Olivucci, S. Bernardi, and M. A. Robb, "What Happens During the Picosecond Lifetime of $2A_1$ Cyclohexa-1,3-Diene? A CAS-SCF Study of the Cyclohexadiene/Hexatriene Photochemical Interconversion," *Journal of the American Chemical Society* 116, (1994): 10141–10151.

367. M. Merchán, L. Serrano-Andres, L. S. Slater, B. O. Roos, R. McDiarmid, and X. Xing, "Electronic Spectra of 1,4-Cyclohexadiene and 1,3-Cyclohexadiene: A Combined Experimental and Theoretical Investigation," *Journal of Physical Chemistry A* 103 (1999): 5468–5476.

368. M. Garavelli, C. S. Page, P. Celani, et al., "Reaction Path of a Sub-200 fs Photochemical Electrocyclic Reaction," *Journal of Physical Chemistry A* 105 (2001): 4458–4469.

369. A. Nenov, P. Kölle, M. A. Robb, and R. de Vivie-Riedle, "Beyond the Van der Lugt/Oosterhoff Model: When the Conical Intersection Seam and the S_1 Minimum Energy Path Do Not Cross," *Journal of Organic Chemistry* 75 (2010): 123–129.

370. A. Hofmann and R. de Vivie-Riedle, "Quantum Dynamics of Photoexcited Cyclohexadiene Introducing Reactive Coordinates," *Journal of Chemical Physics* 112 (2000): 5054–5059.

371. A. Hofmann and R. de Vivie-Riedle, "Adiabatic Approach for Ultrafast Quantum Dynamics Mediated by Simultaneously Active Conical Intersections," *Chemical Physics Letters* 346 (2001): 299–304.

372. J. B. Schönborn, J. Sielk, and B. Hartke, "Photochemical Ring-Opening of Cyclohexadiene: Quantum Wavepacket Dynamics on a Global Ab Initio Potential Energy Surface," *Journal of Physical Chemistry A* 114 (2010): 4036–4044.

373. A. Ohta, O. Kobayashi, S. O. Danielache, and S. Nanbu, "Nonadiabatic Ab Initio Molecular Dynamics of Photoisomerization Reaction Between 1,3-Cyclohexadiene and 1,3,5-Cis-Hexatriene," *Chemical Physics* 459 (2015): 45–53.

374. Y. Lei, H. Wu, X. Zheng, G. Zhai, and C. Zhu, "Photo-Induced 1,3-Cyclohexadiene Ring Opening Reaction: Ab Initio On-The-Fly Nonadiabatic Molecular Dynamics Simulation," *Journal of Photochemistry and Photobiology A: Chemistry* 317 (2016): 39–49.

375. O. Schalk, T. Geng, T. Thompson, et al., "Cyclohexadiene Revisited: A Time-Resolved Photoelectron Spectroscopy and Ab Initio Study," *Journal of Physical Chemistry A* 120 (2016): 2320–2329.

376. M. Filatov, S. K. Min, and K. S. Kim, "Non-Adiabatic Dynamics of Ring Opening in Cyclohexa-1,3-Diene Described by an Ensemble Density-Functional Theory Method," *Molecular Physics* 117 (2019): 1128–1141.

377. I. Polyak, L. Hutton, R. Crespo-Otero, M. Barbatti, and P. J. Knowles, "Ultrafast Photoinduced Dynamics of 1,3-Cyclohexadiene Using XMS-CASPT2 Surface Hopping," *Journal of Chemical Theory and Computation* 15 (2019): 3929–3940.

378. H. Tamura, S. Nanbu, T. Ishida, and H. Nakamura, "Ab Initio Nonadiabatic Quantum Dynamics of Cyclohexadiene/Hexatriene Ultrafast Photoisomerization," *Journal of Chemical Physics* 124 (2006): 084313.

379. J. Coonjobeeharry, K. E. Spinlove, C. Sanz Sanz, M. Sapunar, N. Došlić, and G. A. Worth, "Mixed-Quantum-Classical or Fully-Quantized Dynamics? A Unified Code to Compare Methods," *Philosophical Transactions. Series A, Mathematical, Physical, and Engineering Sciences* 380 (2022): 20–200.

380. J. Kim, H. Tao, J. L. White, V. S. Petrović, T. J. Martínez, and P. H. Bucksbaum, "Control of 1,3-Cyclohexadiene Photoisomerization Using Light-Induced Conical Intersections," *Journal of Physical Chemistry A* 116 (2012): 2758–2763.

381. J. Kim, H. Tao, T. J. Martínez, and P. Bucksbaum, "Ab Initio Multiple Spawning on Laser-Dressed States: A Study of 1,3-Cyclohexadiene Photoisomerization via Light-Induced Conical Intersections," *Journal of Physics B: Atomic Molecular and Optical Physics* 48 (2015): 164003.

382. D. Simah, B. Hartke, and H.-J. Werner, "Photodissociation Dynamics of H_2S on New Coupled Ab Initio Potential Energy Surfaces," *Journal of Chemical Physics* 111 (1999): 4523–4534.

383. B. Roos, "The Complete Active Space Self-Consistent Field Method and It Applications in Electronic Structure Calculations," *Advances in Chemical Physics* 69 (1987): 399–445.

384. R. Perez-Castillo, V. M. Freixas, S. Mukamel, et al., "Transient-Absorption Spectroscopy of Dendrimers via Nonadiabatic Excited-State Dynamics Simulations," *Chemical Science* 15 (2024): 13250–13261.

385. S. V. Pios, M. F. Gelin, A. Ullah, P. O. Dral, and L. Chen, "Artificial-Intelligence-Enhanced On-The-Fly Simulation of Nonlinear Time-Resolved Spectra," *Journal of Physical Chemistry Letters* 15 (2024): 2325–2331.

386. T. Suzuki, "Ultrafast Photoelectron Spectroscopy of Aqueous Solutions," *Journal of Chemical Physics* 151 (2019): 090901.

387. Z.-H. Loh, G. Doumy, C. Arnold, et al., "Observation of the Fastest Chemical Processes in the Radiolysis of Water," *Science* 367 (2020): 179–182.

388. Z. Yin, Y.-P. Chang, T. Balčiunas, et al., "Femtosecond Proton Transfer in Urea Solutions Probed by X-Ray Spectroscopy," *Nature* 619 (2023): 749–754.

389. B. Smith and A. V. Akimov, "Modeling Nonadiabatic Dynamics in Condensed Matter Materials: Some Recent Advances and Applications," *Journal of Physics: Condensed Matter* 32 (2019): 073001.

390. M. Mališ and S. Luber, "Trajectory Surface Hopping Nonadiabatic Molecular Dynamics With Kohn Sham Δ SCF for Condensed-Phase Systems," *Journal of Chemical Theory and Computation* 16 (2020): 4071–4086.

391. F. P. Bonafe, B. Aradi, B. Hourahine, et al., "A Real-Time Time-Dependent Density Functional Tight-Binding Implementation for Semiclassical Excited State Electron-Nuclear Dynamics and Pump-Probe Spectroscopy Simulations," *Journal of Chemical Theory and Computation* 16 (2020): 4454–4469.

392. H. W. Senn and W. Thiel, "QM/MM Methods for Biomolecular Systems," *Angewandte Chemie, International Edition* 48 (2009): 1198–1229.

393. D. Avagliano, M. Bonfanti, A. Nenov, and M. Garavelli, "Automatized Protocol and Interface to Simulate QM/MM Time-Resolved Transient Absorption at TD-DFT Level With COBRAMM," *Journal of Computational Chemistry* 43 (2022): 1641–1655.

394. M. Born and K. Huang, *Dynamical Theory of Crystal Lattices* (Oxford University Press, 1954).

395. L. Allen and J. H. Eberly, *Optical Resonance and Two-Level Atoms* (Dover Publications, 1987).

396. C. Xu, C. Lin, J. Peng, et al., "On-The-Fly Simulation of Time-Resolved Fluorescence Spectra and Anisotropy," *Journal of Chemical Physics* 160 (2024): 104109.

397. M. F. Gelin, R. Borrelli, and W. Domcke, "Efficient Orientational Averaging of Nonlinear Optical Signals in Multi-Chromophore Systems," *Journal of Chemical Physics* 147 (2017): 044114.

398. S. V. Pios, M. F. Gelin, L. Vasquez, J. Hauer, and L. Chen, "On-The-Fly Simulation of Two-Dimensional Fluorescence-Excitation Spectra," *Journal of Physical Chemistry Letters* 15 (2024): 8728–8735.

399. V. Sauri, L. Serrano-Andrés, A. R. M. Shahi, L. Gagliardi, S. Vancoillie, and K. Pierloot, "Multiconfigurational Second-Order Perturbation Theory Restricted Active Space (RASPT2) Method for Electronic Excited States: A Benchmark Study," *Journal of Chemical Theory and Computation* 7 (2011): 153–168.

400. J. Finley, P. A. Malmqvist, B. O. Roos, and L. Serrano-Andrés, "The Multi-State CASPT2 Method," *Chemical Physics Letters* 288 (1998): 299–306.

401. P. O. Löwdin, "Quantum Theory of Many-Particle Systems. I. Physical Interpretations by Means of Density Matrices, Natural Spin-Orbitals, and Convergence Problems in the Method of Configurational Interaction," *Physics Review* 97 (1955): 1474–1489.

402. F. Plasser, M. Ruckenbauer, S. Mai, M. Oppel, P. Marquetand, and L. González, "Efficient and Flexible Computation of Many-Electron Wave Function Overlaps," *Journal of Chemical Theory and Computation* 12 (2016): 1207–1219.

403. D. Toffoli, S. Coriani, M. Stener, and P. Decleva, "Tiresia: A Code for Molecular Electronic Continuum States and Photoionization," *Computer Physics Communications* 297 (2024): 109038.

404. K. Sun, L. Vasquez, R. Borrelli, L. Chen, Y. Zhao, and M. F. Gelin, "Interconnection Between Polarization-Detected and Population-Detected Signals: Theoretical Results and Ab Initio Simulations," *Journal of Chemical Theory and Computation* 20 (2024): 7560–7573.

Appendix A

Molecular Hamiltonian and Molecule-Field Interaction Hamiltonian

The molecular Hamiltonian H consists of the kinetic energy operators K_E of the electrons, K_N of the nuclei, and of the Coulomb Hamiltonian $V(\mathbf{r},\mathbf{R})$ comprising the electron–electron, electron-nuclei and nuclei–nuclei interactions,

$$H = K_N + K_E + V(\mathbf{r},\mathbf{R}) \tag{A1}$$

($\mathbf{r}$ and $\mathbf{R}$ denote the coordinates of electrons and nuclei, respectively). Relativistic effects, such as spin-orbit coupling, are not considered in this review. For applications in spectroscopy, it is appropriate to represent the molecular and molecule-field interaction Hamiltonians in a set of electronic states. In the context of quasi-classical trajectory calculations, the Born-Huang adiabatic electronic representation is preferred [394], in which the eigenfunctions $\Psi(\mathbf{r},\mathbf{R})$ of the total molecular Hamiltonian H are expanded in the set of eigenstates $\Phi_n(\mathbf{r},\mathbf{R})$ of the fixed-nuclei Hamiltonian $H_E = K_E + V(\mathbf{r},\mathbf{R})$:

$$\Psi(\mathbf{r},\mathbf{R}) = \sum_n \psi_n(\mathbf{R})\Phi_n(\mathbf{r},\mathbf{R}), \tag{A2}$$

$$\big(H_E - V_n(\mathbf{R})\big)\Phi_n(\mathbf{r},\mathbf{R}) = 0 \tag{A3}$$

($n = 0,1,2,\ \ldots$). In the discrete set of adiabatic electronic states $\Phi_n(\mathbf{r},\mathbf{R})$, the molecular Hamiltonian is then defined by its matrix elements

$$H_{nm} = \big[K_N + V_n(\mathbf{R})\big]\delta_{nm} - \Lambda_{nm}(\mathbf{R}). \tag{A4}$$

The $V_n(\mathbf{R})$ are the adiabatic electronic PE functions and the $\Lambda_{nm}(\mathbf{R})$ are the nonadiabatic coupling (NAC) operators, defined as

$$\Lambda_{nm} = -\int d\mathbf{r}\Phi_n^*(\mathbf{r},\mathbf{R})\big[K_N, \Phi_m(\mathbf{r},\mathbf{R})\big]. \tag{A5}$$

Usually, laser pulses are tuned into resonance with lower-lying singlet excited states Φ_n ($n \geq 1$) which are bright from the electronic ground state Φ_0. It is thus instructive to partition the electronic states $\{\Phi_n\}$ into three manifolds, {0}, {I}, {II} [30]. Manifold {0} consists of the single state Φ_0; manifold {I} contains the bright electronic states which can be interrogated by the laser pulses from the ground state as well as other electronic states strongly coupled to them; manifold {II} comprises those electronic states which can be probed by laser pulses from manifold {I}. In block-diagonal form, the Hamiltonian of Equation (A4) thus reads

$$H = \begin{pmatrix} H_0 & H_{0,\mathrm{I}} & 0 \\ H_{\mathrm{I},0} & H_{\mathrm{I}} & H_{\mathrm{I,II}} \\ 0 & H_{\mathrm{II,I}} & H_{\mathrm{II}} \end{pmatrix} \tag{A6}$$

where H_k is the molecular Hamiltonian in manifold k ($k = 0, \mathrm{I}, \mathrm{II}$) and the off-diagonal terms $H_{0,\mathrm{I}}$ and $H_{\mathrm{I,II}}$ are the nonadiabatic coupling operators (the direct coupling between manifolds {0} and {II} is neglected).

Downward and upward TDM operators have the corresponding block structure

$$\boldsymbol{\mu}^{\downarrow} = \begin{pmatrix} 0 & \boldsymbol{\mu}_{0,\mathrm{I}} & 0 \\ 0 & 0 & \boldsymbol{\mu}_{\mathrm{I,II}} \\ 0 & 0 & 0 \end{pmatrix}, \quad \boldsymbol{\mu}^{\uparrow} = \begin{pmatrix} 0 & 0 & 0 \\ \boldsymbol{\mu}_{\mathrm{I},0} & 0 & 0 \\ 0 & \boldsymbol{\mu}_{\mathrm{II,I}} & 0 \end{pmatrix} \tag{A7}$$

where $\boldsymbol{\mu}_{\mathrm{I},0}$ is responsible for the dipole transitions between the ground state and the states of manifold {I}, etc. Electronic transitions between manifolds {0} and {I} generate ground-state bleach (GSB) and stimulated emission (SE) contributions to spectroscopic signals, while transitions between manifolds {I} and {II} are responsible for excited-state absorption (ESA).

In the rotating-wave approximation (RWA) [395], the system-field interaction Hamiltonian assumes the form

$$H_F(t) = -\sum_j \Big\{ \big(\mathbf{s}_j \cdot \boldsymbol{\mu}^{\uparrow}\big)\mathscr{E}_j(t) + \big(\mathbf{s}_j \cdot \boldsymbol{\mu}^{\downarrow}\big)\mathscr{E}_j^*(t) \Big\} \tag{A8}$$

where

$$\mathscr{E}_j(t) = \lambda_j E_j\big(t - \bar{t}_j\big) e^{i\left(\mathbf{k}_j\mathbf{r} - \omega_j\left(t - \bar{t}_j\right)\right)}, \tag{A9}$$

and $\mathbf{s}_j, \lambda_j, E_j(t), \bar{t}_j, \mathbf{k}_j$ and ω_j are, respectively, the linear polarization vector, field amplitude, dimensionless normalized envelope function, arrival time, wave vector and carrier frequency of pulse j. The pulse durations τ_j can be defined as

$$\tau_j = E_j^{-1}(0)\int_{-\infty}^{\infty} dt E_j(t). \tag{A10}$$

For the description of time-resolved photoelectron signals, the upper excited-state manifold {II} is replaced by a multi-channel electronic continuum. The N-electron continuum states are written as antisymmetrized products of $(N-1)$-electron cationic states Ψ_f (the ionization channels) and one-electron continuum states in each channel $\Phi^{(-)}_{f\mathbf{k}_f}(\mathbf{r},\mathbf{R})$ defined by Equation (42) where $\mathbf{k}_f$ denotes the asymptotic k-vector of the continuum electron in channel f in the molecular frame. The superscript $(-)$ indicates incoming wave boundary conditions that are appropriate for the description of half-collision processes, such as photoionization or photodissociation [329]. Inter-channel couplings are neglected.

The elements of the matrices $\boldsymbol{\mu}^{\downarrow}$ and $\boldsymbol{\mu}^{\uparrow}$ in Equation (A7) take the form

$$\boldsymbol{\mu}^{\uparrow}_{ef\mathbf{k}_f} = \left\langle \Phi^{(-)}_{f\mathbf{k}_f}(\mathbf{r},\mathbf{R}) \mid \boldsymbol{\mu} \mid e \right\rangle \tag{A11}$$

$$\boldsymbol{\mu}^{\downarrow}_{ef\mathbf{k}_f} = \left\langle e \mid \boldsymbol{\mu} \mid \Phi(\mathbf{r},\mathbf{R})^{(-)}_{f\mathbf{k}_f} \right\rangle. \tag{A12}$$

The one-electron continuum functions are expanded in spherical harmonics

$$\phi^{(-)}_{f\mathbf{k}_f} = \sum_{l,m_l} \phi^{(-)}_{fk_f lm_l}(\mathbf{r},\mathbf{R}) Y_{l,m_l}\left(\hat{\mathbf{k}}_f\right) \tag{A13}$$

where $\hat{\mathbf{k}}_f$ is the unit vector in the asymptotic direction of the photoelectron in channel f. To obtain the angular distribution in the laboratory frame, the spherical harmonics are transformed with Wigner rotation matrices [299].

$$Y_{l,m_l}\left(\hat{\mathbf{k}}_f\right) = \sum_{n_l} D^{l}_{m_l n_l}(\alpha,\beta,\gamma) Y_{l,n_l}\left(\hat{\mathbf{K}}_f\right). \tag{A14}$$

Here $\hat{\mathbf{K}}_f$ is the unit vector in the asymptotic direction of the photoelectron in channel f in the laboratory frame and α, β and γ are the Euler angles which specify the orientation of the molecule in the laboratory frame.

Appendix B

Third-Order Response Functions

From the set of nonlinear response functions $R_{\alpha k}$ ($\alpha = \mathrm{R}, \mathrm{NR}$, $k = 0, \mathrm{I}, \mathrm{II}$) any third-order spectroscopic signal can be evaluated. In this work, the response functions are defined according to Refs [30, 131–133, 151, 259]

$$S_{\mathrm{R}}(t_3,t_2,t_1) = R_{\mathrm{R},0}(t_3,t_2,t_1) + R_{\mathrm{R,I}}(t_3,t_2,t_1) - R_{\mathrm{R,II}}(t_3,t_2,t_1)^{*}, \tag{B1}$$

$$S_{\mathrm{NR}}(t_3,t_2,t_1) = R_{\mathrm{NR},0}(t_3,t_2,t_1) + R_{\mathrm{NR,I}}(t_3,t_2,t_1) - R_{\mathrm{NR,II}}(t_3,t_2,t_1)^{*}. \tag{B2}$$

Explicitly,

$$R_{\mathrm{R},0}(t_3,t_2,t_1) = \mathrm{Tr}\left[(\mathbf{s}_1\cdot\boldsymbol{\mu}_{0,\mathrm{I}})e^{iH_1t_1}(\mathbf{s}_2\cdot\boldsymbol{\mu}_{1,0})e^{iH_0(t_2+t_3)}(\mathbf{s}_3\cdot\boldsymbol{\mu}_{0,\mathrm{I}})e^{-iH_1t_3}(\mathbf{s}_4\cdot\boldsymbol{\mu}_{\mathrm{I},0})e^{-iH_0(t_1+t_2)}\rho_0\right],$$

$$R_{\mathrm{NR},0}(t_3,t_2,t_1) = \mathrm{Tr}\left[e^{iH_0(t_1+t_2+t_3)}(\mathbf{s}_1\cdot\boldsymbol{\mu}_{0,\mathrm{I}})e^{-iH_1t_3}(\mathbf{s}_2\cdot\boldsymbol{\mu}_{1,0})e^{-iH_0t_2}(\mathbf{s}_3\cdot\boldsymbol{\mu}_{0,\mathrm{I}})e^{-iH_1t_1}(\mathbf{s}_4\cdot\boldsymbol{\mu}_{\mathrm{I},0})\rho_0\right],$$

$$R_{\mathrm{R,I}}(t_3,t_2,t_1) = \mathrm{Tr}\left[(\mathbf{s}_1\cdot\boldsymbol{\mu}_{0,\mathrm{I}})e^{iH_1(t_1+t_2)}(\mathbf{s}_2\cdot\boldsymbol{\mu}_{\mathrm{I},0})e^{iH_0t_3}(\mathbf{s}_3\cdot\boldsymbol{\mu}_{0,\mathrm{I}})e^{-iH_1(t_2+t_3)}(\mathbf{s}_4\cdot\boldsymbol{\mu}_{\mathrm{I},0})e^{-iH_0t_1}\rho_0\right],$$

$$R_{\mathrm{NR,I}}(t_3,t_2,t_1) = \mathrm{Tr}\left[e^{iH_0t_1}(\mathbf{s}_1\cdot\boldsymbol{\mu}_{0,\mathrm{I}})e^{iH_1t_2}(\mathbf{s}_2\cdot\boldsymbol{\mu}_{\mathrm{I},0})e^{iH_0t_3}(\mathbf{s}_3\cdot\boldsymbol{\mu}_{0,\mathrm{I}})e^{-iH_1(t_1+t_2+t_3)}(\mathbf{s}_4\cdot\boldsymbol{\mu}_{\mathrm{I},0})\rho_0\right],$$

while $R_{\alpha,\mathrm{II}}$ are written as

$$R_{\mathrm{R,II}}(t_3,t_2,t_1) = \mathrm{Tr}\left[e^{iH_0t_1}(\mathbf{s}_1\cdot\boldsymbol{\mu}_{0,\mathrm{I}})e^{iH_1t_2}(\mathbf{s}_2\cdot\boldsymbol{\mu}_{\mathrm{I,II}})e^{iH_{\mathrm{II}}t_3}(\mathbf{s}_3\cdot\boldsymbol{\mu}_{\mathrm{II,I}})e^{-iH_1(t_1+t_2+t_3)}(\mathbf{s}_4\cdot\boldsymbol{\mu}_{\mathrm{I},0})\rho_0\right],$$

$$R_{\mathrm{NR,II}}(t_3,t_2,t_1) = \mathrm{Tr}\left[(\mathbf{s}_1\cdot\boldsymbol{\mu}_{0,\mathrm{I}})e^{iH_1(t_1+t_2)}(\mathbf{s}_2\cdot\boldsymbol{\mu}_{\mathrm{I,II}})e^{iH_{\mathrm{II}}t_3}(\mathbf{s}_3\cdot\boldsymbol{\mu}_{\mathrm{II,I}})e^{-iH_1(t_2+t_3)}(\mathbf{s}_4\cdot\boldsymbol{\mu}_{\mathrm{I},0})e^{-iH_0t_1}\rho_0\right]$$

where

$$\rho_0 = Z_0^{-1}\exp\{-\beta H_0\} \tag{B3}$$

is the initial thermal equilibrium (Boltzmann) distribution, $\beta = (k_B T_B)^{-1}$, Z_0 is the partition function, and T_B is the temperature of the molecular ensemble.

Recasting the above expressions in the DW form of Equation (7), we can write

$$R_{\alpha k}(t_3,t_2,t_1)=\mathrm{Tr}\left[\mathcal{W}_{\alpha k}(t_3)\mathcal{L}(t_2)\mathcal{D}_{\alpha k}(t_1)\right] \tag{B4}$$

where

$$\mathcal{D}_{\mathrm{NR,0}}(t_1)=\mathcal{D}_{\mathrm{R,0}}(t_1)^{\dagger}=(\mathbf{s}_1\cdot\boldsymbol{\mu}_{0,\mathrm{I}})e^{-iH_{\mathrm{I}}t_1}(\mathbf{s}_2\cdot\boldsymbol{\mu}_{10})\rho_0 e^{iH_0t_1} \tag{B5}$$

$$\mathcal{D}_{\mathrm{NR,I}}(t_1)=\mathcal{D}_{\mathrm{R,II}}(t_1)=\mathcal{D}_{\mathrm{R,I}}(t_1)^{\dagger}=\mathcal{D}_{\mathrm{NR,II}}(t_1)^{\dagger}=e^{-iH_{\mathrm{I}}t_1}(\mathbf{s}_1\cdot\boldsymbol{\mu}_{\mathrm{I},0})\rho_0 e^{iH_0t_1}(\mathbf{s}_2\cdot\boldsymbol{\mu}_{0,\mathrm{I}}) \tag{B6}$$

and

$$\mathcal{W}_{\mathrm{NR,0}}(t_3)=\mathcal{W}_{\mathrm{R,0}}(t_3)=e^{iH_0t_3}(\mathbf{s}_3\cdot\boldsymbol{\mu}_{0,\mathrm{I}})e^{-iH_{\mathrm{I}}t_3}(\mathbf{s}_4\cdot\boldsymbol{\mu}_{\mathrm{I},0}) \tag{B7}$$

$$\mathcal{W}_{\mathrm{NR,I}}(t_3)=\mathcal{W}_{\mathrm{R,I}}(t_3)=(\mathbf{s}_3\cdot\boldsymbol{\mu}_{\mathrm{I},0})e^{iH_0t_3}(\mathbf{s}_4\cdot\boldsymbol{\mu}_{0,\mathrm{I}})e^{-iH_{\mathrm{I}}t_3} \tag{B8}$$

$$\mathcal{W}_{\mathrm{NR,II}}(t_3)=\mathcal{W}_{\mathrm{R,II}}(t_3)=(\mathbf{s}_3\cdot\boldsymbol{\mu}_{\mathrm{I,II}})e^{iH_{\mathrm{II}}t_3}(\mathbf{s}_4\cdot\boldsymbol{\mu}_{\mathrm{II},\mathrm{I}})e^{-iH_{\mathrm{I}}t_3}. \tag{B9}$$

Appendix C

Orientational Averaging for Optical Signals

If the orientation of the molecular system under study is fixed in the laboratory frame, the orientations of the TDMs $\boldsymbol{\mu}_{ge}$ can be considered fixed. If, on the other hand, molecular systems in the ensemble are randomly oriented in space, then averaging over their orientations is necessary. It can be carried out as follows. Following [207, 396], we can rewrite the FWM signal of Equation (13) as

$$I_\alpha(\tau,T,\tau_t)=\sum_{a,b,c,d=x,y,z}s_p^{(a)}s_p^{(b)}s_u^{(c)}s_u^{(d)}\mathrm{Re}\sum_{k=0,\mathrm{I,II}}a_k\left\langle W_k^{(cd)}(\mathbf{R}(T),\mathbf{P}(T);\tau_t)D_\alpha^{(ab)}(\mathbf{R},\mathbf{P};\tau)\right\rangle_{\mathrm{MC}}$$

where the explicit expressions for $D_\alpha^{(ab)}(\mathbf{R},\mathbf{P};\tau)$ and $W_k^{(\mathrm{cd})}(\mathbf{R},\mathbf{P};\tau_t)$ can be retrieved from Equations (14–17). The indices $a,b,c,d=x,y,z$ denote the x,y,z components of the TDMs in a certain (arbitrary) reference frame. By employing the method of [397], the orientational averaging (denoted by overbar) can be achieved as follows:

$$\overline{I_\alpha(\tau,T,\tau_t)}=\frac{1}{15}\left(1+2(\mathbf{s}_p\cdot\mathbf{s}_u)^2\right)\left(I_\alpha^{(xxxx)}+I_\alpha^{(yyyy)}+I_\alpha^{(zzzz)}\right)+ \tag{C1}$$

$$\frac{1}{15}\left(2-(\mathbf{s}_p\cdot\mathbf{s}_u)^2\right)\left(I_\alpha^{(yyxx)}+I_\alpha^{(zzxx)}+I_\alpha^{(xxyy)}+I_\alpha^{(zzyy)}+I_\alpha^{(xxzz)}+I_\alpha^{(yyzz)}\right)+$$

$$\frac{2}{15}\left(3(\mathbf{s}_p\cdot\mathbf{s}_u)^2-1\right)\left(I_\alpha^{(yxyx)}+I_\alpha^{(zxzx)}+I_\alpha^{(zyzy)}\right).$$

(the explicit dependence of $I_\alpha^{(abcd)}$ on (τ,T,τ_t) is omitted for brevity). It is essential that the evaluation of the $I_\alpha^{(abcd)}$ in Equation (C1) does not require 12 rounds of trajectory simulations. One just has to save the x,y,z components of the TDMs along each trajectory. Then all $I_\alpha^{(abcd)}$ can be calculated through their DW expressions in the post-procession stage.

Appendix D

DW Formulas for Dispersed TA PP Signals

The dispersed TA PP signal is determined through the general FWM signal of Equation (13) as follows:

$$I^{dis}(\omega_{pu},\omega_t,T)\sim\int d\tau_t e^{i\omega_t\tau_t}\left(I_{\mathrm{R}}(0,T,\tau_t)+I_{\mathrm{NR}}(0,T,\tau_t)\right) \tag{D1}$$

It can be evaluated through the expression [160].

$$I^{dis}(T,\omega_t)\sim\sum_{k=0,\mathrm{I,II}}a_k\left\langle W_k^{dis}(\mathbf{R}(T),\mathbf{P}(T);\omega_t)D(\mathbf{R},\mathbf{P},\omega_{pu})\right\rangle_{\mathrm{MC}} \tag{D2}$$

in which the doorway function is defined by Equation (23), while the dispersed window functions read

$$W_0^{dis}(\omega,\mathbf{R}_g(T),\mathbf{P}_g(T);\omega_t)=E_{pr}^2(\omega-\omega_{pr})\sum_e\frac{\nu\left(\mathbf{s}_{pr}\cdot\boldsymbol{\mu}_{ge}(\mathbf{R}_g(T))\right)^2}{\nu^2+\left(\omega_t-\omega_{eg}(\mathbf{R}_g(T))\right)^2}, \tag{D3}$$

$$W_{\mathrm{I}}^{dis}(\omega,\mathbf{R}_e(T),\mathbf{P}_e(T);\omega_t)=E_{pr}^2(\omega-\omega_{pr})\frac{\nu\left(\mathbf{s}_{pr}\cdot\boldsymbol{\mu}_{ge(T)}(\mathbf{R}_e(T))\right)^2}{\nu^2+\left(\omega_t-\omega_{e(T)g}(\mathbf{R}_e(T))\right)^2}, \tag{D4}$$

$$W_{\mathrm{II}}^{dis}\left(\mathbf{R}_e(T),\mathbf{P}_e(T);\omega_t\right)=E_{pr}^2\left(\omega-\omega_{pr}\right)\sum_f\frac{\nu\left(\mathbf{s}_{pr}\cdot\boldsymbol{\mu}_{e(T)f}\left(\mathbf{R}_e(T)\right)\right)^2}{\nu^2+\left(\omega_t-\omega_{fe(T)}\left(\mathbf{R}_e(T)\right)\right)^2}. \tag{D5}$$

The first, second and third terms in Equation (D2) correspond to the GSB, SE and ESA contributions. ν is the electronic dephasing rate, which determines frequency resolution of $I^{dis}\left(T,\omega_t\right)$.

Two factors determine the shapes of TA PP spectra in the frequency domain and the shapes of peaks in 2D spectra. The first factor is the spectral profile of the pulses $E_j(\omega)$, $j=1,2,3,4$. The second factor is the dephasing rate ν, which describes homogeneous broadening. It corresponds to the peak-shape function $A(t)=\exp(-\nu t)$ whose one-sided Fourier transform $\widetilde{A}(\omega)=1/(\nu+i\omega)$ yields Lorentzian shapes of the spectral features. Other shapes (e.g., Gaussian or Voigt) can be chosen, if necessary, by adopting more realistic functions $A(t)$ and $\widetilde{A}(\omega)=\int_0^\infty dt\exp(-i\omega t)A(t)$. Then, for example,

$$W_{\mathrm{I}}\left(\mathbf{R}_e(T),\mathbf{P}_e(T);\omega_t\right)=E_{pr}^2\left(\omega-\omega_{pr}\right)\left(\mathbf{s}_{pr}\cdot\boldsymbol{\mu}_{ge(T)}\left(\mathbf{R}_e(T)\right)\right)^2\widetilde{A}\left(\omega_t-\omega_{e(T)g}\left(\mathbf{R}_e(T)\right)\right) \tag{D6}$$

and the other DW functions are modified accordingly. Gaussian lineshape functions were recently employed in [398].

Appendix E

Transient-Absorption Pump-Probe Signals for Coupled {0}-{I} Manifolds

In the case of {0}-{I} nonadiabatic coupling, the general quasi-classical DW expression for the evaluation of the integral TA PP spectrum is written as

$$I^{int}\left(\omega_{pu},\omega_{pr},T\right)\sim\sum_{k=0,\mathrm{I},\mathrm{II}}a_k\left\langle\widehat{W}_k^{int}\left(\omega_{pr},\mathbf{R}(T),\mathbf{P}(T)\right)D\left(\omega_{pu},\mathbf{R},\mathbf{P}\right)\right\rangle_{\mathrm{MC}}. \tag{E1}$$

The T-evolution is governed by the total field-free molecular Hamiltonian H (including nonadiabatic couplings). The explicit expression for the doorway function D remains unchanged. The window functions $\widehat{W}_k^{int}$ are defined in terms of their counterparts W_k^{int} specified by Equations (15–17) as follows [183, 396]:

$$\widehat{W}_0^{int}=W_0^{int},$$

$$\widehat{W}_{\mathrm{I}}^{int}=\begin{cases}W_{\mathrm{I}}^{int}, & \text{if the trajectory stays within }\{\mathrm{I}\}\\ -W_0^{int}, & \text{if the trajectory jumps from }\{\mathrm{I}\}\text{ to }\{0\}\end{cases} \tag{E2}$$

$$\widehat{W}_{\mathrm{II}}^{int}=\begin{cases}W_{\mathrm{II}}^{int}, & \text{if the trajectory stays within }\{\mathrm{I}\}\\ 0, & \text{if the trajectory jumps from }\{\mathrm{I}\}\text{ to }\{0\}.\end{cases} \tag{E3}$$

If a trajectory jumps from manifold {I} back to the ground state, then $e(T)$ is switched to g in Equations (E2) and (E3). This trajectory contributes to the GSB with a minus sign, see Equation (E2). The reason for the minus sign is as follows. If the standard DW functions are defined as positive laser-induced populations, then the GSB contribution to the TA PP signal has to be written as

$$I_{GSB}^{int}\left(\omega_{pu},\omega_{pr},T\right)\sim\left\langle\left(-D(\mathbf{R},\mathbf{P})\right)\left(-W_0^{int}(\omega_{pr},\mathbf{R}(T),\mathbf{P}(T))\right)\right\rangle_{\mathrm{MC}}, \tag{E4}$$

because the pump pulses creates a "hole" in the ground-state population. This means that the population generated by the internal conversion $\{\mathrm{I}\}\rightarrow\{0\}$ is counted positive, while the original ground-state population generated by the pump pulse (a hole) is negative. If T exceeds both the internal-conversion time constant and vibrational relaxation time constant in the ground state, the equilibrium distribution is restored in the ground state and

$$I^{int}\left(\omega_{pu},\omega_{pr},T\right)\rightarrow 0$$

because no optically induced population remains in the ground state (so-called bleach recovery).

Appendix F

Calculation of Photoelectron Spectroscopy Observables

The Dyson orbital for the $e \rightarrow f$ ionization channel is given by

$$| \phi_{ef}^{D} \rangle = \sqrt{N} \int \Psi_f(x_1, \ldots, x_{N-1})^* \Psi_e(x_1, x_2, \ldots, x_N) dx_1 \ldots dx_{N-1} \tag{F1}$$

where $|\Psi_e\rangle$ is the wave function of an excited state e of the neutral molecule and Ψ_f is the wave function of the cation in state f. The electronic wave functions of the neutral molecule are expanded in terms of normalized CASSCF Slater determinants as:

$$|\Psi_e\rangle = \sum_a c_{ae}^N |\Phi_a^N\rangle \tag{F2}$$

where the Slater determinants of the neutral molecule are constructed from a set of molecular spin-orbitals $\{\chi\}$ and are given by:

$$|\Phi_a^N\rangle = \frac{1}{\sqrt{N!}} \det\left[\chi_{a1}, \ldots, \chi_{aN}\right] \tag{F3}$$

Similarly, the electronic wave functions of the cation are expanded as follows:

$$\left|\Psi_f\right\rangle = \sum_b c_{bf}^{N-1} |\Phi_b^{N-1}\rangle \tag{F4}$$

where the Slater determinants of the cation are built from a different set of molecular spin-orbitals $\{\phi\}$

$$|\Phi_b^{N-1}\rangle = \frac{1}{\sqrt{(N-1)!}} \det\left[\phi_{b1}, \ldots, \phi_{b(N-1)}\right]. \tag{F5}$$

In Equations (F2) and (F4) the coefficients c_{ae}^N and c_{bf}^{N-1} are the CASSCF configuration interaction vectors for the neutral molecule and the cation, respectively.

The computation of Dyson orbitals using the extended multi-state (XMS) complete active space second-order perturbation theory (CASPT2) method [201] has been described in [336] It is assumed that the XMS-CASPT2 wave function is well approximated by the so-called perturbatively modified (PM) CASSCF wave function [399]. In this case, the XMS-CASPT2 configuration interaction vectors are obtained by rotating the CASSCF states with the XMS-CASPT2 rotation matrix $\mathbf{U}$ [400]

$$\mathbf{C}_{\text{XMS-CASPT2}} = \mathbf{C}_{\text{CASSCF}} \mathbf{U} \tag{F6}$$

where the matrix $\mathbf{C}_{\text{CASSCF}}$ contains the CASSCF configuration interaction vectors as its columns. The Dyson orbital is obtained by substituting (F2) and (F4) into Equation (F1) as

$$\left|\phi_{ef}^{D}\right\rangle = \sqrt{N} \sum_a \sum_b c_{bf}^{*N-1} c_{ae}^N \left\langle \Phi_{bf}^{N-1} | \, \Phi_{ae}^N \right\rangle. \tag{F7}$$

This equation can also be expressed in second quantization form as

$$\left|\phi_{ef}^{D}\right\rangle = \sum_a \sum_b c_{bf}^{*N-1} c_{ae}^N \sum_k \left\langle \Phi_{bf}^{N-1} | \, \hat{a}_k \, | \, \Phi_{ae}^N \right\rangle |\chi_{ak}\rangle, \tag{F8}$$

where $\hat{a}_k$ is the annihilation operator for the k-th spin-orbital in the a-th determinant, $|\chi_{ak}\rangle$. Finally, to compute $\left|\phi_{ef}^{D}\right\rangle$ we recall that the overlap between two Slater determinants is given by the determinant of the overlap matrix between the orbitals composing the two determinants [401, 402].

In [336] the free-electron orbitals $|\phi_k\rangle$ were computed using the B-spline static-exchange DFT (SE-DFT) approach. Here the one-electron continuum orbital $|\phi_k\rangle$ is obtained as the solution of Kohn-Sham (KS) equation for a kinetic energy E_k

$$H_{KS} \phi_k = E_k \phi_k. \tag{F9}$$

The KS Hamiltonian, H_{KS}, is given as

$$H_{KS} = -\frac{1}{2}\Delta + V_N + V_C + V_{XC} \tag{F10}$$

where V_N is the nuclear attraction potential. The Coulomb potential, $V_C(\rho)$, and the exchange-correlation potential, $V_{XC}(\rho)$, are defined by the ground-state electron density, ρ, which is computed separately in a single-point DFT calculation. The Hamiltonian matrix is then constructed in a multicenter (LCAO) B-spline basis, which is given as the product of radial B-spline functions and real spherical harmonics expanded over several centers (i) in the molecule

$$\chi_{nl\lambda}^{(i)} = \frac{1}{r^{(i)}} B_n\left(r^{(i)}\right) X_{l\lambda}\left(\theta_i, \phi_i\right). \tag{F11}$$

Here B_n is the n-th B-spline function and

$$X_{l\lambda}(\theta, \phi) = \sum_m Y_{lm}^R(\theta, \phi) b_{m\lambda} \tag{F12}$$

are linear combinations of real spherical harmonics Y_{lm}^R with angular momentum quantum numbers l and m, and λ is a symmetry-related collective index [338]. The multicenter expansion includes a single-center expansion with the origin in the molecule's center of mass, associated with a sphere of large radius, and a superposition of spherical basis sets of small radii centered on the various atoms (the LCAO part). Bound states are computed using conventional diagonalization of the Hamiltonian matrix, while the Galerkin approach is employed to find the solutions in the continuum for the energy E_k. The B-spline SE-DFT method is implemented in the Tiresia program [345, 403].

Appendix G

Simulation Protocols

The initialization of a classical trajectory requires the specification of the initial nuclear coordinates and momenta $\mathbf{R}_g$, $\mathbf{P}_g$ in the electronic ground state and the selection of the initially excited state e of manifold {I}. $\mathbf{R}_g$ and $\mathbf{P}_g$ are sampled from the Wigner distribution $\rho_g^{Wig}\left(\mathbf{R}_g, \mathbf{P}_g\right)$ of the electronic ground state. The initial electronic state excited by the pump pulse is sampled from the oscillator strength distribution of the electronic states in manifold {I}. This sampling distribution

$$\rho_s\left(\mathbf{R}_g, \mathbf{P}_g, e\right) = \left|\boldsymbol{\mu}_{ge}\left(\mathbf{R}_g\right)\right|^2 \rho_g^{Wig}\left(\mathbf{R}_g, \mathbf{P}_g\right) \tag{G1}$$

is the standard choice for the simulation of time-dependent electronic population probabilities with quasi-classical propagation methods. The sampling distribution of Equation (G1) is appropriate for very short (sub-fs) pump pulses. The power spectrum of the pump pulse, $E_{pu}^2\left(\omega_{pu} - U_{eg}\left(\mathbf{R}_g\right)\right)$, is then included in the evaluation of the doorway function, Equation (23). For longer pulses, it is computationally more efficient to include the power spectrum of the pump pulse in the sampling distribution, using

$$\rho_s\left(\mathbf{R}_g, \mathbf{P}_g, e\right) = E_{pu}^2\left(\omega_{pu} - U_{eg}\left(\mathbf{R}_g\right)\right)\left|\boldsymbol{\mu}_{ge}\left(\mathbf{R}_g\right)\right|^2 \rho_g^{Wig}\left(\mathbf{R}_g, \mathbf{P}_g\right). \tag{G2}$$

With any of these assumptions, the fundamental DW expression, Equation (13), is replaced by

$$I_\alpha\left(\tau, T, \tau_t\right) \sim \mathrm{Re} \sum_{k=0,\mathrm{I},\mathrm{II}} a_k \left\langle W_k(\mathbf{R}(T), \mathbf{P}(T); \tau_t) D_\alpha^{(s)}(\mathbf{R}_g, \mathbf{P}_g; \tau)\right\rangle_{\mathrm{MCs}} \tag{G3}$$

in which $\langle \ldots \rangle_{\mathrm{MCs}}$ means MC sampling of the initial trajectories from ρ_s and

$$D_\alpha^{(s)}\left(\mathbf{R}_g, \mathbf{P}_g; \tau\right) = \rho_s^{-1}\left(\mathbf{R}_g, \mathbf{P}_g, e\right) D_\alpha\left(\mathbf{R}_g, \mathbf{P}_g; \tau\right). \tag{G4}$$

With the definition of Equation (G1), for example, the TA PP doorway function of Equation (23) turns into

$$D^{(s)}\left(\mathbf{R}_g, \mathbf{P}_g\right) = \frac{\left(\mathbf{s}_{pu} \cdot \boldsymbol{\mu}_{ge}\left(\mathbf{R}_g\right)\right)^2}{\left|\boldsymbol{\mu}_{ge}\left(\mathbf{R}_g\right)\right|^2}. \tag{G5}$$

Equation (G5) was used, for example, in [384]. It is essential that Equation (G5) does not contain singularities since $0 \le D^{(s)}\left(\mathbf{R}_g, \mathbf{P}_g\right) \le 1$. If one is not interested in polarization-sensitive detection, one can chose $\mathbf{s}_{pu} \parallel \boldsymbol{\mu}_{ge}$, which gives $D^{(s)}\left(\mathbf{R}_g, \mathbf{P}_g\right) = 1$.

The computational steps involved in the simulation of the general FWM signal of Equation (13) with classical trajectories can be summarized as follows.

1. Sample an initial condition $\mathbf{R}_g, \mathbf{P}_g$ and e from the phase-space distribution $\rho_s\left(\mathbf{R}_g, \mathbf{P}_g, e\right)$ of Equation (G1) or Equation (G2) and calculate the doorway function $D_\alpha^{(s)}\left(\mathbf{R}_g, \mathbf{P}_g; \tau\right)$ of Equation (G4).
2. Propagate the trajectory $\mathbf{R}_g(t), \mathbf{P}_g(t)$ with the classical ground-state Hamiltonian H_0 up to the final time t_F of the simulation.
3. Evaluate $W_0\left(\mathbf{R}_g(T), \mathbf{P}_g(T); \tau_t\right)$ for the desired grid of pulse delay times T.
4. Propagate the trajectory $\mathbf{R}_e(t), \mathbf{P}_e(t)$ with the SH algorithm up to the final time t_F of the simulation.
5. Evaluate $W_{\mathrm{I}}\left(\mathbf{R}_e(T), \mathbf{P}_e(T); \tau_t\right)$ and $W_{\mathrm{II}}\left(\mathbf{R}_e(T), \mathbf{P}_e(T); \tau_t\right)$ for the desired grid of pulse delay times T.
6. Repeat these calculations until the MC sampling is converged.

The signals considered in this review can be evaluated by a straightforward adaptation of this algorithm. The possibility of the on-the-fly DW simulation of so-called population-detected signals has recently been discussed in [404].